

# Dynamical stellar masses via high angular resolution techniques

---

SEBATIÁN GASPAR ZÚÑIGA FERNÁNDEZ



**Universidad  
de Valparaíso**  
CHILE



Instituto de Física y Astronomía  
Facultad de Ciencias  
Universidad de Valparaíso  
Doctorado en Astrofísica

---

Mes 2021  
Valparaíso. Chile.



Dedicado a tres mujeres excepcionales, mi amada compañera Sofia, mi madre y mi  
hermana.



This thesis is solely my own composition,  
except where specifically indicated in the text.

Total or partial reproduction, for scientific or academic purposes,  
is authorised including a bibliographic reference to this document.

Sebastián Gaspar Zúñiga Fernández

Mes 2021.

Valparaíso. Chile.



# Acknowledgements

First and foremost, I would like to express my gratitude to my supervisors Prof. Johan Olofsson and Prof. Amelia Bayo for their continuous support and patience during my Ph.D. journey. I am thankful for their guidance, invaluable constructive criticism, and friendly advice during my study. I would like to especially thank your efforts to support my ideas and requests during the doctorate, mainly my intentions to participate in an instrumentation project and later to apply for the ESO studentship. I am very grateful to Dr. Xavier Haubois and Dr. Jesus Corral-Santana for being my supervisors during my two-year stay at ESO Chile. I appreciate your willingness to open a window of time between shifts at Paranal and your science to co-supervise my thesis work. I would like also thank Dr. Jean-Philippe Berger at the Institut de Planétologie et d'Astrophysique de Grenoble (IPAG) for hosting and supporting my 3-month stay at IPAG and for inviting me to be part of the NAOMI commissioning in Paranal, which was a really valuable experience for my career. I am also grateful to Dr. Andrei Tokovinin for his insightful comments during our collaboration and especially for agreeing to be part of my thesis review committee under somewhat special circumstances. Coming from another area, at the beginning of my PhD I had to make some decisions almost blindly, so I feel very lucky to have ended up surrounded by such a great group. I believe that the rigorous research training they have provided will continue to benefit me immensely throughout my career.

I gratefully acknowledge financial support from Universidad de Valparaíso via Fondo Institucional de Becas (FIB-UV, 2017), the European Southern Observatory via its studentship program and ANID via PFCHA/Doctorado Nacional/2018-21181044. Also I would like to thank support by ANID, – Millennium Science Initiative Program– NCN19\_171 and the Max Planck Tandem Group MPIA - Universidad de Valparaíso.



# Abstract

Multiple stellar systems are abundant in our galaxy. Almost half of solar-like field stars have at least one companion. Multiple systems are the perfect playground to determine the stellar mass, which is one of the most fundamental parameters in stellar astrophysics, without having to rely heavily on models. In this thesis we present the results of detection and orbital characterisation of multiple systems in young ( $\sim 5 - 100$  Myr) associations. The aim is to identify binary and multiple systems in our sample and determine their dynamical masses. Ultimately, the results of this work should provide valuable information to calibrate evolutionary models of low-mass ( $< 0.5 M_{\odot}$ ) pre-main sequence stars.

The SACY sample (Search for Association Containing Young stars) is a collection of nearby ( $< 200$  pc) young ( $\sim 5 - 100$  Myr) stars, mostly with estimated masses  $\sim 0.1 - 1.2 M_{\odot}$ . The sample is structured in groups consistent of separated populations known as moving group or associations, such as the  $\beta$ -Pic moving group and the AB Doradus association.

In Chapter 2, we identify 68 spectroscopic binaries (SBs) among our sample of 410 objects and update the SB fraction of each young association. Our results hint at the possibility that the youngest associations have a higher SB fraction ( $\sim 30\%$ ) in comparison with the five oldest ( $\sim 10\%$ ). This difference suggests could hint towards a non-universal primordial multiplicity in the youngest associations. One of the well known SB in our sample is the quadruple system HD 98800. The system is composed of two SBs orbiting each other (AaAb and BaBb), with a gas-rich disc in polar configuration around BaBb. We obtain new astrometric measurements using long-baseline infrared interferometric observations with the VLTI/PIONIER instrument. Combining our new astrometry with archival observations and radial velocity measurements, we determine the orbital parameters of both subsystems. We refine the orbital solution of BaBb and derive, for the first time, the orbital solution of AaAb. In addition, we confirm the polar configuration of the disc around BaBb. Furthermore, we present some

preliminary results on astrometric measurements for seven interesting binary systems that we are monitoring with AO-imaging observations. Additionally, we also report new estimates on the astrometry of seven binaries using VLTI PIONIER observations. These astrometric measurements will be used to prepare the future work towards full orbital characterisation and dynamical masses determination in those multiple systems. Finally, in Chapter 5 we describe our contribution to the commissioning of the New Adaptive Optics Module for Interferometry (NAOMI).

# Contents

<b>1</b>	<b>Introduction</b>	<b>1</b>
1.1	The role of multiplicity in Star Formation . . . . .	1
1.1.1	Formation process of a single low-mass star . . . . .	1
1.1.2	Formation of multiple star systems . . . . .	3
1.2	Observational studies on stellar multiplicity . . . . .	5
1.2.1	The field populations . . . . .	5
1.2.2	Star forming regions and other young populations . . . . .	6
1.3	Dynamical masses . . . . .	9
1.4	Organisation of the thesis . . . . .	15
<b>2</b>	<b>An updated census of spectroscopic binaries in SACY</b>	<b>17</b>
2.1	Introduction . . . . .	17
2.2	Sample . . . . .	20
2.3	Observations and additional data . . . . .	20
2.3.1	Archival high-resolution spectra . . . . .	21
2.3.2	Previously published quantities . . . . .	21
2.3.3	Gaia Data Release 2 . . . . .	23
2.3.4	Assessing membership using BANYAN $\Sigma$ . . . . .	24
2.3.5	Rotational periods from light curves . . . . .	26
2.4	Properties and calculation of CCF profiles . . . . .	28
2.4.1	Sources of uncertainty . . . . .	28

## CONTENTS

2.4.2	Cross-correlation features . . . . .	29
2.5	Estimates of radial and rotational velocities . . . . .	30
2.5.1	Cross-match with literature . . . . .	32
2.6	Using multiple measurements to identify single-lined spectroscopic binaries . . . . .	32
2.6.1	Distinguishing RV variation as a function of rotation . . . . .	33
2.6.2	Distinguishing fast rotators from blended binaries . . . . .	35
2.6.3	Using the BIS versus RV relation . . . . .	36
2.6.4	Spectroscopic binaries from the literature . . . . .	37
2.6.5	Close visual binaries from the literature . . . . .	37
2.6.6	Detection of SBs candidates . . . . .	38
2.7	Accounting for observation sensitivity . . . . .	38
2.8	Updated census of spectroscopic binaries . . . . .	41
2.9	Discussion . . . . .	43
2.9.1	Comparison with previous results on low density environments . . . . .	43
2.9.2	The impact of the sensitivity correction . . . . .	44
2.9.3	Relation with higher-order multiplicity . . . . .	46
2.9.4	SB fraction evolution with age . . . . .	46
2.9.5	Role of the environment . . . . .	47
2.10	Summary and conclusions . . . . .	48
2.11	Appendix . . . . .	49
2.11.1	Targets flagged as potential SB1 . . . . .	49
2.11.2	Notes on individual sources . . . . .	50
2.11.3	Measurements of $v \sin i$ . . . . .	62
2.11.4	SB1 systems identified in this work . . . . .	67
2.11.5	Gaia DR2 . . . . .	68
2.11.6	Rotational periods from light curves . . . . .	68
2.11.7	Sensitivity maps . . . . .	70
2.11.8	Individual and summary tables . . . . .	74

## 3 The HD 98800 quadruple pre-main sequence system

77

## CONTENTS

3.1	Introduction . . . . .	77
3.2	Observations, astrometry, and RV . . . . .	80
3.2.1	PIONIER observations and data reduction . . . . .	80
3.2.2	Determining the AaAb and BaBb astrometry . . . . .	81
3.2.3	AB astrometry . . . . .	83
3.2.4	CTIO spectroscopy . . . . .	84
3.2.5	Reduced spectra from public archives . . . . .	84
3.2.6	Literature data . . . . .	85
3.3	Orbital fitting . . . . .	85
3.3.1	BaBb orbit . . . . .	86
3.3.2	AaAb orbit . . . . .	88
3.3.3	Outer orbit A-B . . . . .	90
3.4	Short- and long-term future of the quadruple system . . . . .	94
3.4.1	Dynamical stability . . . . .	95
3.4.2	The transit of the disk in front of AaAb . . . . .	98
3.5	Discussion . . . . .	101
3.5.1	Comparisons with previous results . . . . .	101
3.5.2	Mutual alignment . . . . .	102
3.5.3	Formation history of HD 98800 . . . . .	104
3.5.4	The low mass ratio of AaAb and its lack of a disk . . . . .	105
3.6	Summary and conclusions . . . . .	106
3.7	Appendix . . . . .	108
3.7.1	Observations . . . . .	108
3.7.2	Orbital fitting complementary information . . . . .	109
3.7.3	N-body simulations . . . . .	109
3.7.4	Flux ratio estimation . . . . .	111
<b>4</b>	<b>Astrometrically resolved binaries</b>	<b>121</b>
4.1	Introduction . . . . .	121
4.2	AO-imaging astrometry . . . . .	122

## CONTENTS

4.3	Astrometry from infrared interferometry . . . . .	123
<b>5</b>	<b>Instrumentation</b>	<b>127</b>
5.1	Glossary . . . . .	129
5.2	Read Out Noise and NAOMI operations modes . . . . .	130
5.3	NAOMI performance simulations . . . . .	132
5.3.1	H-Band results . . . . .	133
5.3.2	K-Band results . . . . .	134
5.4	Commissioning and final results . . . . .	135
<b>6</b>	<b>Summary and conclusions</b>	<b>139</b>
<b>7</b>	<b>Future work</b>	<b>143</b>
7.1	Immediate work . . . . .	143
7.1.1	Full orbital characterisation of HD 98800 . . . . .	143
7.1.2	Dynamical masses for three young hierarchical systems . . . . .	144
7.1.3	Towards orbital solution for tight binary candidates . . . . .	145
7.2	Long-term work . . . . .	146
7.2.1	Determining the periods of spectroscopic binary systems . . . . .	146
7.2.2	The SACY sample . . . . .	146
7.3	Collaborations . . . . .	147
7.3.1	Disc transit of HD 98800 . . . . .	147
7.3.2	SPECULOOS . . . . .	147
<b>A</b>	<b>Appendix</b>	<b>149</b>
A.1	Publications related with this thesis . . . . .	149

## CONTENTS

A.1.1	Refereed . . . . .	149
A.1.2	Conference and Meeting proceedings . . . . .	150



# CHAPTER 1

## Introduction

### 1.1 The role of multiplicity in Star Formation

#### 1.1.1 Formation process of a single low-mass star

Molecular clouds are cold ( $\sim 10 - 20$  K) interstellar clouds, typically with sizes  $\gtrsim 1$  pc and masses  $\sim 10^3 - 10^4 M_{\odot}$  (Bergin & Tafalla 2007), but can be high as  $10^6 M_{\odot}$  for the so-called giant molecular clouds (Blitz et al. 2007; Molinari et al. 2014). Within molecular clouds there are denser regions called clumps. According to the virial theorem, the cloud expands if the force due to the gas pressure dominates over the force of gravity, whereas the cloud collapses if the kinetic energy is too low. The Jeans' mass,  $M_J$ , represents the minimum mass needed to start the collapse of the clump.

Following Shu et al. (1987), the star formation process can be described in six phases, represented in Fig. 1.1. The first phase is the development of dense cores inside molecular clouds. If a molecular clump gets cold and dense enough that its

mass is greater than the Jeans' mass, it collapses under gravitational free-fall<sup>1</sup>. This collapse is nearly isothermal as long as the cloud is optically thin (efficient cooling by molecular lines and dust grains radiation). Once central densities have exceeded  $\sim 10^{-13} \text{ g cm}^{-3}$  in the inner region, the collapse becomes adiabatic and the internal temperature and pressure increase dramatically (the core becomes optically thick and so line cooling is less efficient). Once the temperature and pressure of this inner region have become sufficiently high they can halt the free-fall collapse. The first hydrostatic core is formed (panel b in Fig. 1.1).

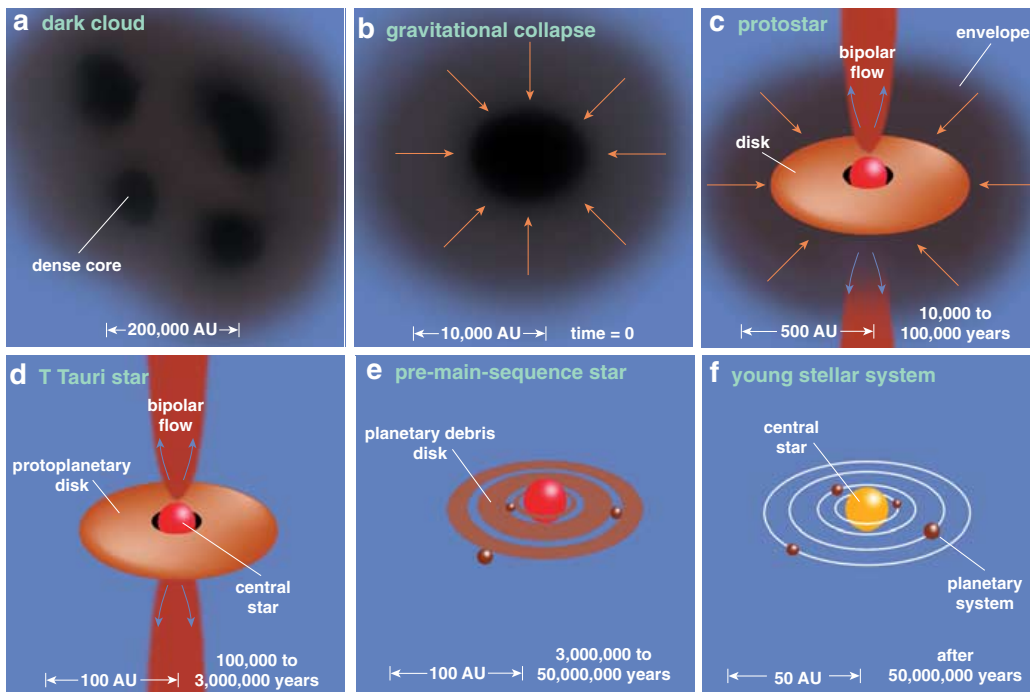


**Figure 1.1:** A schematic view showing the main stages of isolated low-mass star formation (Credit: Greene 2001).

When the core temperature reaches about 2000 K, the thermal energy dissociates the  $\text{H}_2$  molecules. The photon energy lost in this process results in a decrease of the gas pressure. Gravity dominates once again and free-fall collapse is reestablished. As a consequence of the conservation of angular momentum, an accretion disc is formed and bipolar outflow occurs (stage c in Fig. 1.1). After the density of in-falling material has reached about  $10^{-8} \text{ g cm}^{-3}$ , that material is sufficiently transparent to allow energy

<sup>1</sup> $t_{\text{ff}} = \left( \frac{3}{4\pi G \bar{\rho}} \right)^{1/2}$ , the free-fall time is the characteristic time that would take a body to collapse under its own gravitational attraction, if no other forces existed to oppose the collapse.

## 1.1. THE ROLE OF MULTIPLICITY IN STAR FORMATION

radiated by the protostar to escape. This radiative loss of energy allows the protostar to contract further. When the density and temperature are high enough, deuterium fusion begins, and the outward pressure of the resultant radiation slows down the collapse. The stellar magnetic field collimates the material ejected from the protostar into jets and bipolar outflows, which can remove angular momentum from the system (Appenzeller & Mundt 1989). Once the material in the envelope has either settled onto the accretion disc or been dissipated by the strong outflows, the star is now observable at visible wavelengths (see panel d in Fig. 1.1). This stage of evolution is referred as the T-Tauri stage for low-mass stars ( $< 2 M_{\odot}$ ). As the disc evolves rapidly (a few Myr), the gas is cleared from the inner disc, the accretion stops and planets can form from the remaining material<sup>2</sup>. While it contracts, the T-Tauri star decreases in luminosity given it has a smaller surface area to emit light. This contraction produce a change in temperature that is minimal compared to the change in luminosity, visible as a nearly vertical track on the Hertzsprung–Russell diagram. This luminosity-temperature relationship for low-mass pre-main sequence stars evolution is known as the Hayashi track (Hayashi 1961). The star continues to contract and its core temperature increases until it ignites hydrogen. At this stage the star halts further contraction and reaches the main-sequence (MS).

This is a simplified overview of isolated low-mass star formation. However, it is now accepted that almost 50% of solar-like star have at least one companion (Raghavan et al. 2010; Tokovinin 2014a,b), and this multiplicity rate is even higher at younger ages (Tobin et al. 2016; Elliott & Bayo 2016). Therefore, the study of star formation cannot be understood in isolation without studying the formation of multiple stars.

### 1.1.2 Formation of multiple star systems

The two major theoretical channels proposed for low-mass binary star formation are disc instability (Bonnell & Bate 1994) and core fragmentation (Boss 1986). The disc instability mechanism occurs in the disc surrounding a forming star and is triggered by density perturbations. A sufficiently massive disc is susceptible to gravitational instabilities, which trigger the disc fragmentation that can form companions around the protostar (see Kratter & Lodato 2016, for a recent review on gravitational instabilities).

---

<sup>2</sup>Recent observations suggest that planets could form even earlier (stage d on Fig. 1.1), as seen in recent observations of HL Tau (ALMA Partnership et al. 2015) or PDS 70 (Keppler et al. 2018).

## CHAPTER 1. INTRODUCTION

The fragmentation stops when the gas becomes opaque and heat adiabatically, this is the so-called opacity limit to fragmentation and constrains the minimum companion separation  $\sim 10$  au (Larson 1969; Vaytet, N. et al. 2012). Given the spatial scale of the disc, these close stellar companions are generally formed with initial separations  $\sim 50 - 200$  au (Bonnell & Bate 1994; Kratter et al. 2010; Zhu et al. 2012).

Core fragmentation is a direct consequence of hierarchical clouds collapse (Vázquez-Semadeni et al. 2019), where protostars are born from local over-densities in a collapsing cloud (Lee & Song 2019). Two protostars born in the same filament can be gravitationally bound if their relative velocity is less than the escape velocity of the system, forming a wide binary. A binary formed by core fragmentation can migrate inward as it evolves and accretes more gas (Lee et al. 2019). Accretion driven migration can lead to similar systems compared to the disc instability scenario, therefore erasing traces of its initial formation mechanism, and can reproduce the overall properties of close binary population (Tokovinin & Moe 2020). In cluster environments, dynamical interaction with other stars and binaries can alter the binary or multiple star formed by the elementary mechanisms mentioned above. In dense environment, the gas-assisted capture of accreting protostars is the dominant binary formation channel (Bate 2019).

Multiple systems can have many configurations, and recent theoretical studies have presented possible formation scenarios that could explain some of the observed architectures (see Tokovinin 2021, for a recent review on the architecture of multiple stellar systems and their proposed formation scenarios). In the formation of a close binary due to disk instability, another partner can be formed by the same mechanism in the outer regions of the disks, which leads to triple compact systems (Tokovinin & Moe 2020). Simulations by Lee et al. (2019) found that close binary, formed by either disc or core fragmentation, can capture another distant component, also producing a triple system. Similarly, the encounter of two forming binaries can produce a triple system with one component being ejected if the encounter is not moderated by gas (Ryu et al. 2017). The dynamical interactions between 3 or more components in an unstable configuration can form tight inner binaries with an outer tertiary bound companion, or even eject the tertiary component (Reipurth & Mikkola 2012). In the formation of triple systems by disc fragmentation, the growth of the third companion can be slowed down if a fourth outer companion forms in a larger separation, creating a 3+1 quadruple system. On the other hand, the collision of two protostellar cores creates a shock front that can trigger the collapse of each core into binaries and produce a

2+2 quadruple systems (Whitworth 2001). Multiple star systems with  $n > 2$  are nearly always hierarchical (Tokovinin 2018c), meaning that they can be decomposed into binary or single sub-systems based on their relative separations (e.g. two close binaries that orbit each other with a wide separation). Hierarchical systems can have many distinct configurations and it is thought that they are formed by the interplay of the elementary channels described above and further altered by gravitational interactions.

Nonetheless, there is no reliable or “unified” model of multiple star formation available yet, future improvement in the understanding of multiple star formation will be reached by the comparison between theoretical models and observations.

## 1.2 Observational studies on stellar multiplicity

### 1.2.1 The field populations

For solar-type MS stars, one of the first modern study is the work by Duquennoy & Mayor (1991) on a volume-limited sample of 164 objects in the solar neighbourhood. Duquennoy & Mayor (1991) found that about 50% of solar-type MS stars “live” in a binary system, this result was later revisited with a larger sample of 454 stars and updated to 46% by Raghavan et al. (2010). More detailed multiplicity statistics over different mass ranges and environment have revealed that multiplicity increases with stellar mass (over 70% for O stars, Sana et al. 2012), and also depends on density, temperature, and metallicity of the formation environment (Duchêne & Kraus 2013; Moe & Di Stefano 2017). However there is still not the same consensus in the community regarding the multiplicity for the lower end of the mass function. For instance, Fischer & Marcy (1992) published a multiplicity fraction of about  $42\% \pm 9\%$  for nearby M dwarfs (with mass ratio  $0.2 < q < 1$  and separation  $0 < a < 10,000$  AU) and Ward-Duong et al. (2015) estimated a companion star fraction of  $23.5\% \pm 3.2\%$  over a wide region of the parameter space ( $3 < a < 10,000$  AU,  $0.2 < q < 1$ ). Recently, Winters et al. (2019) found similar multiplicity fraction ( $\sim 26.8\%$ ) and companion fraction (32.4%) in a survey of 1,120 M-dwarfs up to 25 pc and Susemihl & Meyer (2021) calculated a binary fraction of  $22.9\% \pm 2.8\%$  over a constrained region ( $0.6 \leq q \leq 1.0$  and  $0 \leq a \leq 10,000$  AU). It is still necessary further studies surveying the binary fraction of M dwarf companions at low-mass ratios and exploring the relation between the mass of the companion and the orbital separation distribution over a wider parame-

ters space.

These large multiplicity surveys also revealed that stellar systems containing three or more stars are common. In the study of solar-type star within 25 pc of the Sun published by Raghavan et al. (2010), the fraction of triple star systems was found to be  $\approx 8\%$  and it drops to  $\approx 3\%$  for higher multiplicity systems. The volume-limited sample of Tokovinin (2014a,b) studied 4947 F and G dwarfs within 67 pc of the Sun and showed that  $\approx 10\%$  of stellar systems are triple and  $\approx 4\%$  are quadruple. Lately, the triple and higher multiplicity fraction was found to be  $\approx 17\%$  in a solar-type sample within 25 pc (Hirsch et al. 2021), larger than the aforementioned studies. This difference comes mainly from the discovery of new sub-systems in known binaries using high-resolution imaging. A large observational program has been monitoring multiple stellar systems covering a wide range of orbital parameters and increasing the sample of known hierarchical system (almost 3000) in the Multiple Star Catalog (MSC, Tokovinin 2018c). It is expected that different formation mechanisms leave their imprints on the mass ratios, periods, eccentricities and mutual orbit inclinations of hierarchical systems (Kozai 1962; Lidov 1962; Sterzik & Tokovinin 2002; Lee et al. 2019). Constraining these orbital parameters could provide additional information to understand multiple star formation. Based on the architecture of hierarchical systems in the MSC, Tokovinin (2021) classified the different architectures within these systems and presented possible formation scenarios, highlighting that the star formation is a process more than an event.

Most of the large, unbiased and complete surveys are focusing on fully formed MS populations. This raises the question of whether the high multiplicity fractions seen are primordial or a result of interactions throughout the evolution of the star. The formation channels of multiple systems can not be determined only by characterising field stars, where environmental key factors are not present anymore and billions of years of dynamical evolution may have erased their formation history. Therefore, the study of young ( $\sim 1 - 100$  Myr) multiple systems is an important step to improve our understanding of the formation and dynamical evolution of multiple systems.

## 1.2.2 Star forming regions and other young populations

The statistics of MS populations do not fully reveal the origin of multiple systems, there are many dynamical processes between the star formation stages (Myr time

## 1.2. OBSERVATIONAL STUDIES ON STELLAR MULTIPLICITY

scales) and the time when MS populations are observed in the solar neighbourhood (Gyr and later). Then, to understand the formation and the subsequent evolution of the primordial multiplicity we need to study young ( $\lesssim 100$  Myr) populations. Duchêne & Kraus (2013) provide a comprehensive review of stellar multiplicity across mass and age, including star-forming objects.

Protostars are traditionally categorised based on their spectral energy distribution. Class 0 sources are the least evolved objects, with more mass in circumstellar material, mostly in the form of a dense envelope, than in the central object. On the other hand, the envelope mass of Class I sources is lower than that of the central object, visible in the near- and thermal infrared in contrast to Class 0 source that are detected only the far-infrared and sub-millimeter domain. Classical T-Tauri stars with accretion disc correspond to Class II objects, and weak line T-Tauri stars with weaker or no circumstellar disc are referred as Class III. Every category have an associated evolutionary timescale, in the order of  $10^4$ ,  $10^5$ ,  $10^6$  and  $10^7$  years for Class I, II and III, respectively (Dunham et al. 2014). To date, a set of wide separation ( $> 1000$  au) Class 0 sources have been observed (Maury et al. 2010; Chen et al. 2013; Lee et al. 2017). Class 0 binary or multiple systems are of particular interest since they are too young to have experienced migration from their birth positions. Two millimeter and sub-millimeter interferometry surveys of Class 0 sources found that protostellar multiplicity is higher than that of the field population, however they disagree on whether increase or decrease from Class 0 to Class I stage (Maury et al. 2010; Chen et al. 2013). Another advantage of study Class 0 and Class I multiple systems is to characterise their gas environment and thereby identify if they are created by disc or turbulent fragmentation. Recently, the VANDAM<sup>3</sup> survey of protostars in Perseus studied 17 multiple sources (9 Class 0 and 8 Class I). In eight out of the 12 cases gas velocity information points to disc fragmentation, while the other 4 system are better modelled by a variant of turbulent fragmentation (Tobin et al. 2018b). A variety of surveys have been conducted in nearby star formation zones to obtain a better statistical sample of the younger multiple systems (Reipurth et al. 2014). In the future, the ngVLA project will improve the protobinary statistics extending the volume-limited sample to about 1.5 kpc with  $\sim 0.01''$  at wavelengths between 2 cm and 3 mm (Tobin et al. 2018a).

Binary surveys of low-mass young stellar objects in the Taurus cluster found a very high companion frequency (65 – 89%, Kraus et al. 2011). In contrast, a much

---

<sup>3</sup>VLA/ALMA Nascent Disk and Multiplicity (VANDAM).

lower companion frequency was found in denser clusters like the Orion nebula Cluster, ONC ( $< 10\%$ , Köhler et al. 2006; De Furio et al. 2019). These results raise the question of whether the environment play a role for the population of binaries and multiple systems. To answer that question, the so called young moving group or young association (for a review see Torres et al. 2008) are great candidates due to their proximity ( $< 200$  pc) and age (5 – 100 Myr). Their range of ages and distance, provide us with outstanding laboratories to study multiple star formation, and given their low density they undergone to a low dynamical processing providing valuable information about their primordial multiplicity. A recent study identified the spectroscopic binaries ( $< 1$  au, Elliott et al. 2014), close visual binaries (3 – 1000 au, Elliott et al. 2015) and wide and extremely wide binaries (1000 – 100,000 au, Elliott et al. 2016a) in the young associations within the SACY project<sup>4</sup>. They compared their multiplicity results with other PMS population such as Taurus (Kraus et al. 2011; Daemgen et al. 2015) and also older field population (Tokovinin 2014a,b), finding good agreement between the regions assuming a primordial companion fraction  $\approx 1$ , i.e. that on average, every star has one companion in its early stages. Later, studies by Elliott & Bayo 2016 ( $\beta$ -Pictoris moving group) and Joncour et al. 2017 (Taurus) suggest that the majority of very wide binaries ( $> 1000$  au) have primordial origin and were formed by the structure fragmentation of the natal cloud, where these wide systems are usually hierarchical multiples that decay with time on their evolution to the MS. This scenario could reconcile the apparent excess of very wide companions in young groups to the field, supporting a universal multiplicity scenario, and assuming a significant dynamical interaction and migration. However, King et al. (2012) study the multiplicity fraction at seven nearby star forming regions and found binary fraction to be decreasing with stellar density and an excess of close young binaries (10 – 100 au) compared to the field stars. More recently, Duchêne et al. (2018) also found an excess ( $\sim 20\%$ ) of close companions (10 – 60 au) in the ONC relative to the field suggesting a different formation mechanism. Similarly, Tokovinin et al. (2020) found a larger companion frequency at small separation ( $< 100$  au) and large mass ratio ( $q > 0.3$ ) for low-mass stars in Upper Scorpius (USco) star forming region compared to the field. Given that these close binaries are unlikely to be destroyed by dynamical interactions, Tokovinin et al. (2020) concluded that multiple star formation is not universal, and by extension, star formation process is not universal. Much remains to be done in multiplicity studies in

---

<sup>4</sup>Search for Association Containing Young Stars (SACY), see Torres et al. (2006).

pre-main sequence (PMS) populations, specially for spectroscopic binaries (SB). The only systemics studies are the ones by Melo (2003) and Elliott et al. (2014), resulting in a SB fraction  $\approx 10\%$ , but dominated by low number statistics. None of these studies has followed it up campaign in the last years to improve the epochs coverage. Future studies on multiple systems statistics in young populations are expected specially after the publication of the Gaia data release 3 (Gaia DR3<sup>5</sup>).

### 1.3 Dynamical masses

The mass is one of the fundamental parameter of a star, but unfortunately it is very difficult to estimate directly from observations (later we will discuss which methods can be used). In most cases, astronomers use mass-luminosity relationships as a proxy for the stellar masses (Wang & Zhong 2018). The stellar mass is a crucial parameter as it will define the temperature, surface gravity, and lifetime of the star from its formation to end. By placing a star with well determined  $T_{\text{eff}}$  and luminosity on the Hertzsprung–Russell diagram (HRD) and comparing those values to evolutionary tracks and isochrones models (e.g. Pietrinferni et al. 2004; Baraffe et al. 2015), astronomers can estimate its mass by assuming an age. The HRD fitting approach and mass-luminosity relationships work reliably when applied to MS stars given that the theoretical models are relatively well calibrated using dynamical masses measurements (Halbwachs 1986; Henry & McCarthy 1993; Malkov 2007, see later). However, the stellar evolutionary models are still far from delivering accurate predictions for PMS stellar masses; indeed a tendency has been found that such models underestimate the masses of stars by about 20 – 30% (Mathieu et al. 2007; Rodet et al. 2018; Simon et al. 2019) and this discrepancy increases especially for low-mass stars ( $< 0.5 M_{\odot}$ , Close et al. 2005; Sheehan et al. 2019; Pegues et al. 2021), which have strong convection, rotation and magnetic activity (Mathieu et al. 2007). This underestimation of the masses from models could lead to an overestimation in the frequency of brown dwarfs and planetary mass objects in young stellar clusters. This overestimation could affect studies on the mass distribution of young population like the initial mass function (e.g. IMF in Taurus star forming region, Briceño et al. 2002), which is generally derived from studies of volume-limited samples and using evolutionary models to estimate the stellar masses. Studies on the IMF are of great importance to understand

<sup>5</sup><https://www.cosmos.esa.int/web/gaia/dr3>

the star formation process. By comparing the IMF of different star forming regions it is possible to investigate whether the IMF is somehow “universal” (Elmegreen 1997) or if the environmental conditions could influence the IMF (Larson 1985).

The question therefore is, how can we actually determine stellar masses without relying too heavily on models? There are three model-independent methods to estimate stellar masses that are commonly used by astronomers. One of these methods relies on observing astrometric microlensing events (Paczynski 1991, 1996). Astrometric microlensing describes the time-dependent light centroid shift of a background star by an intervening stellar object (the lens). Recent works demonstrated the potential of astrometric microlensing to measure the mass of a single star with a precision of  $\sim 5 - 10\%$  (Sahu et al. 2017; Zurlo et al. 2018). These events can be predicted for stars with known proper motions, and the Gaia mission (Gaia Collaboration et al. 2016, 2018, 2021) can provide the measurements with the precision necessary to predict and measure these astrometric deflections. Klüter et al. (2020) predicted that Gaia can measure astrometric deflections for 114 events within the Gaia mission timescale (2014.5 - 2026.5), and a precision of 30% or better can be reached for at least 34 systems. However, the randomness of these events presents a disadvantage with respect to other methods that can be planned in a more systematic way on known young populations.

The second method relies on observing pre-MS stars hosting gas-rich circumstellar discs to obtain dynamical masses. As long as the disc is sufficiently inclined with respect to the line of sight, the rotation profile of some molecular line emission (e.g., CO), can be used to estimate the stellar mass (Sheehan et al. 2019; Pegues et al. 2021). Since the disc mass is small compared to the central star, the gas should rotate at Keplerian velocity (though deviation from Keplerian rotation is expected as the gas is self-supported by its own pressure). Modelling the resulting double peak profile (one part of the emission is blue-shifted while the other one is red-shifted), it becomes possible to determine the mass of the central object dynamically. This technique does not require multiple epochs of observations, and the free parameters are the stellar mass, the inclination of the disk, and an estimation of the radial distribution of the gas.

However, the most common approach to calculate dynamical masses has been through the determination of the orbital parameters of binary stars (see Fig. 1.2, for more detail see Hilditch (2001) and Sec. 3.3). For binaries whose components have been astrometrically resolved, it is possible to follow-up the relative motion of the sec-

ondary component with respect to the primary. With sufficient orbital coverage, we can obtain the orbital solution for the system (Pourbaix 1998; Hilditch 2001). If the distance of the binary from earth is known, then the total dynamical mass (i.e.  $M_1 + M_2$ ) can be calculated using Kepler's third law.

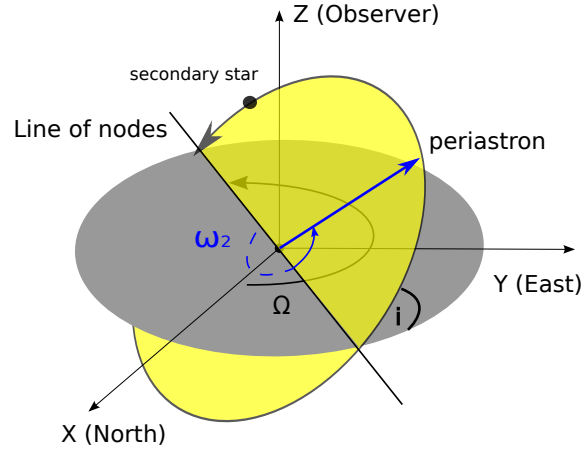


**Figure 1.2:** Diagram of the orbit of the secondary star around the centre of mass (yellow plane) and the reference plane (grey). This diagram follows the orbital convention of exoplanet<sup>7</sup>(credit: Zúñiga-Fernández et al. 2021b).

Furthermore, the radial velocity of the components of a binary system can be measured from optical spectroscopic observations using the Doppler shifts of atomic lines (typically ionised metals, for more details see Lindegren & Dravins 2003). From these measurements we can further constrain some of the orbital elements, i.e. the period, eccentricity, argument of periastron, semi-amplitude, systemic velocity and time of periastron passage (Hilditch 2001). For a single-line spectroscopic binary (SB1), where only the periodic variation of the primary star is observed, the mass-ratio of the components is degenerate with the inclination and then it is not possible to obtain a model-independent measurement of the masses. For double-lined spectroscopic binaries (SB2), where the radial velocity variation is observed for both components, the mass-ratio can be determined from the inverse ratio of the radial velocity semi-amplitudes,  $M_2/M_1 = K_1/K_2$ , where  $K_1$  and  $K_2$  are the radial velocity semi-amplitude of the primary and secondary components respectively. From SB2 orbits we can only estimate

<sup>7</sup><https://github.com/exoplanet-dev/exoplanet>

the minimum mass of each component (Hilditch 2001). The combination of the spectroscopic and astrometric measurements provide a more complete orbital solution (see Murray & Correia 2010; Gallenne et al. 2019; Chap. 3). If the system is an SB2 and if we have enough astrometric points, it is then possible to obtain the distance to the system and the distance-independent dynamical masses for each individual star (more details in Sec. 3.3.1). In the case of an SB1 system with astrometric measurements, it is necessary to assume a distance to obtain the dynamical masses of each binary component (more details in Sec. 3.3.2).

Once the stellar masses have been estimated using one of the method described above, we are then able to confront these estimates to evolutionary models. Simon et al. (2019) compared magnetic and non-magnetic evolutionary models and found that evolutionary models of PMS that include magnetic fields (such as the ones presented in Feiden 2016) provide mass estimates that are more consistent with model-independent dynamical masses measurements estimated by disc rotation using ALMA observations (second method described above). Another aspect that should not be neglected are the magnetically induced star-spots, which can lead to discrepancies in the estimated temperatures between optical and infrared observations. Comparisons between temperatures estimated from infrared spectroscopy and literature temperatures estimated from optical photometry showed a difference between 200 – 800 K, where stars with stronger magnetic activity have larger temperature differences (Flores et al. 2021). These discrepancies lead to differences in the masses estimated from PMS evolutionary models, since those models require an estimate of the temperature (among other parameters) to constrain the mass. Flores et al. (2021) estimated stellar masses using both the temperatures derived from infrared spectroscopic observations and optical photometric observations using the stellar evolutionary models from Feiden (2016). They compared both results with dynamical masses estimated from the Keplerian rotation, and found that both masses estimated using the evolutionary models showed discrepancies compared to the dynamical masses. But on average the masses inferred from temperatures derived using infrared spectroscopic observations were more precise ( $\sim 30\%$  error instead of  $\sim 90\%$  for optical observation), especially for low-mass stars ( $\lesssim 0.5 M_{\odot}$ ). Similarly, Pegues et al. (2021) compared dynamical masses of PMS low-mass stars ( $< 0.5 M_{\odot}$ ) obtained with ALMA with evolutionary models that do not include magnetic field activity and found that the models underpredicted masses by 60 – 80%. Pegues et al. (2021) suggested that

this discrepancy could come from of inaccurate estimation of stellar effective temperatures or the lack of magnetic activity in the evolutionary models. These results suggest that stellar-spots and magnetic activity effects need to be taken into account in evolutionary models, especially for low-mass stars. However, it is still necessary to test the reliability of magnetic models on a larger sample with dynamical masses smaller than  $0.4 M_{\odot}$ . The aforementioned studies estimated the dynamical masses by disc rotation using ALMA observations, however this technique has some limitations if we were to use it on a larger sample. Indeed, given the substantial amount of gas necessary to obtain a clear detection of the emission line, this technique remains limited to Class II stars (panel d in Fig. 1.1). On the other hand, determining the dynamical masses from binary systems can also be applied for MS systems and both Class II and III young stars. Though, one should keep in mind that the disc rotation technique can perfectly be used for single stars, while the dynamical masses from the orbital motion is obviously restricted to binary stars. Therefore, for the goal to obtain dynamical masses in young populations these techniques are very complementary.

Evolutionary models do not only provide estimates of the masses but also of the stellar ages. The need for mass estimates to test and calibrate PMS evolutionary models is therefore crucial to also constrain the latter parameter. For example, the age of the M-type secondary or tertiary in young multiple systems, estimated from evolutionary models (with no magnetic field included) and dynamical masses from their orbital solutions, was found to be  $\sim 2 - 3$  Myr younger than their G-type companions (Rizzuto et al. 2016, 2020), indicating calibration issues and systematic errors in PMS evolutionary tracks for low-mass stars. Similarly, the ages of stars estimated from models that include magnetic fields were  $\sim 3 - 7$  Myr older than the ages obtained with models that do not account for such effects (Simon et al. 2019). As discussed earlier, Simon et al. (2019) found that evolutionary models which include magnetic fields lead to masses that are more consistent with dynamical masses in the Taurus star forming region. Therefore, ages of stars estimated using models include magnetic fields should be more reliable. These older ages ( $\sim 3 - 10$  Myr, instead of  $1 - 3$  Myr) mean that, for example, gaseous discs could survive longer than what is currently expected and, as a consequence, that giant gaseous planets may have more time to accrete their gas. The ages of young stellar objects are used to infer the timescales for the dissipation and evolution of their discs (Simon & Prato 2019), exoplanets formation and migration (Kraus & Ireland 2012; Mann et al. 2016), and rotational evolution

(Douglas et al. 2016). Model independent measurements of PMS stellar masses are therefore crucially needed to better calibrate the evolutionary models.

From the previous discussion, it should therefore be clear that the orbital characterisation of binaries is a powerful method to directly constrain stellar masses that can be used to calibrate evolutionary models, especially for PMS stars and in the low-mass regime (Stassun et al. 2014; Nielsen et al. 2016; Rodet et al. 2018). However, as we discussed previously, this calibration could be limited by uncertainties on the ages (especially in the low-mass regime) and distances of the systems. For systems that are members of young nearby associations or young moving groups, these uncertainties are greatly mitigated. The ages of young associations are often inferred by several approaches (lithium depletion, kinematics, etc, see Zuckerman et al. 2004; Torres et al. 2008) and the distances are now accurately determined from the latest Gaia release (Gaia Collaboration et al. 2018, 2021).

The SACY sample (Search for Associations Containing Young stars), originally presented in Torres et al. (2006) and Torres et al. (2008), is a collection ( $\approx 600$  objects) of nearby ( $< 200$  pc) young ( $\sim 5 - 100$  Myr) stars, free of extinction. Recently, comprehensive multiplicity studies within the SACY sample have identified spectroscopic binaries (Elliott et al. 2014), visual binaries (Elliott et al. 2015), and wide and extremely wide binaries (Elliott et al. 2016a). The age range covered by our sample is of particular interest to determine dynamical masses. In that regard we have identified a subset of low-mass targets in our sample with orbital periods shorter than a decade. Our collection of observational data includes high resolution spectroscopic, adaptive optics imaging and long-baseline infrared interferometric observations. As most PMS stars reside in clusters ( $> 140$  pc) very few PMS binaries have well characterised orbital solutions due to the very long orbital periods accessible for direct imaging at those distances. Given the proximity of our targets, a large and continuous orbital parameter space can be covered when combining different observational techniques. The targets presented in this work are therefore precious benchmarks and full orbital solution will provide very good young calibrators for comparison with PMS stellar evolution theory.

## 1.4 Organisation of the thesis

The remainder of this thesis is organised using the projected separation of the binary systems in our sample as a criteria to move between chapters. We started from tight binaries and then transitioned to wider separations as we progress through the thesis.

In Chapter 2 we present an update of the spectroscopic binary population in the young associations in our sample. The updated binary fraction is compared with other regions and discussed in the context of universal star formation. One of those spectroscopic binary, which is actually a quadruple systems called HD 98800, was characterised using long-baseline infrared inteferometry in Chapter 3. We obtained a new orbital solution for this quadruple system and we calculated the dynamical masses of its components. The results was compared with previous works from the literature and discussed in the context of formation of multiple star systems. Switching from tight binary systems to close and intermediate separations, in Chapter 4 we presented the work in progress to obtain dynamical masses using astrometrically resolved binaries using Adaptive Optics imaging and long baseline interferometry observations. We presented the astrometric measurements of these binary systems and we discussed the perspectives of these results and the future work necessary to obtain a full characterisation of their orbits and the dynamical masses. In Chapter 5, we describe the instrumentation project developed for the new adaptive optics module for interferometry (NAOMI<sup>8</sup>). We present the work carried out during the three month research stay at IPAG (France), the subsequent commissioning campaign in Paranal and the application for observing time in the Scientific Verification call. We discussed the results obtained during the commissioning campaign and the relationship of this experience with the work developed in Chapter 3. We present the summary and the overall conclusions from the work presented in this thesis and the future prospects of research in Chapter 6 and Chapter 7 respectively.

---

<sup>8</sup><https://www.eso.org/public/teles-instr/paranal-observatory/vlt/vlt-instr/naomi/>



## CHAPTER 2

# An updated census of spectroscopic binaries in SACY

This chapter have been previously published as “Search for associations containing young stars (SACY). VIII. An updated census of spectroscopic binary systems exhibiting hints of non-universal multiplicity among their associations” Zúñiga-Fernández, S., Bayo, A., Elliott, P., Zamora, C., Corvalán, G., Haubois, X., Corral-Santana, J. M., Olofsson, J., Huéramo, N., Sterzik, M. F., Torres, C. A. O., Quast, G. R., and Melo, C. H. F. *A&A*, 645, A30 (2021).

### 2.1 Introduction

Ever since the first nearby young moving group of stars was identified around 30 years ago (TW Hya association, de la Reza et al. 1989; Kastner et al. 1997), extensive research has been dedicated to these stellar associations – from identifying new ones and their members to characterising their chemical composition, dynamics, ages, and multiplicity fractions (see Zuckerman et al. 2004; Torres et al. 2008; Shkolnik et al. 2012; Malo et al. 2014; Elliott & Bayo 2016; Gagné et al. 2018a, among others). These nearby populations, given their age ( $\sim 5 - 150$  Myr) and proximity ( $< 200$  pc), are great laboratories for the study of the properties of young stellar and substellar objects.

Recent studies have used youth signatures (such as the presence of  $H\alpha$  in emission or the detection of the  $\text{Li } \lambda 6707 \text{ \AA}$  line) and 6D kinematics (i.e. Galactic position and Galactic velocity in the six-parameter space, XYZ and UVW) to estimate membership (Schneider et al. 2019; Lee & Song 2019). In this context, multiplicity studies (particularly the search for tight binaries) play an important role since age diagnostics, velocity determinations, and astrometry are often affected by the application of single-star models to blended multiple systems.

More generally speaking, stellar multiplicity is important in a broad range of fields (e.g. supernova rates), however, here we focus on its impact on the star-formation processes. Works on multiplicity as a function of environment, along with detailed studies of composition and orbital parameters, provide valuable empirical data that improve our understanding of stellar evolution and unresolved stellar populations. These empirical estimates are of particular interest at younger ages and close separations, where theoretical models still remain only loosely constrained (Duchêne et al. 2007; Connelley et al. 2008; Tobin et al. 2016) and the literature in this field is still lacking in comparison to the more exhaustive work done for main-sequence (MS) stars with volume-limited samples (Tokovinin 2014a; Tokovinin & Briceno 2019; Tokovinin 2019; Sperauskas et al. 2019; Merle et al. 2020).

It is widely accepted that almost half of solar-type stars spend their time in the MS as multiple systems (Tokovinin 2014a; Raghavan et al. 2010). There is also growing evidence that multiplicity is even higher at very young ages (Tobin et al. 2016), possibly indicating the primordial nature of multiplicity in the processes of star formation. Observational studies suggest an overall decrease of the binary fraction from pre-MS ages to field ages (Ghez et al. 1997; Kouwenhoven et al. 2007; Raghavan et al. 2010). This decrease could be a consequence of disruption process in long-period systems due to interactions with other systems (Raghavan et al. 2010) or due to the dynamical evolution of wide companions in triple or higher order systems (Sterzik & Tokovinin 2002; Reipurth & Mikkola 2012; Elliott & Bayo 2016). In contrast with wide binaries, tight binaries are expected to ‘last’ longer given their larger binding energy. A number of observational results on tight binaries have indicated that the overall SB fraction remains unchanged after 1 Myr (Nguyen et al. 2012; Tokovinin 2014b; Elliott et al. 2014). However, more recently, Jaehnig et al. (2017) suggested that some SBs (periods  $\approx 10^2 - 10^4$  days) in pre-MS clusters ( $\approx 1 - 10$  Myr) can be dynamical disrupted prior to reaching the MS. The evolution and the formation channel of multiple stellar sys-

tems cannot be easily determined by field stars, where billions of years of dynamical evolution have already occurred. Therefore, it is necessary to devote specific studies of the stellar multiplicity from star-forming regions (SFRs) to the young associations (1 – 100 Myr).

The multiplicity studies for the youngest stars ( $\leq 100$  Myr) are still dominated by low number statistics. This is particularly critical in the case of SBs (sub-au separation scales) where high-resolution techniques are mandatory (Melo 2003; Nguyen et al. 2012; Viana Almeida et al. 2012), but some of these techniques can be contaminated by phenomena such as activity and rotation, inherent to the young ages involved (see Sect. 2.5). In principle, the preferred mechanism to form some of these close binaries ( $\lesssim 100$  au) is disk fragmentation, where the disk fragments as a result of gravitational instabilities (Bonnell & Bate 1994; Zhu et al. 2012). However, the formation mechanisms could be affected by environment conditions. In particular, Bate (2019) found an apparent trend for multiple systems to be preferentially tighter when formed at lower metallicity environments. On the other hand, the tightest systems ( $\lesssim 10$  au) can neither form directly via turbulent nor disk fragmentation, and the emerging consensus is that some processing must dynamically evolve the initial separations to closer ones (Bate et al. 2002). In particular, Tokovinin et al. (2006) found that  $\sim 63\%$  of MS SBs were members of high-order multiple systems (see Elliott & Bayo 2016 for a similar result focused on the  $\beta$  Pictoris moving group). Interestingly,  $\sim 98\%$  of SBs with orbital periods shorter than three days have additional companions. This result seems to provide observational support to the dynamical evolution hypothesis commented above. Further SB studies in younger population ( $\leq 100$  Myr) are, in any case, still needed to provide improved statistics on more pristine populations.

This work is the continuation of a series of studies of multiplicity in young associations over a wide range of orbital parameters ( $a \sim 0.1 - 10^4$  au: Elliott et al. 2014, 2015, 2016a; Elliott & Bayo 2016). In particular, this work focuses on SB identification within SACY via cross-correlation function (CCF), not only using the radial velocity (RV) variations with time as a sign of multiplicity, but also incorporating high-order features as a complementary tool to establish the origin of the variation. Following our modelling and upon applying observational bias corrections, we present the results on the SB fraction in each association within the SACY sample along with the list of SB candidates, including notes on individual objects.

## 2.2 Sample

The sample presented in this work is drawn from our database of young association members, as in Elliott et al. (2016a), mainly gathered from Torres et al. (2006); Torres et al. (2008); Zuckerman et al. (2011); Malo et al. (2014); Kraus et al. (2014); Elliott et al. (2014); and Murphy et al. (2015). The membership of each object to a given association was assessed using the convergence method described in Torres et al. (2006) and Torres et al. (2008) with the updated distances from the second Gaia data release (Gaia DR2, Gaia Collaboration et al. 2018). The full membership study and further analysis will be presented in Torres et al. (in prep.). In addition, the targets selected for this work have to fulfil at least one of the following selection criteria: 1. The objects have at least one high-resolution spectrum in our database from which a CCF can be calculated; 2. The target has at least one RV measurement (with uncertainty  $\leq 3 \text{ km s}^{-1}$ ) and one  $v \sin i$  value given in the literature (with uncertainty  $\leq 5 \text{ km s}^{-1}$ ).

Hereafter, this selection is referred as ‘the sample’ and obtained with the SACY convergence method unless otherwise indicated. Our sample covers an approximate mass range of  $0.1 - 1.5 M_{\odot}$ , with the majority of objects having an estimated mass around  $1 M_{\odot}$ . Masses were estimated from the 2MASS near-infrared magnitudes and parallactic distances using the evolutionary tracks from Baraffe et al. (2015). Our final sample size is 410 objects, 303 of which have two or more epochs of high-resolution spectra. Further details on the literature measurements used in our sample are summarised in Sect. 2.3.2, and all relevant parameters for this work are listed in Table 2.7.

## 2.3 Observations and additional data

We obtained spectra taken with the Ultraviolet and Visual Echelle Spectrograph (UVES;  $\lambda/\Delta\lambda \sim 40,000$  with a  $1''$  slit, Dekker et al. 2000) in Paranal, Chile. These observations came from three of our observing campaigns, taken between 2015 and 2016. We also added data retrieved from the ESO phase 3 public archive<sup>1</sup>. Our data were taken with a  $1''$  slit width in the wavelength range  $3250 - 6800 \text{ \AA}$ . The time separation between different observing epochs of a given source ranges from one day to  $\sim$ one month.

The data were reduced with the EsoRex<sup>2</sup> pipeline of UVES, using the

<sup>1</sup>[http://archive.eso.org/wdb/wdb/adp/phase3\\_main/form](http://archive.eso.org/wdb/wdb/adp/phase3_main/form)

<sup>2</sup><https://www.eso.org/sci/software/cpl/esorex.html>

*uves\_obs\_redchain* recipe (bias corrected, dark-current-corrected, flat-fielded, wavelength-calibrated and extracted). This provides three spectra from the two arms of the instrument (BLUE and REDL/REDU, with wavelength coverage 3250 – 4500 Å, 4800 – 5800 Å, and 5800 – 6800 Å, respectively). For the calculation of CCF in this work, we combined all three spectra in the case where the average signal-to-noise ratio (S/N) for the BLUE spectrum is  $> 10$ . Otherwise, we combined the REDU and REDL spectra only. In total, we present 998 individual CCFs from the UVES observations.

#### 2.3.1 Archival high-resolution spectra

In order to maximise the time baseline and available spectral information for each target, we used the publicly available phase 3 data taken with the Fibre-fed Extended Range Échelle Spectrograph (FEROS/2.2 m, Kaufer et al. 1999) and the High Accuracy Radial velocity Planet Searcher (HARPS/3.6 m, Mayor et al. 2003).

FEROS is a high-resolution Échelle spectrograph ( $\lambda/\Delta\lambda \approx 50,000$ ) installed at the MPG/ESO 2.2-m telescope located at ESO’s La Silla Observatory, Chile. The wavelength range of the reduced spectra is 3527 – 9217 Å. The one dimensional Phase 3 spectra are given in the barycentric reference frame. HARPS is also a high-resolution Échelle spectrograph ( $\lambda/\Delta\lambda \approx 115,000$ ), mounted on the 3.6 m telescope, also located at La Silla Observatory in Chile. The wavelength range is 3781 – 6912 Å and the phase 3 spectra are given in the barycentric reference frame.

We searched for any available science spectra for targets in common with our database of young moving group members. From all the archival spectra, we successfully calculated CCFs for 167 observations taken with FEROS and 97 CCFs for observations taken with HARPS. These data are also included in the analysis presented in this work.

#### 2.3.2 Previously published quantities

Table 2.1 lists the references used in this work for both the RV and  $v \sin i$  values. As mentioned previously, we only include values that have uncertainties  $\leq 3 \text{ km s}^{-1}$  and  $\leq 5 \text{ km s}^{-1}$  for RV and  $v \sin i$ , respectively. The table is split into two sections: the top one shows values that do not have associated Modified Julian Dates (MJD) values for each RV and the bottom section corresponds to surveys that do have individual MJD

values for each observation.

**Table 2.1:** Previous catalogues of RV and  $v \sin i$  values used in this work. The bottom section shows those values with associated MJDs, while the top section show values for which MJDs have been estimated from the respective MJD-range.

Ref.	Values	MJD-range	Ref. code
MJD estimated from observation range			
Schlieder et al. (2012)	RV, $v \sin i$	54718-55685	SC12
Shkolnik et al. (2012)	RV <sup>a</sup>	53725-54455	SH12
Torres et al. (2006)	RV, $v \sin i$	51179-53826	TO06
Lopez-Santiago et al. (2006)	RV <sup>b</sup>	51910-52796	LO06
Rodriguez et al. (2013)	RV	56171-56230	RO13
Maldonado et al. (2010)	RV	53552-54771	MA10
Moór et al. (2013)	RV	55013-55669	MO13
Reiners & Basri (2009)	RV	54475-54835	RE09
Gontcharov (2006)	RV	47892-52275	GO06
Exact MJD values available for each observation			
Malo et al. (2014)	RV, $v \sin i$	54996-56532	MA14
Kraus et al. (2014)	RV <sup>c</sup>	56124-56327	KR14
Montes et al. (2001)	RV	51384-51566	MO01b
Mochnecki et al. (2002)	RV	51082-52003	MO02
Bailey et al. (2012)	RV, $v \sin i$	53327-54963	BA12
Desidera et al. (2015)	RV, $v \sin i$	53102-55399	DE15

**Notes.** <sup>(a)</sup> Extended from Shkolnik et al. (2010), <sup>(b)</sup> Stars added to the initial sample of Zuckerman et al. (2004), <sup>(c)</sup>  $v \sin i$  values not used from Kraus et al. (2014) as these values are the standard deviation of the broadening function, not calibrated  $v \sin i$  values.

### 2.3.3 Gaia Data Release 2

The second Gaia data release<sup>3</sup> (hereafter, Gaia DR2) was issued on 25 April 2018, providing accurate proper motions and parallaxes (among other astrophysical parameters) for more than a billion sources. In particular, this Gaia data release also includes for the first time RV values (Katz et al. 2018) for objects with a mean G magnitude between  $\sim 4$  and  $\sim 13$  and effective temperatures ( $T_{\text{eff}}$ ) between 3550 and 6900 K. The overall precision of the RV at the bright-end is in the order of  $200 - 300 \text{ m s}^{-1}$ , while at the faint-end, it deteriorates to  $\sim 1.2 \text{ km s}^{-1}$  for a  $T_{\text{eff}}$  of 4750 K and  $\sim 2.5 \text{ km s}^{-1}$  for a  $T_{\text{eff}}$  of 6500 K. Stars identified as double-lined spectroscopic binaries are not reported in Gaia DR2, whereas variable single-lined, variable star, and non-detected double-lined spectroscopic binaries have been treated as single stars in the same release (Sartoretti et al. 2018).

We retrieved Gaia DR2 data for all the objects in the SACY sample using the astroquery VizieR package<sup>4</sup>. We updated our local database to use identifiers resolvable by the Sesame service and the Gaia DR2 queries were based on those identifiers. Objects not resolved by identifiers were instead searched by coordinates. In both cases we ran an initial query with a  $10''$  radius and used the proper motions of the closest Gaia source, within the radius, to derive its J2000 coordinates (that are those originally included in our local database). Those J2000 coordinates were then matched to the coordinates in our local database with a  $1''$  radius. Objects outside of this  $1''$  radius were individually inspected (see Fig. 2.19 in the Appendix) by cross validating using Simbad, VizieR and the TESS input catalogue (TIC-8, Stassun et al. 2019). We recovered Gaia DR2 counterparts for 805 out of 837 targets in our local database, corresponding to a completeness of 96.2% (see Fig. 2.1). From these 805 objects, 374 have RV measurements from Gaia, which were used in this work as an additional epoch of data. Our database comprises 2379 RV measurements and 1515  $v \sin i$  values, 1151 of which come from our CCF calculation of high-resolution spectra. All these values, together with other additional properties, can be found in Tables 2.4 and 2.5.

---

<sup>3</sup><https://www.cosmos.esa.int/web/gaia/dr2>

<sup>4</sup><https://astroquery.readthedocs.io/en/latest/vizier/vizier.html>

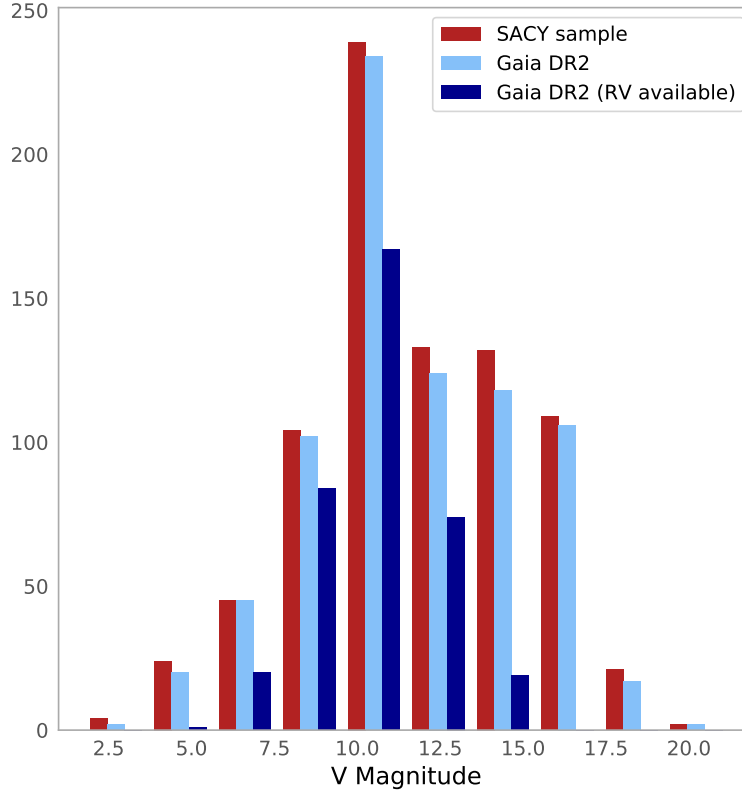


**Figure 2.1:** V-magnitude distribution of all members of the SACY sample along with those with a counterpart in the Gaia DR2. We reach a completeness of 96.2%, where 44.7% of the objects count based on a Gaia RV estimate.

### 2.3.4 Assessing membership using BANYAN $\Sigma$

In order to assess any possible bias throughout this work with the use of the convergence method to build the census of the different associations, we followed an independent path, utilising the BANYAN  $\Sigma$  tool<sup>5</sup> for young association membership.

Accurate RV, distances, and proper motion values are key ingredients in the accuracy of our convergence method (Torres et al. 2006; Torres et al. 2008). Similarly, the recovery rate of BANYAN  $\Sigma$  is 68% when proper motion and RV are used and 90% when parallaxes are included (Gagné et al. 2018a). Therefore, as we did for the convergence method, we fed the RV measurements collected in this work plus the Gaia DR2 proper motion and parallaxes to the BANYAN  $\Sigma$  tool for membership assessment.

It is out of the scope of this work to develop or establish a metric to compare in

<sup>5</sup>[https://github.com/jgagneastro/banyan\\_sigma](https://github.com/jgagneastro/banyan_sigma)

### 2.3. OBSERVATIONS AND ADDITIONAL DATA

detail the outcome of the two methodologies. However, the two resulting censuses allow us to test the robustness of our results against moderate changes in membership (see Sect. 2.8 for further details). The membership results for the SACY convergence method and BANYAN  $\Sigma$  are available in Table 2.7 and summarised in Fig. 2.2. The mass distributions of the samples analysed throughout this work (using either our convergence method or BANYAN  $\Sigma$  tool) are shown in the bottom panel of Fig. 2.2. As it can be seen, the only associations with noticeable differences regarding total number of members are ABD and THA.

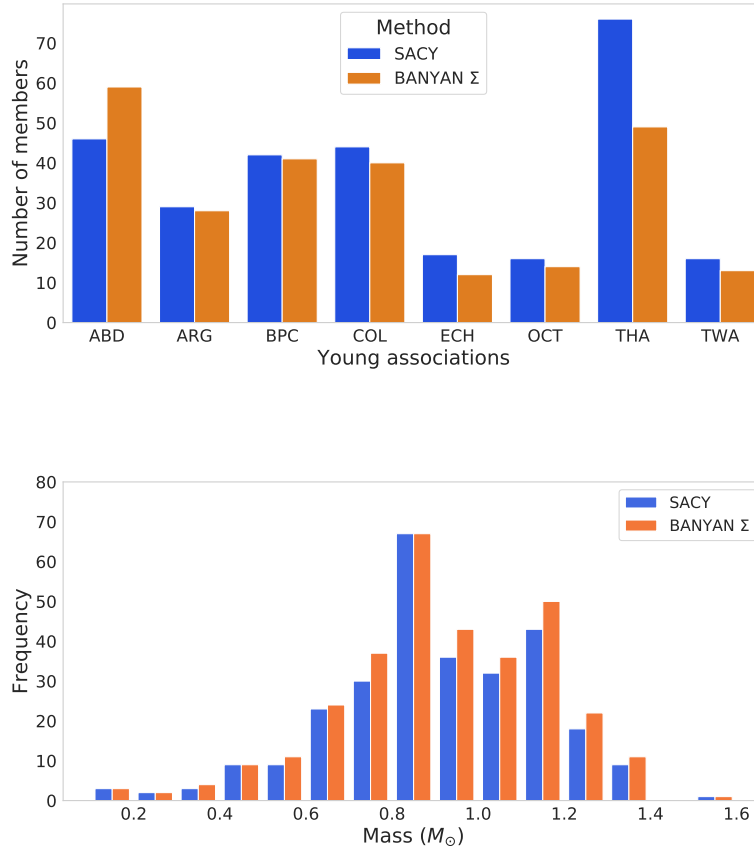


**Figure 2.2:** *Top:* Number of targets belonging to each young associations identified by our convergence method (SACY) and BANYAN  $\Sigma$ . *Bottom:* Mass function of the census built with the convergence method and BANYAN  $\Sigma$  for membership assessment.

### 2.3.5 Rotational periods from light curves

In order to estimate the rotational periods of the objects in the sample, we queried two of the main missions delivering precise light curves: K2 and TESS (Howell et al. 2014; Ricker et al. 2015). We began by querying the archives of both missions via the MAST API (via the `astroquery` package within `astropy`) with the J2000 coordinates of each object and a search radius of 0.002 deg ( $\sim 7''$ ). We obtained light curves for 272 out of 410 objects ( $\sim 65\%$  of the sample). In particular, 266 were taken with TESS (across different sectors) and six with K2. In all cases, we chose the Pre-search Data Conditioned Simple Aperture Photometry (PCDSAP) fluxes and characterised the variability of the sources via their Lomb-Scargle (LS) periodograms (calculated with `astropy.timeseries.lombscargle`, VanderPlas & Ivezić 2015).

Even though the false alarm probabilities (FAPs) of the peaks identified in the LS periodogram were extremely low (typically well below  $10^{-4}$ ), we performed a simple quality check for the identified periods in the following way: we folded each light curve to the period with the highest intensity in the LS periodogram and modelled the modulation by calculating the median, binning the phased curve in 100 bins. Such a trend was subtracted from the phased light curve and the median absolute deviation (MAD) of those residuals was compared to the MAD of the original phased light curve.

In the case of TESS data, additional checks need to be done to account for the large pixel size of its detector. In order to estimate the contamination that could affect each of the light curves, we modified the existing python package `tpfplotter` (Aller et al. 2020) which, in short, provides the number of Gaia sources within a  $\Delta G$  mag (Gaia  $G$  mag, this  $\Delta$  is defined by the user) of the science target that fall in the pipeline aperture of TESS. We modified the code in order to take into account both the proper motions of our targets and the cross-match with Gaia DR2 (explained in Sect. 2.3.3). We chose a  $\Delta G$  mag on the order of five magnitudes and in Table 2.7, we include notes on the minimum  $\Delta G$  mag found within the aperture. We note that a number (27 to be precise) of our Gaia cross-match identifications are not recovered in Simbad. Even though we stand by those identifications, we make note of them in the column *LC notes* of Table 2.7.

We classified a period as ‘good quality’ if the MAD of the residuals is at least three times smaller than the MAD of the original phased light curve and if there are no Gaia sources that fall in the aperture with  $\Delta G$  mag  $< 5$ . Periods that fulfil the criteria based

### 2.3. OBSERVATIONS AND ADDITIONAL DATA

on the MAD of the residuals but have contaminants in the aperture with  $2.5 \leq \Delta G \text{ mag} \leq 5$  should be considered with caution. For periods that present contaminants in the TESS aperture and do not fulfil the criteria based on the MAD are not considered as reliable for the rest of the analysis and are flagged as being of ‘bad quality’. For an example of a clearly contaminated light curve (rotational periods that are not to be trusted) see Appendix 2.11.6.

Our estimated periods as a function of median  $v \sin i$  from our work are presented in Fig. 2.3 (see the details regarding  $v \sin i$  estimation in appendix. 2.11.3). This relation was used throughout our analysis as a complementary source to evaluate the nature of SB candidates.

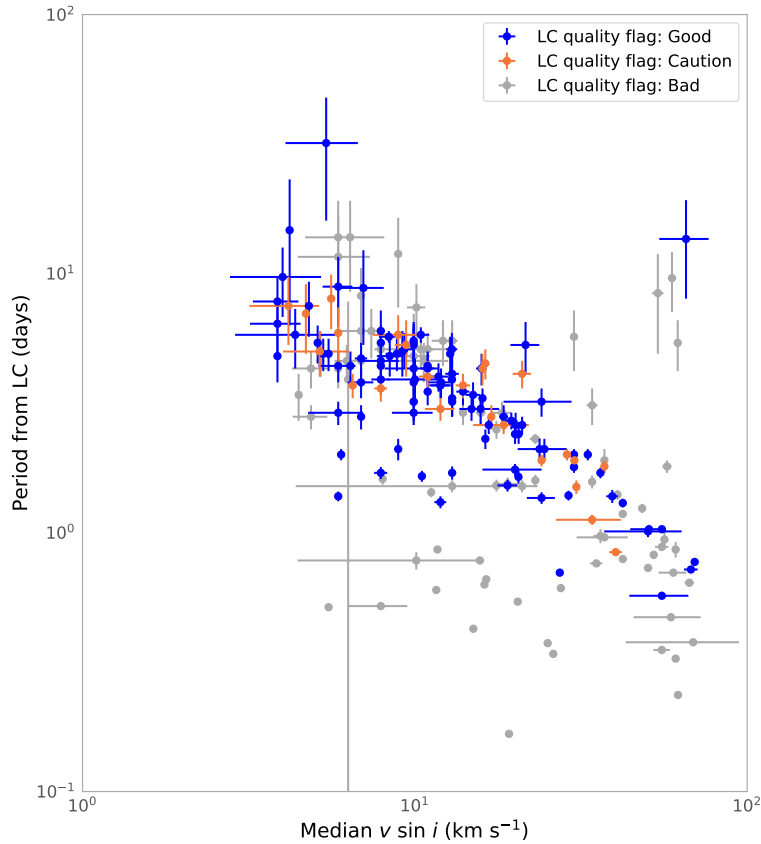


**Figure 2.3:** Rotational periods estimated from the light curves versus median  $v \sin i$  from our work. The quality flag of the period defined in Sect. 2.3.5, is colour-coded as grey, orange, and blue for ‘bad’ caution and ‘good’, respectively.

## 2.4 Properties and calculation of CCF profiles

There are two main ways of calculating CCFs from high-resolution spectra, using either observations of RV standard stars or a numerical mask acting as a standard star. In this analysis, we used a CORAVEL-type numerical mask which was convoluted with the observed spectrum for each observation (for further details, see Queloz 1995). For the sake of homogeneity and given the relatively narrow range of spectral types in our sample (see Table 2.7), we use a single K0 mask in our analysis.

Only in cases where the K0 mask completely failed in the CCF calculation (assessed by the goodness of fit of the Gaussian profile to the CCF), we used other available masks (F0 or M4, depending on the spectral type of the star). However, for consistency, the CCF profiles and respective properties of such objects are not included in the statistical analysis of our measurements.

The CCFs analysis and the SB update presented in this work follows up what was presented by Elliott et al. (2014). However, we do not only enlarge our database of observations here, but we have also chosen to use a much more detailed approach in calculating the CCFs for each observation; by introducing high-order features of the CCFs, we can distinguish between apparent RV variation caused by poor fitting of the CCF and variation produced by bound companions or stellar activity.

### 2.4.1 Sources of uncertainty

The uncertainty in RV calculation using a numerical mask ( $\sigma_{\text{meas.}}$ ) can be derived with the following equation (Baranne et al. 1996):

$$\sigma_{\text{meas.}} = \frac{C(T_{\text{eff}})}{D \times S/N} \frac{1 + 0.2\omega}{3} \text{ km s}^{-1}, \quad (2.1)$$

where  $C(T_{\text{eff}})$  is a constant that depends on both the spectral type of the star and the mask used, which is typically 0.04;  $\omega$  is the (noiseless) full width at half maximum (in  $\text{km s}^{-1}$ ) of the CCF;  $D$  is the (noiseless) relative depth, and  $S/N$  is the mean signal-to-noise ratio.

This uncertainty is relevant to one measurement of RV from a single observation and a single instrument. Given the high  $S/N$  of our data, typically in the range of  $\sim 50 - 100$ , the calculated uncertainty is almost negligible. A more empirical approach can be taken by studying the RV from different epochs and gauging the level of intrinsic variation of the star. As these stars are often variable, the CCF profiles are

not always completely symmetric (Lagrange et al. 2013) and, therefore the uncertainty calculated using Eq. 2.1 is underestimated. Thus, following the analysis presented in Elliott et al. (2014), we use an empirical approach to estimate RV uncertainties (see Sect. 2.6.1 for further details).

## 2.4.2 Cross-correlation features

In order to better describe the CCF profile, we calculate a set of high-order cross-correlation features:

*Bisector*: The bisector is calculated from the midpoint of the line for each element of intensity that defines the CCF profile. This is shown by the grey dots in upper right panel in Fig. 2.4.

*Bisector inverse slope*: Here, we adopt the bisector inverse slope (BIS) as defined by Queloz et al. (2001):

$$BIS = \bar{v}_t - \bar{v}_b, \quad (2.2)$$

where  $\bar{v}_t$  is the mean bisector velocity in the region between 10% and 40% of the line depth and  $\bar{v}_b$  is the mean bisector velocity between 55% and 90% of the line depth. These two regions are highlighted in the bottom right panel of Fig. 2.4.

*Bisector slope ( $b_b$ )*: This is defined as the inverse slope from a linear fit for the region between 25%-80% of the CCF's depth (Dall et al. 2006). This is shown by the red line in the bottom right panel of Fig. 2.4.

*Curvature ( $c_b$ )*: The curvature of the CCF's profile is defined as:

$$c_b = (v_3 - v_2) - (v_2 - v_1) \quad (2.3)$$

where  $v_1$ ,  $v_2$ , and  $v_3$  are the mean bisector velocity on the 20-30%, 40-55%, and 75-100% of the CCF's depth. This definition is from Dall et al. (2006) which is a slightly modified version of the curvature presented in Povich et al. (2001).

*Anderson-Darling statistic (AD)*: We use the AD statistic around the peak of the CCF profile as a test for normality, that is, how Gaussian-like the profile is. We perform this test around the  $1\sigma$  region around the peak of the CCF profile. The AD statistic and its

significance are shown in the upper left panel of Fig. 2.4, that is, the null hypothesis that the function is not Gaussian cannot be rejected at a significant level.

*Profile residual:* The CCF profile is fitted by a set of rotational profiles (Gray 1976) to determine its  $v \sin i$  value. In order to quantify the validity of this fit we calculated the overall residual for each  $v \sin i$  profile (from 1 - 200 km s<sup>-1</sup>). The minimum of this set of residuals is used to determine the best-fit profile for each observation, but also the absolute value is retained. That way, we can compare the absolute residuals as a function of other properties in our sample.

## 2.5 Estimates of radial and rotational velocities

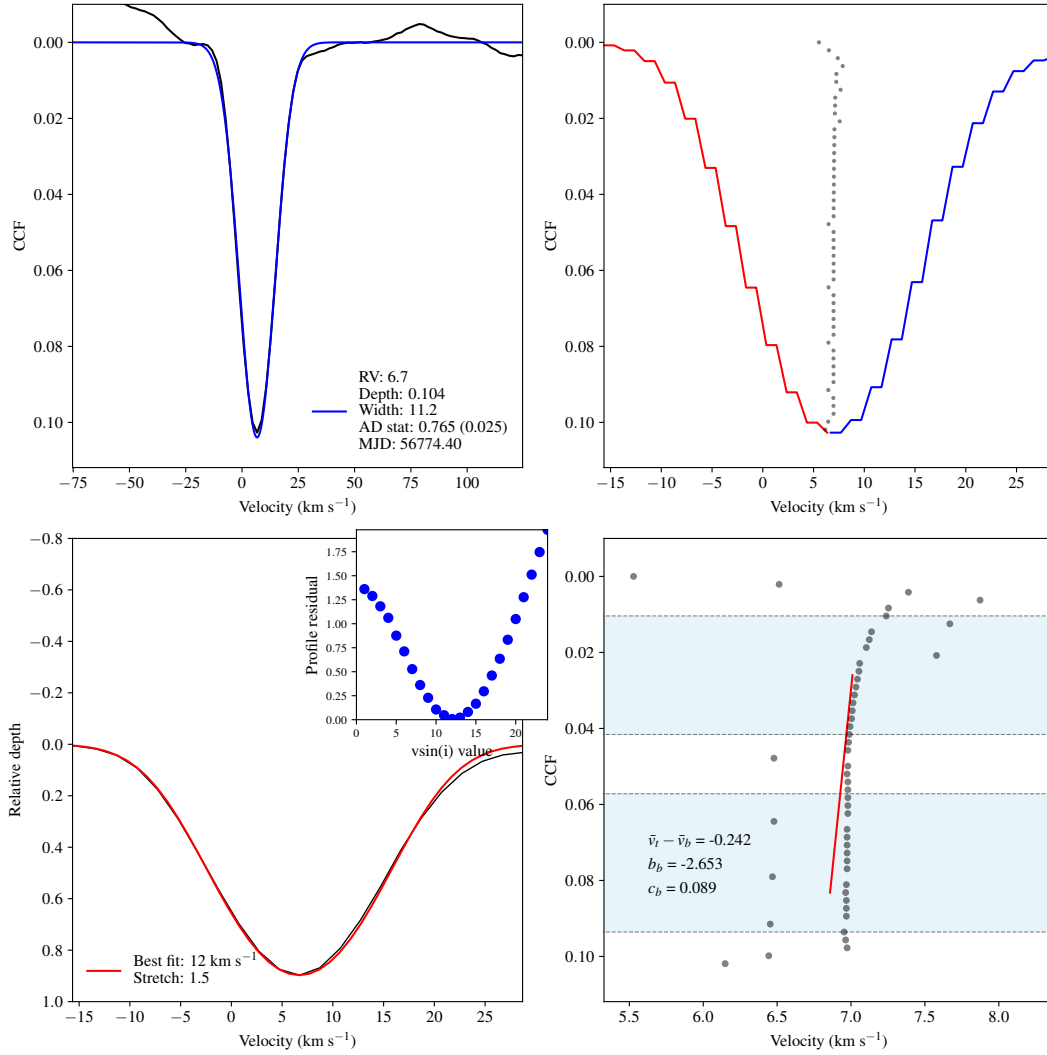
To calculate all the properties defined in the previous section from the available high-resolution optical spectra, we wrote a series of functions<sup>6</sup>. Those functions compute the CCFs and return these properties as a ‘digest’ of the information contained in the CCFs.

Figure 2.4 shows the summary graphical output from the master function described before. The CCF is shown in the top left panel of Fig. 2.4, that is, the resulting profile of the star’s spectrum with the numerical mask (in black) and the Gaussian profile fitted to the data (in blue). The grey dots in the right panel of Fig. 2.4 represent the bisector of the profile whereas the red and blue parts show the two separate sides of the  $2\sigma$  region of the star’s CCF profile. Another relevant output from our functions is the star’s normalised CCF profile with the best-fit rotational profile (bottom left in Fig. 2.4 from a series of profiles with  $v \sin i$  from 1 - 200 km s<sup>-1</sup>). The legend shows the best fitting profile value and the stretch factor, which is a measure of how much the best-fit  $v \sin i$  profile was stretched to achieve the fit. The inset in the upper right shows an area around the minimum of the residuals from different  $v \sin i$  profile fitting, highlighting in this case that 7 km s<sup>-1</sup> is clearly the best fit. We note that these  $v \sin i$  values are ‘raw’, see Appendix 2.11.3 for details on calibration. The three metrics of the bisector are also given by our functions (see bottom right panel in Fig. 2.4); namely the BIS ( $\bar{v}_t - \bar{v}_b$ ), the slope ( $b_b$ ), and the curvature ( $c_b$ ) which help to quantitatively characterise the properties of the bisector.

We visually inspected each of the CCF outputs and removed any observations where the CCF calculation had clearly failed (or a different mask had to be used),

<sup>6</sup>Code is available at <https://github.com/szunigaf>

## 2.5. ESTIMATES OF RADIAL AND ROTATIONAL VELOCITIES



**Figure 2.4:** Example of the graphical output from our CCF calculation code for one target. *Top left:* CCF profile. The quantities shown in the lower left are the peak of the fitted Gaussian profile (RV), the depth of the CCF, the width ( $\sigma$ ) of the Gaussian profile, the Anderson-Darling statistic for normality between  $-\sigma$  and  $+\sigma$  with its respective significance level, and the MJD of the observation. *Top right:*  $2\sigma$  region of the CCF profile and the bisector (grey dots). *Bottom left:* Normalised CCF-fitted with the best-fit rotational profile (from profiles in the  $v \sin i$  range 1–200  $\text{km s}^{-1}$ ). The residuals of fits are shown in the inset. *Bottom right:* Bisector slope along with three metrics of its shape ( $b_b$ ,  $c_b$  and  $BIS$ ). See text in Sects. 2.4 and 2.5 for further details.

mostly due to low S/N. This left 1375 CCFs for further analysis. Several broadening mechanisms can contribute to the width of the CCF – these can either be inherent to the star (surface gravity, effective temperature, rotation, turbulence) or arise from

the instrument used to obtain the observations. Therefore to accurately measure rotational velocities we have to account for non-rotational broadening mechanisms, both physical and instrumental. The details for our calibration approach can be found in Appendix 2.11.3.

With our calibrated  $v \sin i$  values and barycentric RVs, we were able to look at the overall properties of our targets by combining individual observations. We were also able to identify any clear double-lined spectroscopic binaries from their double-peaked CCF profiles (see Appendix 2.11.2).

### 2.5.1 Cross-match with literature

For each object, we compared the median RVs and  $v \sin i$  from our database with previously published values (see Table 2.1 for references) to ensure there was no significant offset. Figure 2.5 shows the results of this comparison. The error bars for each quantity represent the standard deviation from multiple observations.

Black crosses represent objects previously identified as multiple systems, that is, those not likely to follow the 1:1 relation. We also note that for  $v \sin i \gtrsim 50 \text{ km s}^{-1}$ , the broader CCF profile translates into a larger uncertainty on the estimate of this quantity (see Appendix 2.11.3). With all of this taken into account, the 1:1 relation describes adequately the comparison of both sets of values for objects considered as a single stars, demonstrating that our new functions calculating CCF properties are working correctly.

## 2.6 Using multiple measurements to identify single-lined spectroscopic binaries

Most previous studies identifying SB1 solely rely on the analysis of multi-epoch RV values. However, in this work, we use the high-order CCF features, if possible, when investigating any potential RV variation to better conclude on the true nature of the object. We made an initial list of systems to be further investigated by looking at both RV and  $v \sin i$  variation as a function of  $v \sin i$ .

## 2.6. USING MULTIPLE MEASUREMENTS TO IDENTIFY SINGLE-LINED SPECTROSCOPIC BINARIES

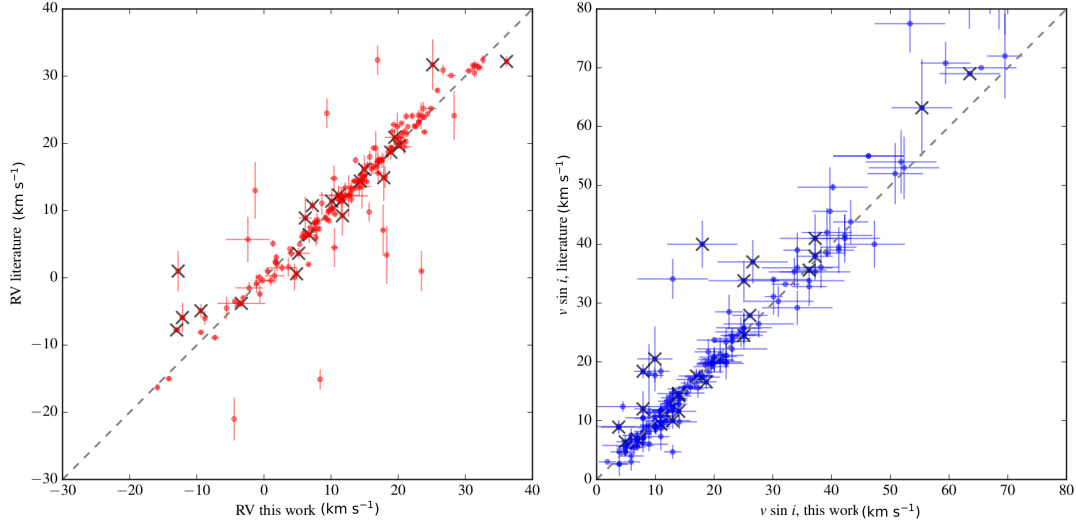


**Figure 2.5:** *Left panel:* RV values calculated in this work versus the values from the literature. Crosses represent previously identified spectroscopic multiple systems. The 1:1 relation is shown by the dashed line. *Right panel:* Same as upper panel, but for  $v \sin i$  values.

### 2.6.1 Distinguishing RV variation as a function of rotation

Typically, the variation in RV ( $\sigma_{\text{RV}}$ ) is used to flag potential SB1. However, this apparent variation can also be caused by mechanisms unrelated to multiplicity. Elliott et al. (2014) used a single value (global  $\sigma_{\text{RV}} = 2.7 \text{ km s}^{-1}$ ) to flag potential SB1, irrespective of their  $v \sin i$  values. However, in this work we show that  $\sigma_{\text{RV}}$  is a function of  $v \sin i$ , that is, the apparent radial velocity variation is intrinsically related to the target's  $v \sin i$ . This was also demonstrated in Bailey et al. (2012) using near-infrared radial velocities. The relationship can be explained by the peak of the CCF being less well-defined the broader the profile is. We can exploit this relationship to revisit the spectroscopic multiplicity of stars in our sample.

Figure 2.6 shows  $\sigma_{\text{RV}}$  versus  $v \sin i$  for stars in our sample that are not double- or triple-lined spectroscopic binaries, and that have observations for at least two different epochs. The left panel shows the estimates from this work while the right panel presents our values together with those compiled from literature and Gaia DR2. For the sake of homogeneity, to be considered, the literature data also has to fulfill the criteria of having an uncertainty on RV and  $v \sin i$  lower than 3 and 5  $\text{km s}^{-1}$ , respectively (Sect. 2.2).

Considering only our measurements, we note that the dispersion in RV is rela-

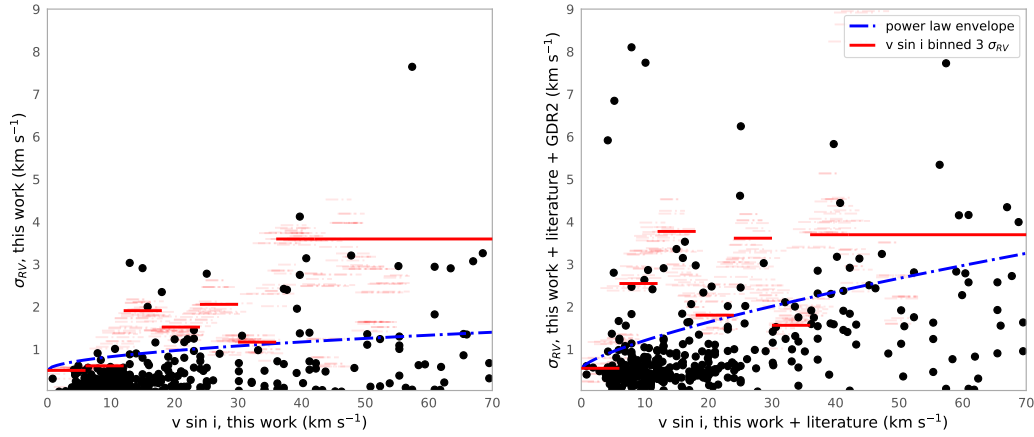


**Figure 2.6:** *Left panel:* Standard deviation in RV as a function of  $v \sin i$  for measurements calculated in this work. The  $3\sigma$  value from binning in  $6 \text{ km s}^{-1}$  bins are represented by the red solid lines. The power-law envelope is represented by dash-dotted blue line. *Right panel:* Same as left panel, but including values from the literature and Gaia DR2 for the standard deviation estimates.

tively low for slow rotators. For example,  $3\sigma$  variation of  $0.7$  and  $1.1 \text{ km s}^{-1}$  for  $v \sin i$  of  $\approx 5$  and  $10 \text{ km s}^{-1}$ , respectively (shown by the solid red line in Fig. 2.6). Only at  $v \sin i \approx 40 \text{ km s}^{-1}$  more than  $3 \text{ km s}^{-1}$  RV variations are observed. When measurements from the literature are considered, on average, RV variations increase which is expected from combining observations from different instruments, heterogeneity in the procedure to perform the estimates, and a longer time-span between observations.

As mentioned before, a relationship between  $v \sin i$  and  $\sigma_{RV}$  is expected. In order to obtain a general and empirical description this relation, we calculated the  $3\sigma$  interval for  $\sigma_{RV}$  using an array of binned  $v \sin i$  values. We ran a Monte Carlo simulation using the  $3\sigma$  statistics for different bin size and phase (the starting point of the binning). The bin size range was between  $3$  and  $7 \text{ km s}^{-1}$ . This range was estimated from the three most commonly used bin-size estimation method: Freedman & Diaconis (1981), Scott (1979) and Sturges (1926). The selected initial phase range covers from  $0$  to  $4 \text{ km s}^{-1}$ . This exercise allowed us to address the dispersion in the results that can be explained solely in terms of the choice of phase and bin size. Each realization is represented by a light red line in Fig. 2.6. It is out of the scope of this work to characterize, in detail, the underlying physical structure between the  $\sigma_{RV}$  values as a function of  $v \sin i$ . The only purpose of the simple analysis presented here is to have a first order estimate of the effect of the rotation velocity in the RV determination and, consequently,

## 2.6. USING MULTIPLE MEASUREMENTS TO IDENTIFY SINGLE-LINED SPECTROSCOPIC BINARIES

in its variation. The final adopted thresholds to be used as ‘caution’ flags when assessing multiplicity are those resulting from a  $6 \text{ km s}^{-1}$  step between 0 and  $42 \text{ km s}^{-1}$  (solid red line, Fig. 2.6). This bin size was selected by taking in consideration the better compromise between sampling and the minimum number of points in each bin. Beyond  $43 \text{ km s}^{-1}$  on  $v \sin i$ , the number of points in each bin is  $\lesssim 10$  and, therefore, the statistics become less reliable. However, we can assume that a very rough positive correlation is maintained or, at the very least, that it does not invert, that is, the higher the  $v \sin i$ , the larger the RV variation is.

As an alternative method to identify SB candidates, we fit a power-law of the form  $\sigma_{\text{RV}} = m (v \sin i)^b$  and then we scale it up to keep a conservative envelope that leave about 85% of the points below it. The fit is obtained using a Huber loss function (Huber 1964), which is more robust to outliers than squared loss function (Ivezić et al. 2014) and is shown as a dashed-dotted blue line in Fig. 2.6. We identified SB candidates using both selection criteria and further investigated the nature of any targets with RV variation lying above either of those thresholds. We investigated the true SB nature of any targets with RV variations above those thresholds (see Table 2.3 and Appendix 2.11.2).

### 2.6.2 Distinguishing fast rotators from blended binaries

Large projected rotational velocity values could not only result from a single fast rotator, but also from a blended profile of two slower rotators. If the latter is the case, one would expect  $v \sin i$  values varying in time depending on the system’s phase at the time of the observations. To investigate any potential systems of this kind, similarly to Fig. 2.6, we looked at the typical variations in  $v \sin i$  as a function of median  $v \sin i$ . These results are shown in Fig. 2.7. We note that as our  $v \sin i$  values are calculated from a grid of rotational profiles with  $1 \text{ km s}^{-1}$  step, our study is not sensitive to smaller variations and, therefore, many objects appear to be constant. Following a similar approach to the one of the previous subsection, we calculated an upper envelopes to the variations in  $v \sin i$  and flagged systems above those levels for further inspection.

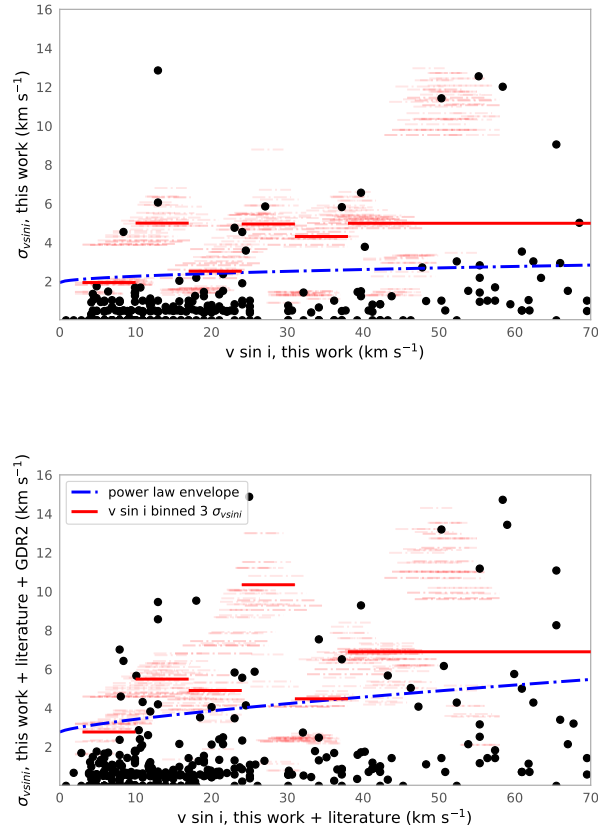


**Figure 2.7:** *Top panel:*  $v \sin i$  versus the standard deviation in  $v \sin i$  for measurements calculated in this work. The  $3\sigma$  values, from 3 to 45 km s<sup>-1</sup> binned in 7 km s<sup>-1</sup> bins, are shown by red solid lines. The power-law envelope is represented by dash-dotted blue line. *Bottom panel:* Same as upper panel, however, including values from the literature.

### 2.6.3 Using the BIS versus RV relation

Another way to validate whether a RV variation is induced by a bound companion is to include the BIS as an additional source of information. Lagrange et al. (2013) used this technique searching for giant planets in a sample of 26 stars, some of which are in the young associations studied here. Significant anti-correlation between the BIS and RV suggests that the RV jitter is most likely due to stellar activity (Desort et al. 2007). This technique relies on a large number of measurements per target and therefore in this work we are limited to a small number of stars in our sample. Therefore, in our case, this technique allowed us to rule out a few potential SBs rather than to identify new systems. The BIS and RV values are listed in Table 2.4.

## 2.6. USING MULTIPLE MEASUREMENTS TO IDENTIFY SINGLE-LINED SPECTROSCOPIC BINARIES

**Table 2.2:** Properties of previously identified close visual binaries within our sample.

ID	$\sigma_{RV}$ (km s <sup>-1</sup> )	$v \sin i$ (km s <sup>-1</sup> )	Time span (day)	Num. obs	P (year)	Ref.
TWA 22	0.19	9.9	64	3	5.15	a
HD 98800	0.07	< 5	4	2	0.86	b, g
HD 16760	...	< 5	...	1	1.27	c, d
HD 36705	...	$\approx 75$	...	1	11.74	e, f

**Notes.** a: Bonnefoy et al. (2009), b: Malkov et al. (2012), c: Bouchy, F. et al. (2009), d: Sato et al. (2009), e: Close et al. (2005), f: Nielsen et al. (2005), g: Torres et al. (1995)

### 2.6.4 Spectroscopic binaries from the literature

We searched the literature to identify formerly flagged SBs from our sample to assess the robustness of our method. For all previously identified spectroscopic binaries, we recover a very large fraction of them (84% $^{+11}_{-8}$ ). Most of the non-recovered SBs correspond to objects or systems with very few observations in our local database, but for a few of the objects, our analysis contradicts the ‘SB flag’ found in the literature (see Appendix 2.11.2 for comments on the individual sources).

### 2.6.5 Close visual binaries from the literature

Some multiple systems have the right configuration and are located at the right distance for them to be resolvable with direct imaging techniques (with adaptive optics, AO hereafter) and, in addition, display RV variations of the primary. A good example of such system is V343 Nor (Nielsen et al. 2016). Looking for similar cases, we compiled a list of targets from the literature that have AO-discovered known companions (typically, with estimated periods of  $\approx 1000$  days, Table 2.2).

Unfortunately, within this AO sample of four close visual binaries, none of them had sufficient time coverage in our database of high-resolution spectra to achieve the sensitivity needed to detect any companion-induced RV changes. However, the orbits of all four systems have been determined in previous works, as noted in Table 2.2.

## 2.6.6 Detection of SBs candidates

The final list of SB candidates identified in this work is presented in Table 2.3. In a few cases, our analysis contradicts previous claims of multiplicity from the literature, while in some other cases, we do not recover the SB nature of some candidates, which we attribute to the sampling of the data available to us (see details on Appendix 2.11.2).

Out of the 381 objects from the compilation of our work, the literature (Table 2.1) and Gaia DR2, we identified 68 SB candidates. For each candidate, we compiled all the information available regarding RV and  $v \sin i$  both from our work and the literature. We used those values to establish a final classification regarding their multiplicity. The conclusion (*Conc.*) column of Table 2.3 presents the summary of this analysis, where the values ‘Y’, ‘N’, or ‘?’ correspond to ‘multiple system’, ‘not a multiple system according to the data available’, or ‘inconclusive’.

While specific comments for particularly interesting or challenging candidates can be found in Appendix 2.11.2, there were a number of cases where the variable flag of  $v \sin i$  turned out to be a misleading diagnostic. In these cases, a closer inspection of the CCF profiles revealed that the variability was not real and, rather, simply induced by a poor fitting of the rotational profile. In such cases, it is still possible that the candidate is an unresolved SB, but since we do not have sufficient evidence to support that conclusion, we flagged those candidates as inconclusive.

## 2.7 Accounting for observation sensitivity

As we have seen through this work, tight binaries can be detected in spectroscopic data via identification of double (or multiple) lines, variable RVs (or, unrelated to this work, even unexpected mixes of spectroscopic features). However, our ability to identify these features (multiple lines and variations in RV), can be severely biased by factors such as: the observations strategy (time span  $T$  and number of measurements  $N_{\text{obs}}$ ) and the inherent sensitivity of the spectrographs employed for the observations. These factors have been thoroughly studied and modelled by Tokovinin (2014a). The steps incorporated in our analysis to translate this knowledge into detection probability maps were the following:

Firstly, we created a set of 10,000 simulated binaries from the following distribu-

## 2.7. ACCOUNTING FOR OBSERVATION SENSITIVITY

tions:

Period ( $p$ ) log-normal ( $\mu=5.03$ ,  $\sigma=2.28 \log(\text{day})$ , Raghavan et al. 2010). Mass ratio ( $q$ ) uniform (for system between  $0.01-1.0 M_{\odot}$ ; Raghavan et al. 2010; Kraus et al. 2011; Elliott et al. 2015). Eccentricity ( $e$ ), two-part:  $p \leq 12$  days,  $e=0$ ;  $p > 12$  days, uniform (for  $0 \leq e \leq 0.6$ ). Initial phase ( $\phi_0$ ), longitude of ascending mode ( $\omega$ ) and inclination ( $i$ ) uniform (for  $0 \leq \phi_0 \leq 1$ ,  $0 \leq \omega \leq 2\pi$ , and  $0 \leq i \leq \pi$ , respectively).

From our simulations and using Eqs. 5 to 7 from Tokovinin (2014a), we calculated a detection probability map for each object characterised by its three detection parameters ( $N_{\text{obs}}$ ,  $T$  and  $\sigma_{RV}$ ). In the case of single epoch data, we assumed the same artificial parameters used by Tokovinin (2014a) (i.e.  $T = 100$  days,  $N_{\text{obs}} = 3$ , and  $\sigma_{RV} = 2 \text{ km s}^{-1}$ ), since we are still sensitive to double- and triple-lined multiple systems.

The detection map of each object was calculated on the same mass ratio versus period grid. This ‘common-grid’ approach makes it easy to average those maps for objects belonging to the same moving group, yielding an average sensitivity map per association in our sample (see Fig. 2.8).

These ‘association-averaged’ probability maps were used to correct our SB fractions from biases induced by the observation strategy and precision. The correction was calculated by taking the mean value in the parameter space  $0.1 \leq q \leq 1$  and  $p \leq 10^{3.2}$  days. We excluded mass ratios smaller than 0.1 as very few targets have any meaningful probability of detection in this parameter space (Fig. 2.8, color-scale from red, 100%, to white, 0%).

We note that these corrections are applied across the entire parameter space and do not have assumptions regarding the underlining mass ratio or period distributions (as we have extremely limited information on both).

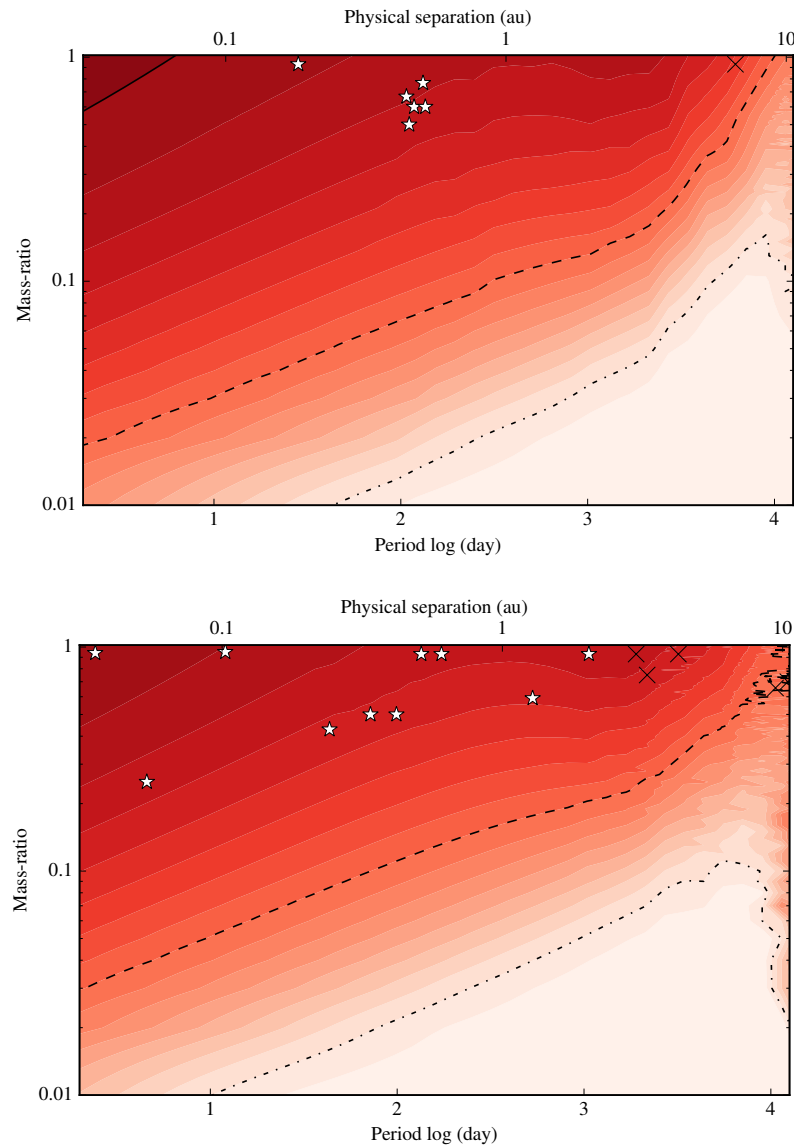


**Figure 2.8:** *Upper panel:* Average detection probabilities for THA association (contours from red, 100%, to white, 0%), detected spectroscopic companions (white stars) and visual binaries (black crosses) in the physical separation versus mass ratio. The solid, dashed and dash-dotted lines encompass areas with detection probabilities  $\geq 90\%$ ,  $50\%$ , and  $10\%$ , respectively. *Bottom panel:* Same as upper panel, but for BPC association.

## 2.8 Updated census of spectroscopic binaries

Building from the previous sections, in Fig. 2.9, we present the SB fraction obtained for each associations as a function of the median  $v \sin i$  of its members. In that figure we present both fractions: the original one that disregards the effects discussed in Sect. 2.7, and the ‘corrected’ one (blue and red symbols, respectively). The uncertainties on the derived fractions are calculated from binomial statistics (Burgasser et al. 2003).

As mentioned earlier in this paper, it is extremely difficult to fully account for the effect of  $v \sin i$  on the sensitivity in order to identify SBs. Since fast rotators may bias the resulting SB fractions, we opted to look for any relationship between the obtained SB and the median  $v \sin i$  of the members of each association. No apparent correlation was found between those two quantities, and the distribution of  $v \sin i$  values for each association are plotted in Fig. 2.10.

One striking result from our study is that the SB fraction obtained for the TW Hya association seems to contradict the results from Elliott et al. (2014). This difference is driven by the discovery of three newly identified SBs in this work, which was possible because of an increase of 30% in the amount of data available for this association since Elliott et al. (2014). To test this result against membership criteria, we compared the fraction estimated using the census obtained from the BANYAN  $\Sigma$  tool with that of the convergence method and found both figures to be fully compatible (see Fig. 2.11).

Interestingly, the three highest SB fractions are found for the three youngest associations ( $\epsilon$  Cha  $18_{-11}^{+15}\%$ , TW Hya  $22_{-14}^{+16}\%$  and  $\beta$  Pictoris moving group  $24_{-8}^{+9}\%$  prior sensitivity correction, and  $22_{-11}^{+15}\%$ ,  $32_{-12}^{+16}\%$ , and  $33_{-8}^{+9}\%$ , respectively, when the corrections of Sect. 2.7 are applied). This is unlikely to result from a lack of sensitivity due to large rotational broadening, as the median  $v \sin i$  values are relatively low and similar (once the low-number statistics are taken into account) for the three associations (see Fig. 2.10). Furthermore, as shown in Fig. 2.11, the higher SB fraction of these associations seems to be insensitive to the membership criteria used, appearing also when the BANYAN  $\Sigma$  census is employed. On the other hand, the average SB fraction for the five older associations are  $\lesssim 10\%$  (with the possible ‘intermediate’ case of THA). It must be noted that the confidence interval for this ‘dichotomy’ is only 1 to 2  $\sigma$  given the large associated uncertainties.

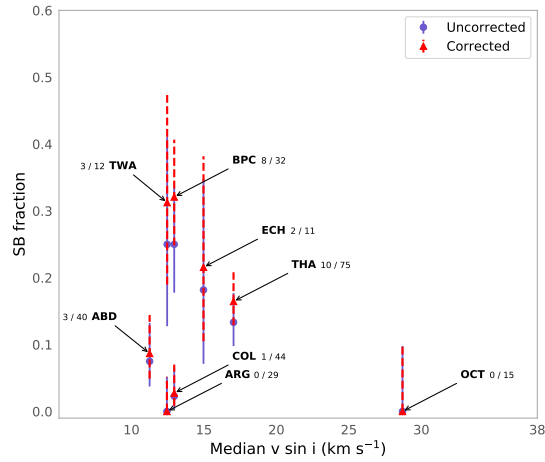


**Figure 2.9:** SB fraction as a function of median  $v \sin i$ . The uncorrected SB fractions are shown in purple and in text next to the name of each association. The corrected SB fractions are shown in red. The primary mass range is  $0.6 \leq M \leq 1.5 M_{\odot}$ .

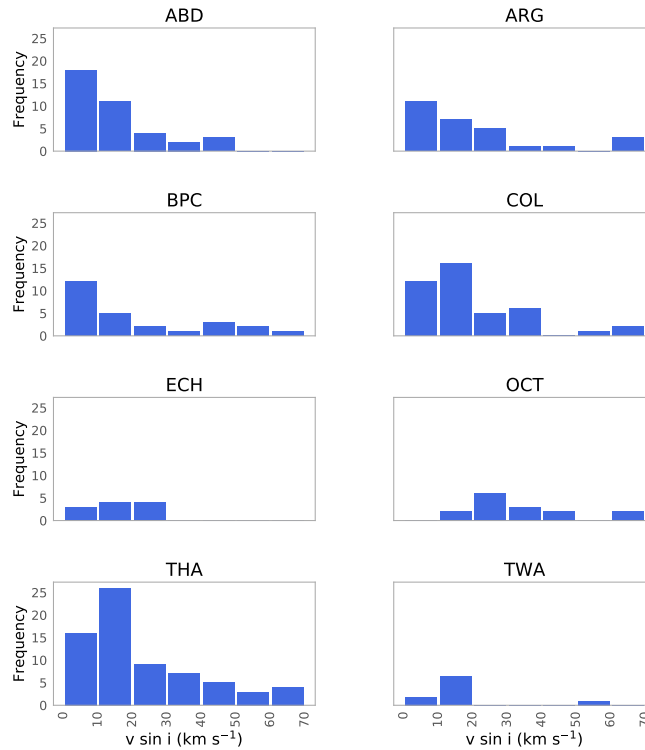


**Figure 2.10:**  $v \sin i$  histogram for each young association from this work with a primary mass range of  $0.6 \leq M \leq 1.5 M_{\odot}$ .

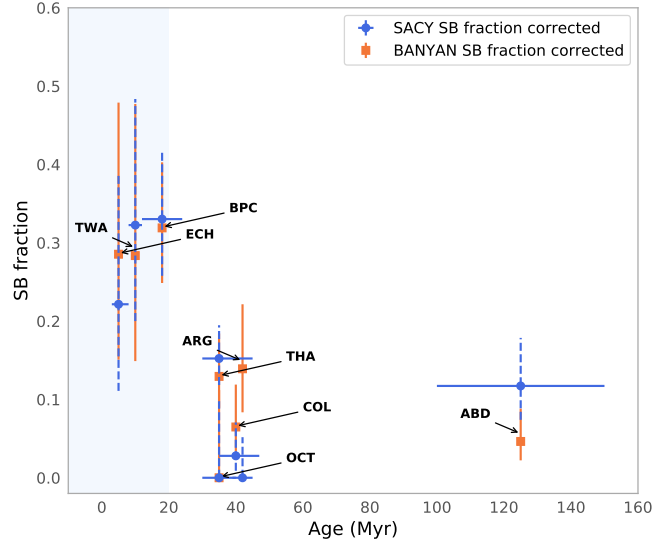


**Figure 2.11:** Corrected SB fraction as a function of age (Myr) for membership estimation from our convergence method (blue dots, Torres et al. 2006; Torres et al. 2008) and BANYAN  $\Sigma$  (orange dots, Gagné et al. 2018a). The shaded area highlights the  $\leq 20$  Myr zone of the figure. The primary mass range is  $0.6 \leq M \leq 1.5 M_{\odot}$ .

## 2.9 Discussion

The results presented in Sect. 2.8 suggest a counter-intuitive path of evolution for SBs. In this section, we compare our results to the literature, discuss whether these results are, in fact, an artifact produced by our methodology or a physical result; and, in the latter case, whether we are really witnessing early SB evolution or the effect of other environmental factors.

### 2.9.1 Comparison with previous results on low density environments

Figure 2.11 shows SB fractions ( $\approx 10\%$ ) consistent with the field population ( $\approx 10\%$ , Raghavan et al. 2010; Tokovinin 2014b), the young clusters Tau-Aur, and Cha I ( $\approx 7\%$ , Nguyen et al. 2012), and our previous results from Elliott et al. (2014) for the five older associations ( $\gtrsim 20$  Myr) across the mass range of  $\sim 0.2 - 2.0 M_{\odot}$ . On the other hand, the observed SB fractions for the three youngest associations seem to be larger than those reported for the previously mentioned young regions of Tau-Aur (1 Myr) and Cha I (2 Myr). The estimated distances to these young regions are  $\sim 140$  pc and

$\sim 160$  pc, respectively (Nguyen et al. 2012); therefore, we argue that, given the overall closer distance of our targets, the difference should not arise from a lack of sensitivity or a completeness bias in the SACY sample (see Sect. 5 from Nguyen et al. 2012).

Nevertheless, the relative paucity of SBs in Tau-Aur and Cha I could be explained by the sample used by Nguyen et al. (2012), which is concentrated on the higher stellar density regions of the clouds. For instance, Guieu et al. (2006) revisited the previously claimed brown dwarf deficit in the same Tau-Aur region, performing a larger scale optical survey including the surroundings of the clouds as well as their densest parts. The authors concluded that the possible deficit was in fact an artefact from target selection rather than a real difference. Interestingly, Viana Almeida et al. (2012) derived an SB fraction of  $\approx 42\%$  for the Rho Ophiuchus star forming region ( $\sim 0.1 - 1$  Myr) from targets with mass range of  $\sim 0.18 - 1.4 M_{\odot}$  (Natta, A. et al. 2006) and a binary fraction of  $\approx 71\%$  combining data from different works. These results are more consistent with the SB fraction of our youngest associations and are aligned with the notion that multiplicity is very high at young ages (younger than  $\sim 1$  Myr). Although the statistical significance in the difference on SB fraction in Fig. 2.11 is weak, at the level of 1 to  $2\sigma$ , it is hard to reconcile with the general picture of SB fraction remaining unchanged after  $\sim 1$  Myr. Therefore, it deserves independent confirmation and further characterisation.

## 2.9.2 The impact of the sensitivity correction

In Sect. 2.7, we created sensitivity maps from 10,000 simulated binaries to estimate how many binary systems would have been missed because of our observing strategy. The simulated binaries were drawn according to certain priors on the mass ratio, period, and orbital parameters, but those parental distributions were originally estimated from field star surveys (Raghavan et al. 2010; Tokovinin 2014a). Those priors may not be representative of the underlying population of binary stars in young associations ( $\lesssim 100$  Myr). This may have consequences on the sensitivity corrections we obtained which may lead to an artificially large value for the corrected SB fraction.

The prior on the period distribution is the most critical one, as it has the most significant effect on the detection probability (shorter periods are easier to detect using spectroscopic observations). Taking this into consideration, we created new sensitivity maps using a log-normal period distribution ( $\mu = 5.3$ ,  $\sigma = 2.28 \log(\text{day})$ ), from

Tobin et al. 2016), representative of Class 0/I systems ( $\lesssim 1$  Myr). With this period distribution, we obtain an increase of  $\sim 2\%$  on the correction factor. This slight increase is not sufficient to explain the difference of  $\gtrsim 10 - 20\%$  between the three younger associations with respect to the older ones in our sample. We further tested the impact of the period distribution on the correction factor by taking an even more extreme case. We used a distribution centred at the smallest separation that a primordial binary system could have ( $\approx 10$  au from disc fragmentation Vaytet, N. et al. 2012). Even in that almost unrealistic scenario, we did not reach a change of sensitivity sufficient to justify the differences of SB fractions between the young and old associations in our sample. The analysis presented here suggests that the differences in SB fractions are not artificially created by our sensitivity correction approach.

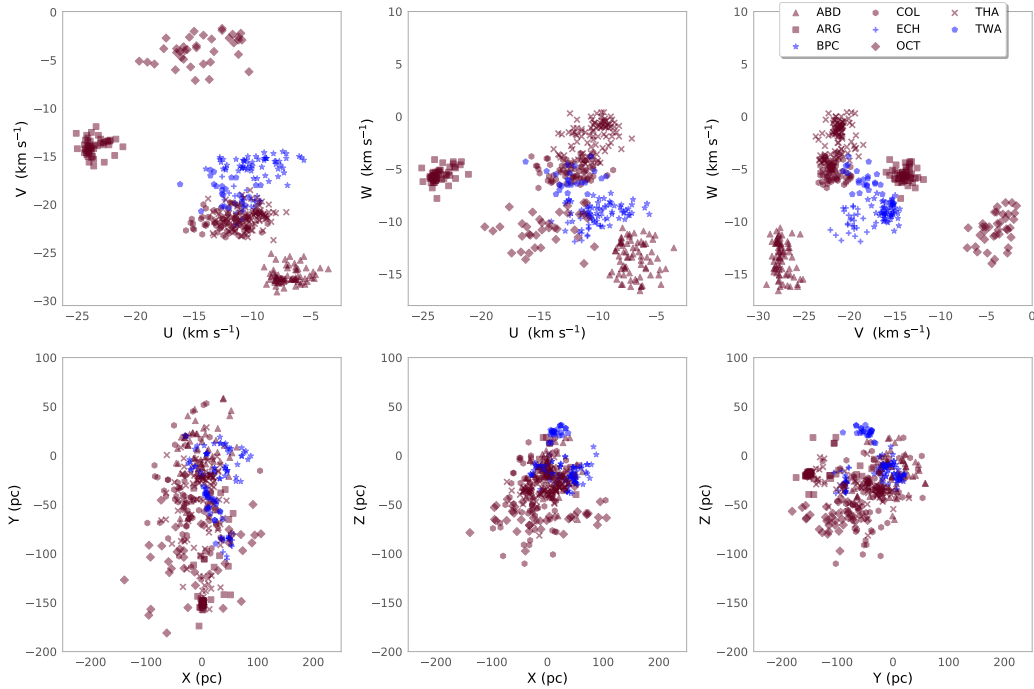


**Figure 2.12:** Combinations of the sub-spaces of the UVWXYZ-space for the young associations in the SACY sample. The blue coloured symbols correspond to the three youngest associations (BPC, ECH and TWA). The full membership study and further analysis will be presented in Torres et al. (in prep.).

### 2.9.3 Relation with higher-order multiplicity

From the SBs identified in this work,  $\sim 77_{-7}^{+8}\%$  are also part of higher-order multiple systems (Elliott et al. 2016a; Elliott & Bayo 2016). This shows a preference for SBs to be found in triple or higher-order systems, similar to the 63% reported in Tokovinin et al. (2006) for field stars.

There is observational evidence that suggests an overall decrease of binary fraction from pre-MS ages to field ages (Ghez et al. 1997; Kouwenhoven et al. 2007; Raghavan et al. 2010). Elliott & Bayo (2016) suggested that dynamical interactions of triple systems (as proposed by Sterzik & Tokovinin 2002; Reipurth & Mikkola 2012) could explain the population from close (0.1 au) to very wide (10 kau) tertiary components where the majority of the wide companions are in the process of being disrupted on timescales of 10 – 100 Myr. The results of Raghavan et al. (2010) also suggest that systems with long periods, or those with more than two components, tend to lose companions with age due to dynamical evolution. However, such mechanisms, which would explain the disruption of wide companions but would not necessary explain the SB fraction in this sample. In fact, Tokovinin et al. (2006) suggested that the overall SB fraction seems to remain unchanged after  $\sim 1$  Myr.

Supporting the dissolution scenario, proposed by Sterzik & Tokovinin (2002); Reipurth & Mikkola (2012),  $\sim 92_{-6}^{+13}\%$  of SBs in the three youngest associations studied here are part of a triple or high-order multiple system that stand in contrast with the  $\sim 67_{-11}^{+12}\%$  for the five older associations.

### 2.9.4 SB fraction evolution with age

Our results hint that the youngest associations ( $\lesssim 20$  Myr) may have a larger SB fraction, even though it remains tentative at the moment. This result suggests a possible decrease of the SB fraction from  $\sim 5$  to  $\sim 100$  Myr. A similar result was obtained for the IN-SYNC (INfrared Spectroscopy of Young Nebulous Clusters) sample from high resolution H-band spectra observations of low-mass stars in Orion A, NGC 2264, NGC 1333, IC 348, and the Pleiades (Jaehnig et al. 2017), where the SB fraction of the five pre-MS clusters ( $\approx 1 - 10$  Myr) was  $\approx 20\% - 30\%$  in contrast with  $\approx 5\% - 10\%$  found for the Pleiades ( $\approx 100$  Myr). Jaehnig et al. (2017) claim that the time sampling of their observations make it more sensitive to the critical  $10^2 - 10^4$  day period range where binary systems are wide enough to be disrupted by dynamical interaction over  $\sim 100$

Myr timescale in dense environments. However, this scenario is proposed for clusters with typical densities of  $\approx 30M_{\odot} \text{pc}^{-3}$  (at the core radius, Piskunov et al. 2007) and may not be compatible with the typical densities of  $\approx 0.01 \text{ stars pc}^{-3}$  for loose associations such as those in the SACY sample (Moraux 2016).

### 2.9.5 Role of the environment

The tentative variations in SB fraction could be related to differences in the primordial multiplicity depending on the formation history and environment of the associations. In Fig. 2.12, we show the sub-spaces of the UVWXYZ-space for all the associations studied in this paper to search for possible signs of clustering in both velocity and spatial coordinates. Given the proximity of the SACY associations no clear separated groups of points appear for the spatial coordinates (Torres et al. 2006). However, it is more informative to plot the galactic proper motion to trace a possible common origin (UVW: positive toward the Galactic center, Galactic rotation, and North Galactic Pole respectively). Qualitatively, we identify possible clustering of points in the UVW sub-spaces (first row of Fig. 2.12) for the three youngest associations (blue coloured symbols) that may suggest possible common birth place in the Galactic bars for these associations compared to the older ones.

Furthermore, previous studies have found evidence that the three associations,  $\beta$  Pictoris, TW Hya, and  $\epsilon$  Cha possibly formed in or near the Sco-Cen giant molecular cloud 5 – 15 Myr ago (Mamajek & Feigelson 2001; Torres et al. 2008). Then the difference in the SB fraction presented in this work could arise from different primordial multiplicity instead of being caused by their dynamical evolution. Standing in support of the latter argument, the overall binary fraction in Sco-Cen is  $\approx 93\%$  among solar-type stars and  $\approx 75\%$  among low-mass star (Kouwenhoven 2006). These figures are higher than the overall binary fraction for solar-type and low-mass stars in Tau-Aur reported by (Kraus et al. 2011,  $\sim 66 - 75\%$ , with slightly different binary parameter space explored). In addition, Clark Cunningham et al. (2020) recently claimed that the ABD association may be kinematically linked to a newly discovered ‘stellar string’ Theia 301. Kounkel & Covey (2019) argue that although they recover Sco-Cen in their kinematic clustering searches, this association is different than the ‘typical strings’ such as Theia 301. To summarise, there are hints supporting non-universal multiplicity, however, our current data-set does not allow us to confirm different en-

vironmental star-formation histories among the SACY associations.

## 2.10 Summary and conclusions

In this work, we present an update for the SB census for the associations within SACY. Our study is based on new observational data (as well as literature and archival data), as well as new criteria to identify these tight binaries. We have estimated radial and rotational velocity for 1375 spectra using CCFs and compiled  $\sim 400$  RV measurements from the literature (including Gaia DR2, Gaia Collaboration et al. 2018). Our RVs and  $v \sin i$  estimates are in good agreement with previously published values, following a 1:1 relation with values from the literature (for targets that are not identified as a multiple systems), demonstrating that our CCF analysis is robust. Further robustness is provided by the fact that we have recovered the  $84^{+11}_{-8}\%$  of previously known multiple systems.

Besides RV variations proving to be key in identifying SB candidates, we used high-order cross-correlation functions as a complementary diagnostic tool. These features offer a concrete way to quantify the symmetry, curvature, and quality of the fitting of the CCFs. More epochs do not only allow us to improve the reliability of any RV variation, but it also allows for other statistics to be used when assessing the binary nature of a candidate (see Sect. 2.6.3, for instance).

We calculated the SB fraction for each SACY association and estimated a correction factor taking into account possible sensitivity issues and biases from the observations (see Sect. 2.7). The summary of SB candidates can be found in Tables 2.3 and 2.7. The analysis and conclusions reached for each target flagged as a candidate can be found in Appendix 2.11.2.

We find that the three youngest associations have higher SB fractions overall ( $\epsilon$  Cha  $22^{+15}_{-11}\%$ , TW Hya  $32^{+16}_{-12}\%$  and  $\beta$  Pictoris moving group  $33^{+9}_{-8}\%$  when the corrections of Sect. 2.7 are applied) compared with the five oldest associations in the SACY sample ( $\sim 35 - 125$  Myr), which are  $\sim 10\%$  or lower. This results seems to be independent of the method used for membership assessment (see Fig. 2.11) and not artificially created by the sensitivity correction approach (see Sect. 2.9.2). In addition, more than 90% of the SB identified in  $\epsilon$  Cha, TW Hya and  $\beta$  Pictoris are part of a triple or hierarchical system in contrast with  $\approx 70\%$  of the five older associations. While the difference in the SB fraction remains tentative at the moment, we propose two possible explanations:

an evolution effect (previously reported in denser environments) and a primordial non-universal multiplicity. With the data currently available, we cannot distinguish between the two possibilities.

## 2.11 Appendix

### 2.11.1 Targets flagged as potential SB1

Table 2.3: Properties of targets flagged as potential SB1 systems in the analysis presented in this work. Standard deviation are calculated for targets with two or more epochs. Targets previously flagged but not recovered in this work are available in Appendix 2.11.2. The new and recovered SB2 and SB3 targets are available in Appendix 2.11.2 and Table 2.7.

ID	Values calculated in this work				Values calculated in this work + literature				# obs	Flag	Conc.
	RV <sub>median</sub>	$\sigma_{RV}$	vsini <sub>median</sub>	$\sigma_{vsini}$	RV <sub>median</sub>	$\sigma_{RV}$	vsini <sub>median</sub>	$\sigma_{vsini}$			
Potential SB1 systems from variable RV and/or $v \sin i$ values											
CD-46 644	23.70	0.03	34.16	0.0	24.22	0.96	34.16	7.54	2 (4)		N
HD 17332 A	4.62	0.75	8.41	4.55	4.20	0.66	8.41	4.55	2 (4)		?
CD-56 1032A	31.87	4.12	39.72	6.56	31.87	5.83	39.72	9.28	2 (2)		Y
CPD-19 878	25.59	1.32	30.63	0.51	25.59	1.32	30.63	0.51	4 (4)		?
TYC 7627-2190-1	21.94	3.03	12.95	12.85	21.94	3.71	24.98	14.88	3 (4)		Y
V*PXXVir	-12.99	0.52	4.17	0.31	-12.39	5.81	4.16	0.35	4 (8)	SB1	Y
HD 159911	21.77	0.63	58.4	12.02	21.77	0.63	58.4	12.02	3 (3)		Y
CD-43 3604	17.5	2.35	18.0	2.19	17.43	2.66	18.0	9.52	4 (5)		Y
V* V379 Vel	14.645	0.045	7.9	1.5	14.6	1.49	7.9	1.5	2 (3)		?
TYC 8594-58-1	11.03	0.650	12.95	0.0	11.03	0.75	12.95	9.45	4 (5)		N
2MASS J12203437-7539286	4.86	0.02	7.9	1.5	4.86	2.47	7.90	2.37	2 (3)		Y
HD 129496	-6.07	3.07	66.99	1.51	-6.07	3.07	66.99	1.51	2 (2)		N
V*AFLeP	20.89	1.11	50.32	11.42	21.39	1.25	50.32	11.42	4 (5)		N
HD 139084	5.17	1.99	15.77	0.56	5.10	1.76	15.88	0.55	9 (11)	SB1	Y
HD 139084 B	4.55	0.01	15.98	1.50	2.32	3.14	15.98	1.5	1 (2)		N
HD 164249 A	-0.14	1.17	21.54	2.37	-0.09	1.06	21.03	2.25	8 (11)		N
HD 164249 B	-0.6	0.28	12.95	6.06	-0.88	0.88	12.95	6.06	2 (3)		N
CD-31 16041	-8.81	0.20	40.22	3.78	-8.73	1.25	43.25	4.92	3 (4)		N
V*PZTel	-2.99	2.96	55.23	12.55	-3.54	2.71	58.99	12.81	10 (12)		N
HD 199143	-22.73	...	58.40	...	-13.62	12.89	92.95	48.86	1 (2)		N
*cEri	18.48	7.64	57.39	1.69	18.43	7.23	57.39	1.69	7 (8)		N
GJ 3305	23.91	0.49	5.88	0.48	20.95	1.57	5.88	0.48	3 (9)		Y
HD 22213	11.27	3.14	40.73	0.51	11.27	3.14	40.73	0.51	2 (2)		Y
HD 21997	17.17	0.86	65.47	9.05	17.24	0.91	65.47	9.05	3 (4)		N
V*AGLeP	25.31	0.57	23.050	4.76	25.31	0.57	23.050	4.76	4 (5)		?
CD-44 753	13.16	0.91	7.9	0.95	13.78	1.37	7.0	0.95	3 (6)		N
HD 104467	11.16	2.78	25.07	2.25	11.4	2.31	25.07	2.25	6 (8)		Y
2MASS J12020369-7853012	11.17	2.91	14.97	0.71	11.17	2.91	14.97	0.71	4 (4)	SB1	Y
BD-184452A	...	...	...	...	-19.31	2.01	8.05	4.59	0 (2)		?
GSC 08057-00342	...	...	...	...	13.5	5.59	5.2	...	0 (3)	SB1	Y
2MASS J04470041-513440	...	...	...	...	17.92	1.98	5.1	...	0 (2)		N
UCAC3 33-129092	...	...	...	...	7.07	2.86	10.5	...	0 (2)		N
UCAC4 110-129613	...	...	...	...	3.58	6.24	25.1	...	0 (2)		N

## CHAPTER 2. AN UPDATED CENSUS OF SPECTROSCOPIC BINARIES IN SACY

CD-53 544	12.62	2.90	63.45	2.18	12.56	2.55	65.47	8.26	3 (5)		N
TYC8098-414-1	...	...	...	...	19.53	8.72	11.75	9.40	0 (6)		?
HD 207575	1.42	2.42	37.19	5.82	1.5	2.14	37.19	5.82	5 (7)		?
HD 207964	23.46	0.2	53.86	1.52	23.26	12.65	53.86	1.52	2 (3)		N
TYC 9344-293-1	6.16	1.01	55.37	1.43	6.95	1.57	55.35	10.0	3 (6)		N
UCAC3 92-4597	...	...	...	...	-5.2	9.81	4.7	...	0 (3)	SB	Y
HD 3221	-2.39	3.26	68.5	5.01	-2.39	3.26	68.5	5.01	3 (3)		N
UCAC3 70-2386	...	...	...	...	5.65	2.33	19.2	...	0 (2)	SB	Y
V* CE Ant	11.7	0.06	4.87	1.75	12.4	0.32	4.87	1.76	4 (17)		N
TWA23	10.82	0.04	9.92	3.0	7.71	2.61	9.92	3.0	2 (16)	SB	Y
UCAC2 1331888	-1.66	0.56	25.07	1.0	-2.22	2.01	25.80	1.09	2 (3)		N
HD 48189	36.14	0.01	16.99	1.5	33.40	2.06	17.29	0.43	2 (3)		N
CD-30 3394	12.71	2.39	37.69	0.50	14.99	2.84	37.19	0.87	4 (5)		?
CD-30 3394B	13.94	3.21	47.79	2.71	15.09	3.24	47.29	4.07	4 (5)		?
CD-52 9381	-13.85	2.74	39.71	1.23	-13.85	2.74	39.71	1.23	4 (4)		N
GSC 08350-01924	1.57	1.45	23.05	3.0	0.21	1.46	23.05	3.0	2 (4)		N
V* AFHor	12.91	0.06	7.90	1.5	12.70	1.13	7.90	1.58	2 (6)		N
RX J12204-7407	14.60	1.37	39.72	1.5	14.60	1.58	39.71	1.72	4 (4)		N
[FLG2003] eps Cha 7	13.64	1.24	23.05	0.47	13.64	1.24	23.05	0.47	3 (3)		N
HD 17250	10.51	0.54	42.24	0.82	9.73	2.92	42.24	1.01	3 (5)	SB	Y
HD 191089	-11.69	0.47	43.75	1.23	-11.18	3.13	43.75	1.42	4 (7)		?
V* AO Men	16.02	0.22	16.69	0.44	16.02	1.63	16.69	0.44	8 (10)		N
HD 984	-2.21	1.95	39.26	1.45	-2.21	2.30	39.26	1.59	6 (8)		N
HD 37484	21.19	0.13	52.34	1.5	21.32	2.80	52.34	1.5	2 (3)		N
2MASS J01505688-5844032	...	...	...	...	9.95	1.62	10.10	...	0 (2)		N
UCAC4 137-000439	...	...	...	...	7.69	2.41	11.20	...	0 (2)		?
2MASS J12560830-6926539	...	...	...	...	11.31	3.53	16.30	...	0 (2)		Y
BD-20 1111	19.26	0.72	24.06	4.54	18.68	1.00	24.06	5.56	3 (4)		?
Smethells 165	5.98	0.72	20.02	0.47	6.04	0.69	20.02	4.04	3 (6)		?

### 2.11.2 Notes on individual sources

#### Sources flagged variable in this work

**CD-46 644:** This target was flagged due to variation in its  $v \sin i$  value. The CCF profile is somewhat asymmetric however, the evidence is not strong enough to confirm its spectroscopic binary nature. Therefore, it was rejected as a spectroscopic binary.

**HD 17332 A:** This target has two UVES observations and no significant radial velocity variation. However, its  $v \sin i$  value was calculated to be 13 and 4 km s<sup>-1</sup> in the two epochs. Closer inspection of the CCF profile shows that the profile is well-fitted. However, given we only have two epochs, we cannot conclude whether this change is due to a companion or inherent variability of the star. Therefore, at this time we flag the system as a questionable SB and flag it for further investigation.

**CD-56 1032A:** This target has two UVES observations producing radial velocity values of 35.99 and 27.75 km/s<sup>-1</sup>. The target is a relatively fast rotator ( $v \sin i \approx 40$  km s<sup>-1</sup>) but the rotational profile is well-fitted considering its properties. Therefore,

we flagged this target as a spectroscopic binary.

**CPD-19 878:** This target shows variation in radial velocity. However, given we only have four epochs, we cannot conclude whether this change is due to a companion or inherent variability of the star. Therefore, at this time we flag the system as a questionable SB, and flag it for further investigation.

**TYC 7627-2190-1:** This target shows significant variation in radial velocity from both our observations and those including literature values. Closer inspection of its CCF profile reveals that it is likely a merged double-lined spectroscopic binary.

**V\*PXVir:** This is a known single-lined spectroscopic binary with an orbital solution ( $P = 216.48 \pm 0.06$  day), presented in Griffin (2010). In this work, when combined with literature values, the system was flagged as variable.

**HD 159911:** This target was flagged as having high  $v \sin i$  variation. Despite it has a high  $v \sin i$  value ( $\approx 58 \text{ km s}^{-1}$ ) its CCF profile is well fitted and therefore it is flagged as a potential SB1 system.

**CD-43 3604:** Its CCF profile has two clear peaks at different depths and the centre of the single Gaussian fit moves significantly from epoch to epoch. The target's rotational broadening is poorly constrained due to the merged double-peak nature of the profile. This target is likely a merged double-lined spectroscopic binary.

**V\* 379 Vel, TYC 8594-58-1, HD 37484:** These targets were flagged due to variation in its radial velocity when a literature value was included. Given that the variation come only for one extra epoch, there is not enough evidence to establish the origin of this variation. Therefore, these targets are rejected from the category of a spectroscopic binary.

**2MASS J12203437-7539286:** This target only has three observations (two presented here, the other from Torres et al. 2006). However, given its low  $v \sin i$  value ( $\approx 8 \text{ km s}^{-1}$ ) the difference in radial velocities (0.6 and  $4.8 \text{ km s}^{-1}$ ) is significant.

**HD 129496:** This target was initially flagged as having potentially variable radial velocity, however it has a very high  $v \sin i$  value ( $\approx 67 \text{ km s}^{-1}$ ). Its CCF profile is poorly fitted and, therefore, it is rejected from the category of a spectroscopic binary.

**CD-52 9381:** This target has a high  $v \sin i$  value ( $\approx 40 \text{ km s}^{-1}$ ) and was flagged due to radial velocity variation ( $\sigma_{\text{rv}} = 2.75 \text{ km s}^{-1}$ ). A closer inspection of its CCF reveals that the profile is asymmetric however, there are not two distinguishable peaks. At this time we reject this target from the category of a spectroscopic binary.

**V\*AFlep:** This target was flagged due to variation in its  $v \sin i$  value from three measurements. The CCF profile is somewhat asymmetric however, the evidence is not strong enough to confirm its spectroscopic binary nature. Therefore, it was rejected from the category of a spectroscopic binary.

**HD 139084:** This is a known single-lined spectroscopic and close visual binary. The orbital solution of this system was recently presented in Nielsen et al. (2016). The period of the system is 4.576 yr, placing it at the limit of detectability; see Fig. 2.8.

**HD 139084 B:** This target is a fast rotator ( $v \sin i \geq 50 \text{ km s}^{-1}$ ) and only has two observations (one presented here and other from Torres et al. 2006). For that reason, there is not enough evidence to establish the origin of the variation. Therefore, this target is rejected from the category of a spectroscopic binary.

**HD 164249 B:** This target was flagged for potential variable  $v \sin i$  values. However its CCF profiles are poorly fitted and therefore it was rejected from the category of a spectroscopic binary.

**CD-31 16041:** This target was flagged due to variation in its  $v \sin i$  value from three measurements. The CCF profile is somewhat asymmetric however, the evidence is not strong enough to confirm its spectroscopic binary nature. Therefore, it was rejected from the category of a spectroscopic binary.

**V\*PZTel:** This target was flagged due to variation in its  $v \sin i$  value. However, it is a very fast rotator ( $v \sin i 64 \text{ km s}^{-1}$ ) and its CCF profile is poorly fitted, there it was

rejected from the category of a spectroscopic binary.

**HD 191089:** From our measurements alone, this target would not be flagged as variable. However, with the inclusion of literature values its radial velocity significantly changes. There are two separate measurements (Gontcharov (2006):  $-5.9 \text{ km s}^{-1}$  and Desidera et al. (2015):  $-6.4 \text{ km s}^{-1}$ ). The values calculated from our three UVES observations are  $-12.18$ ,  $-12.14$ , and  $-11.24 \text{ km s}^{-1}$ . In the analysis by Grandjean et al. (2020), this source was flagged as a variable due to stellar pulsations. Therefore at this time we flag the system as a questionable SB and flag it for further investigation.

**HD 199143:** This target is a fast rotator and has been flagged for both variable  $v \sin i$  value and radial velocity. The value calculated in this work is  $v \sin i \approx 58 \text{ km s}^{-1}$ , compared to that of Torres et al. (2006),  $128 \text{ km s}^{-1}$ . A closer inspection of its CCF shows that our fit of rotational broadening is most likely underestimated due to the velocity span of the CCF fit ( $-180 - +180 \text{ km s}^{-1}$ ). Therefore, the value of  $58 \text{ km s}^{-1}$  should be treated as a conservative lower limit. Additionally the profile is extremely noisy and poorly fitted by both a Gaussian for its radial velocity value and the rotational broadening profiles. Given these limitations the system was rejected from the category of a spectroscopic binary.

**\*cEri:** This target is a very fast rotator ( $v \sin i \approx 57 \text{ km s}^{-1}$ ). Additionally, its CCF is very noisy and poorly fitted. Therefore, it is likely that the apparent radial velocity variation is not physical and the result of a poorly constrained profile. This system is rejected from the category of a spectroscopic binary.

**GJ 3305:** Given its low  $v \sin i$  value ( $\approx 5 \text{ km s}^{-1}$ ) its radial velocity variation ( $\sigma_{\text{RV}} \approx 1.6 \text{ km s}^{-1}$ ) is well above the threshold for identifying it as a spectroscopic binary.

**HD 22213:** This target has two UVES observations producing radial velocity values of  $8.13$  and  $14.41 \text{ km s}^{-1}$ . The target is a relatively fast rotator ( $v \sin i \approx 41 \text{ km s}^{-1}$ ) but the rotational profile is well fitted considering. Therefore, we flagged this target as a spectroscopic binary.

**V\*AGLep:** This target has three UVES observations and no significant radial velocity variation. However, its  $v \sin i$  value was calculated to be  $\sim 23$  and  $33 \text{ km s}^{-1}$  between the three epochs. Closer inspection of the CCF profile shows that firstly, for a relatively fast rotator the profile is well fitted. However, the shape changes significantly between the two epochs (the bisector slope, curvature and bisector inverse slope change dramatically). However, given we only have two epochs we cannot conclude whether this change is due to a companion or inherent variability of the star. Therefore at this time we flag the system as a questionable SB and flag it for further investigation.

**HD 21997:** This target was flagged as having variable  $v \sin i$ , however, given the associated uncertainty and high  $v \sin i$  value this variation is not significant.

**CD-44 753:** This target were flagged due to variation in its radial velocity when a literature value was included. Given that the variation come only for one extra epoch, there is not enough evidence to establish the origin of this variation. Therefore, this targets is rejected as a spectroscopic binary for the moment.

**HD 104467:** This target was flagged due to significant radial velocity variation. The  $v \sin i$  value of the target is  $\approx 25 \text{ km s}^{-1}$ , and the profile is well fitted. Therefore, this system is flagged as a spectroscopic binary.

**2MASS J12020369-7853012:** This target was flagged due to significant radial velocity variation. The  $v \sin i$  value of the target is  $\approx 15 \text{ km s}^{-1}$ , and the profile is well fitted. This target was previously flagged as a single-lined spectroscopic binary in Elliott et al. (2014). Therefore this system is flagged as a spectroscopic binary.

**BD-20 1111:** We have three UVES observations of this target and it has been flagged as having a variable  $v \sin i$  value. The shape of the profile significantly changes between two epochs, resulting in the different  $v \sin i$  values of  $25$  and  $15 \text{ km s}^{-1}$ . Given that we only have three epochs at present, we cannot assess whether this asymmetry is a result of the star's changing surface or of a physically bound companion. Therefore at this time we flag the target as a questionable SB system.

**CD-66 395:** This target is a very fast rotator ( $v \sin i \approx 60 \text{ km s}^{-1}$ ). Additionally, its CCF

is very noisy and poorly fitted. Therefore, it is likely that the apparent radial velocity variation is not physical and the result of a poorly constrained profile. This system is rejected as a spectroscopic binary.

**BD-184452A:** This target only has two  $v \sin i$  observations from Torres et al. 2006 and one RV value from Gaia DR2. Therefore is not enough evidence yet to establish the origin of the variation. At this time we flag the target as a questionable SB system.

**GSC 08057-00342:** This target has three radial velocity values in the literature from Rodriguez et al. (2013), Malo et al. (2014), and Kraus et al. (2014). Given its low  $v \sin i$  value ( $\approx 5 \text{ km s}^{-1}$ ) its large radial velocity variation ( $\sigma_{\text{RV}} \approx 5 \text{ km s}^{-1}$ ) is well above the threshold for identifying it as a spectroscopic binary. This object was also independently identified as a SB by Flagg et al. (2020).

**HD 17250:** This target has three RV from UVES observations and two from the literature (Gontcharov 2006; Gaia Collaboration et al. 2018). This object is the main star of a quadruple system with two visual companions and was flagged as an SB by (Tokovinin & Horch 2016).

**2MASS J04470041-5134405, UCAC3 33-129092, UCAC4 110-129613:** These targets only has two observations (one from GDR2 and other from Kraus et al. 2014). There is not enough evidence yet to establish the origin of the variation. Therefore, these target are rejected as a spectroscopic binary.

**CD-53 544:** This target was flagged due to variation in RV and  $v \sin i$  values. The CCF profile is somewhat asymmetric however the evidence is not strong enough to confirm its spectroscopic binary nature.

**TYC8098-414-1:** There are six available radial velocity measurements for this system. Five of these six measurements would give an  $\text{RV} \sim 19.60 \text{ km s}^{-1}$ , which would not be flagged as SB candidate. However, the inclusion of one value from Kraus et al. (2014) of  $-1.60 \text{ km s}^{-1}$  makes the apparent variation significant. It is difficult to assess these individual values given the available information. At this time, the system is flagged as a potential SB for further investigation.

**HD 207575:** This target shows variation in radial velocity and  $v \sin i$  value. The CCF profile shows that the shape change between the epochs (the bisector slope, curvature and bisector inverse slope). However, given we only have five epochs we cannot conclude whether this change is due to a companion or inherent variability of the star. Recently, Grandjean et al. (2020) flag this source as a variable due to pulsations from HARPS observations. Therefore, this target is rejected as a spectroscopic binary.

**HD 207964:** This target only has three observations (one from GDR2 and two from our work). Given that there is not enough evidence to establish the origin of the variation, this target is rejected from the category of a spectroscopic binary.

**TYC 9344-293-1:** This object has a variable number of  $v \sin i$  values. The values are  $61 \text{ km s}^{-1}$  (Torres et al. 2006), 59.5, 65.4 and  $67.5 \text{ km s}^{-1}$  (Malo et al. 2014) and 55, 55, and  $58 \text{ km s}^{-1}$  (this work). The most different was the value of  $33.1 \text{ km s}^{-1}$  published in Kraus et al. (2014). This system was tagged as a rotational variable but for the moment, it is rejected from the category of a spectroscopic binary.

**UCAC3 92-4597:** This target was previously flagged as a SB in (Malo et al. 2014). In this work, the system was flagged as a variable using the literature values.

**CD-30 3394, CD-30 3394B:** These objects were flagged due to RV variation. The CCF profile shows that the shape change between the epochs (the bisector slope, curvature, and bisector inverse slope). However, given we only have four epochs we cannot conclude whether this change is due to a companion or inherent variability of the star. At this time, the systems are flagged as a potential SBs for further investigation.

**HD 3221:** This target is a very fast rotator ( $v \sin i \geq 68 \text{ km s}^{-1}$ ) and its profile is extremely noisy and poorly fitted. For that reason the radial velocity variation is likely to be non-physical. Therefore, this target is rejected from the category of a spectroscopic binary.

**SCRJ0103-5515:** This target was previously flagged as a double or multiple star in WDS. In this work, the system was flagged as a variable using the literature values

from (Malo et al. 2014) and (Kraus et al. 2014).

**V\* CE Ant** : This target was flagged due to variation in its  $v \sin i$  value from our measurements. The CCF profile is somewhat asymmetric, however, the evidence is not strong enough to confirm its spectroscopic binary nature. Therefore, it was rejected from the category of a spectroscopic binary.

**TWA23**: This target has 16 individual radial velocity measurements (the majority from Bailey et al. 2012) and shows significant radial velocity variation. Although we only have one observation, from UVES, the profile is consistent as resulting from a merged SB2 system. There is a significant asymmetry at approximately half the depth of the profile, causing a large bisector slope. Therefore this target is flagged as an SB2 system.

**V\* AO Men**: This target was flagged due to variation in its radial velocity when a Gaia DR2 value was included. Given that the variation come only for one extra epoch, there is not enough evidence to establish the origin of this variation. On the other hand, Grandjean et al. (2020) estimated that the variation was due to stellar activity (spots). Therefore, this target is rejected from the category of a spectroscopic binary.

**HD 984**: This target was flagged due to variation in its radial velocity when a Gaia DR2 value was included. Johnson-Groh et al. (2017) calculated the orbit of this system as  $\sim 70$  yr, which is outside outside the region where a visual binary can be detected through radial velocity variation given  $\sim 10$  yr measurements. Therefore, although this object is a visual binary, it cannot be flagged as a spectroscopic binary.

**2MASS J01505688-5844032, UCAC4 137-000439**: These targets were flagged due to variation in its radial velocity from two literature values (Kraus et al. 2014; Gaia Collaboration et al. 2018). Shan et al. (2017) did not find sign of companion from adaptive optics observations conducted on the 6.5 m Magellan Clay Telescope for these objects. UCAC4 137-000439 was noted as potential tight binary in Janson et al. (2017) with an estimated separation of  $\sim 0.01''$ . 2MASS J01505688-5844032 is rejected from the category of a spectroscopic binary for the moment and UCAC4 137-000439 is flagged as a potential SB for further investigation.

**2MASS J12560830-6926539:** This target only has two observations (one from Torres et al. 2006 and another from Gaia DR2). Elliott et al. (2015) probed binarity in this object by high-resolution imaging with an estimated angular separation of  $0.1''$ , physical separation of 13.1 au and a mass ratio of 0.55. This object is at the boundaries of the region where a visual binary can be detected through radial velocity variation given  $\sim 10$  yr measurements. At this time, we flag the target as a questionable SB system.

**Smethells 165:** This target was previously flagged as a double or multiple star in WDS. In this work, the system was flagged as a variable using the  $v \sin i$  values from literature. The variation came from one  $v \sin i$  measurement from Kraus et al. (2014). At this time, we flag the target as a potential SB for further investigation.

### **Sources previously flagged as spectroscopic multiple systems not recovered in this work**

**CD-29 4446:** This is a known binary system with an orbital solution presented in Rodet et al. (2018). In this work, the system was flagged as a variable using the literature values.

**V\* V1005 Ori:** This target was flagged as an SB1 system in Elliott et al. (2014). The compilation of further radial velocities do not show significant radial velocity variation caused by a companion.

**HD 98800A:** Torres et al. (1995) calculated the orbit of this SB1 system as 262 day. In the results presented here we only have two radial velocity values which are four days apart and, therefore, did not detect any significant change in velocity. This is one of the few clear spectroscopic systems missed by our analysis.

**CD-33 7795:** This target is a known triple system with companions at  $\approx 0.06''$  (Macintosh et al. 2001) and  $2''$  (Webb et al. 1999). Konopacky et al. (2007) calculated the orbit of the inner system as  $5.94 \pm 0.09$  yr, which puts it in the approximate region where a visual binary can be detected through radial velocity variation given  $\sim 10$  yr measurements. However, this object is a fast rotator ( $v \sin i \approx 50 \text{ km s}^{-1}$ )

and only has two epochs of radial velocity data which do not show significant variation. Therefore, although this object is a visual binary it cannot be flagged as a spectroscopic binary.

**HD 13183:** This target was flagged as a potential SB1 system in the CORAVEL database (Nordstrom et al. 1996). Furthermore, Cutispoto et al. (2002) found evidence for significant radial velocity variation. From our compilation of values, this system does not exhibit significant variation given its rotational velocity ( $v \sin i \approx 24 \text{ km s}^{-1}$ ); however, it does have an asymmetrical CCF profile. Given the previous notes in multiple other works, this system is flagged as a spectroscopic binary.

### **Double- and triple-lined spectroscopic binaries**

Double- and triple-lined spectroscopic multiple systems can be identified from a single epoch of data and are essentially confirmed as multiple systems with one detection. For that reason, the notes below on each system are brief, with references to their original discovery where applicable.

**HD 67945:** This target was flagged as a potential SB2 system in Torres et al. (2006). However, given its extremely fast rotation  $v \sin i \geq 58 \text{ km s}^{-1}$  and extremely noisy CCF profile we do not find sufficient evidence to confirm that. Additionally it does not have significant radial velocity variation. Therefore, it was rejected from the category of a spectroscopic binary.

**HD 155177** There are three individual radial velocity values for this target with uncertainties  $< 3 \text{ km s}^{-1}$ , two of which are calculated in this work. Both the shape ( $b_b, c_b$  and  $BIS$ ) and the peak of the CCF profile change significantly across the two observations. Therefore, this system is flagged as a spectroscopic binary.

**GSC 06513-00291:** Malo et al. (2014) flag this system as an SB2 and quote values of 12.1, 21.6 and 2.4 for  $v \sin i$  of this target from three observations. Interestingly the RV values from the three epochs 22 and 23.9 and 22.8 do not vary significantly. This target has a companion at  $\approx 0.1''$ . Therefore, it is likely an SB3 system. The companion at  $0.1''$  (3 au using a trigonometric distance of 29.4 pc, Riedel et al. 2014) would have

a period  $>1000$  day. Such a period would not typically induce a large RV difference unless the orbit was extremely eccentric. This system is therefore flagged as an SB3.

**V4046 Sgr:** This target is a well-known SB2 system, the orbital solution was presented in R. Quast et al. (2000). We recover both components of this system in all CCF profiles.

**LP 476-207 A:** This is a known SB2 system whose orbital solution was presented in Delfosse et al. (1999). We recover both components of this system in all CCF profiles.

**Barta 161 12:** We do not have our own observations of this target and therefore cannot further investigate the spectroscopic binary-nature of this object with our measurements. However, Malo et al. (2014) reported this target as an SB2 system. There are multiple radial velocity measurement that show apparent variation, however, it was not recovered in our analysis as the majority of measurements have uncertainties larger than  $3 \text{ km s}^{-1}$ . This target is therefore flagged as a spectroscopic binary.

**HD 217379A:** This is a previously discovered SB3 system (Elliott et al. 2014). More recently, Tokovinin (2016a) presented an orbital solution for both the inner and outer system. We recover all three components of this system in our CCF profiles.

**TWA 3A:** This target was flagged as an SB2 system in Malo et al. (2014) We do not have further observations from UVES, FEROS or HARPS. However, from our compilation of radial velocities this system has significant radial velocity variation.

**UCAC3 112-6119, UCAC3 92-4597:** Kraus et al. (2014) flagged these two targets as an SB2 systems. We do not have further observations from UVES, FEROS, or HARPS. However, from our compilation of radial velocities these systems have significant radial velocity variation.

**HD 309751, HD 33999:** These two systems were previously reported in Elliott et al. (2014) and recovered in this analysis.

**HD 36329:** This SB2 system was previously reported in Torres et al. (2006) and recovered in this analysis.

**TYC 8098-414-1:** Kraus et al. (2014) noted this target as an SB2 system, however, we do not recover the component in our analysis. Most likely the companion is not detected as its flux ratio is too low in our optical spectra. Malo et al. (2014) also noted that their  $v \sin i$  value did not agree with the literature values and mentioned that this could be an unresolved spectroscopic binary. Given this information the system is flagged as an SB2 in our analysis.

**HD 199058:** Chauvin et al. (2015) noted this object as a binary or multiple system. In this work we flagged this target as an SB2.

**TYC 6872-1011-1, BD-20 951, GSC 08077-01788, UCAC3 116-474938, V\* V1215 Cen, HD 36329:** To the best of our knowledge these systems have not previously been reported in the literature. All are newly discovered SB2 systems.

### 2.11.3 Measurements of $v \sin i$

#### Calibrating using CCF width

In the case of slow rotators ( $v \sin i \lesssim 20 \text{ km s}^{-1}$ ), there is a significant contribution to the width ( $\sigma_{\text{obs}}$ ) of the cross correlation function (CCF) from non-rotation related broadening mechanisms which can either be inherent to the star (effective temperature and turbulence) or from the instrument that is used for the observation. The width of the CCF profile is described by:

$$\sigma_{\text{obs}}^2 = \sigma_{\text{rot}}^2 + \sigma_0^2, \quad (2.4)$$

where  $\sigma_{\text{obs}}$  is the width of the resultant CCF profile,  $\sigma_{\text{rot}}$  is the rotational broadening of the star and  $\sigma_0$  is the width of a non-rotating star, which can be very well expressed as a function of colour.

Beyond  $\approx 20 \text{ km s}^{-1}$  the width of the CCF profile is dominated by the rotation of the star and therefore these effects become small or negligible. We note that within our sample of objects there are very few measurements with FEROS or HARPS with  $v \sin i$  values  $\geq 20 \text{ km s}^{-1}$ .

The  $v \sin i$  value can be expressed as (Queloz et al. 1998):

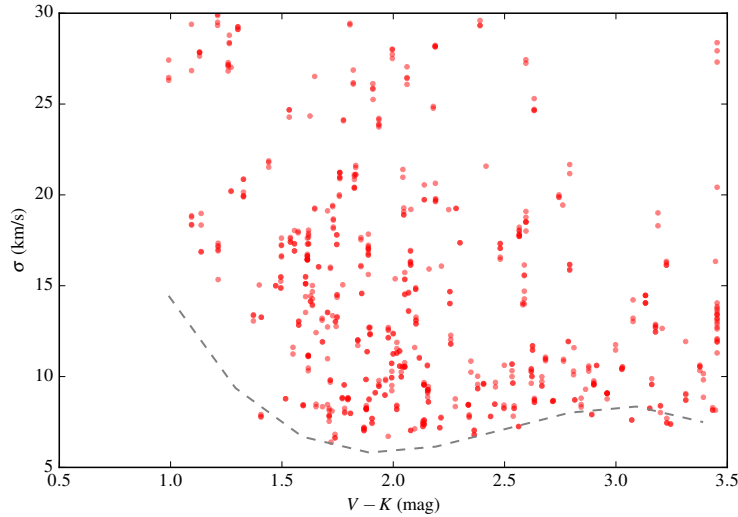
$$v \sin i = A \sqrt{\sigma_{\text{obs}}^2 - \sigma_0^2}, \quad (2.5)$$

where  $A$  is the coupling constant, calibrating one set of CCF measurements to previously calibrated  $v \sin i$  values.

Firstly, to determine the value of  $\sigma_0$ , we computed the lower envelope of points in a  $V - K$  versus  $\sigma_{\text{obs}}$  diagram; see Fig. 2.13 for an example using UVES observations. The envelope was fitted with a polynomial and is shown as the dotted line. This is similar to the technique used in Melo et al. (2001) and Boisse et al. (2010). We used this  $\sigma_0$  value for each star with its respective  $V - K$  colour and found the slope (and offset) between published  $v \sin i$  values and our calculated  $A \sqrt{\sigma_{\text{obs}}^2 - \sigma_0^2}$  values. We note that in this analysis we used CCF profiles with low fit residuals in order to better constrain the results.

Figure 2.14 shows the resultant relation for observations using UVES. We have highlighted three regions of the Fig. to guide the reader's eye. Below  $\approx 6 \text{ km s}^{-1}$ , in the case of UVES,  $\sigma_0 \approx \sigma_{\text{obs}}$  and, therefore, this is our reliable lower limit on  $v \sin i$

values. Between  $\approx 6\text{--}20 \text{ km s}^{-1}$  the 1:1 linear relation sufficiently describes the majority of our data.



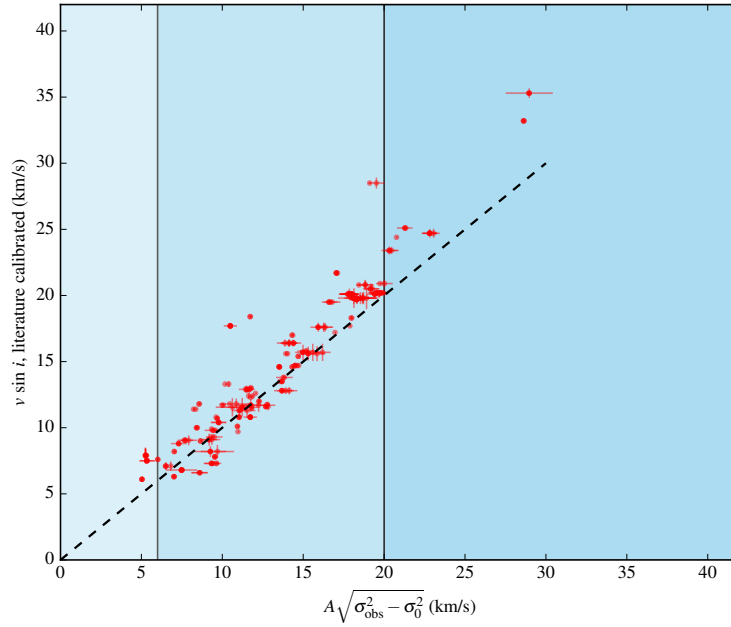
**Figure 2.13:**  $V - K$  colour versus  $\sigma$  (the observed width of the CCF profile) for all individual UVES observations. The dotted line represents a polynomial fitted to the lower envelope of these measurements.

Figure 2.14 shows that, at least in the case of UVES observations, this calibration is relatively successful as the literature  $v \sin i$  values match the  $A\sqrt{\sigma_{\text{obs}}^2 - \sigma_0^2}$  value. However, in the case of FEROS and HARPS we were unable to perform the same analysis successfully. Due to the smaller number of objects an accurate calculation of  $\sigma_0$  was severely inhibited. With this in mind, below we outline an alternative approach to  $v \sin i$  calculation.

### Calibrating using rotational profiles

We directly compared our calculated values using rotational profiles to published values. We used  $v \sin i$  with published uncertainties  $< 3 \text{ km s}^{-1}$  in this analysis. Figure 2.15 shows the results for UVES, FEROS and HARPS in the left, middle and right panels, respectively. A linear relation ( $y = mx + c$ ) was fitted to each set of points and was used to calibrate our values.

To verify this relationship we performed an internal check by comparing  $v \sin i$  values for objects that were observed with at least two of the three instruments. Figure 2.16 shows the results of this comparison for each pair of instruments. Given



**Figure 2.14:**  $A\sqrt{\sigma_{\text{obs}}^2 - \sigma_0^2}$  versus literature  $v \sin i$  values for UVES observations. Three regions are highlighted. From left to right: Our lower limit on reliable  $v \sin i$  values ( $6 \text{ km s}^{-1}$ ), the intermediate range ( $6\text{-}20 \text{ km s}^{-1}$ ) where the 1:1 relation should hold and the fast rotator range ( $> 20 \text{ km s}^{-1}$ ). The dotted line represents the 1:1 relation between the two sets of values.

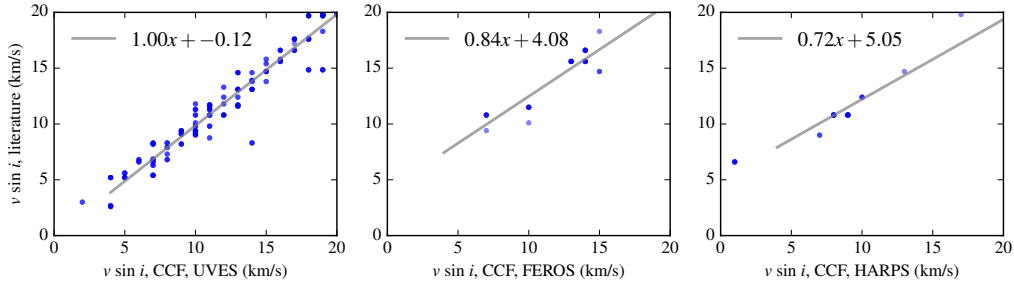


**Figure 2.15:**  $v \sin i$  values from fitted rotational profiles versus literature  $v \sin i$  values. The left, middle and right panels show measurements for UVES, FEROS and HARPS observations. The linear relation ( $y = mx + c$ ) is shown for each set of measurements.

typical uncertainties on  $v \sin i$  values are  $1\text{-}2 \text{ km s}^{-1}$  (Melo et al. 2001; Malo et al. 2014) the resultant 1:1 relationships adequately describe our data. The advantage of this calibration technique is that the linear relation can be applied to all stars in our sample. However, in the case of the technique described in Sect. 2.11.3, a  $V - K$  value is

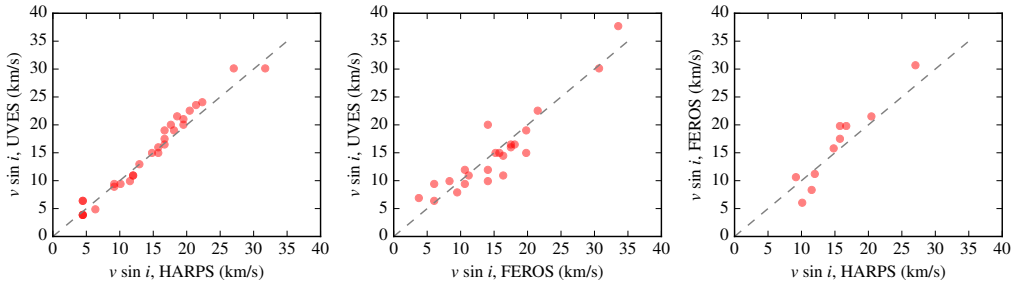


**Figure 2.16:**  $v \sin i$  values calculated in this work for each pair of instruments. Left, middle and right panels are HARPS versus UVES, FEROS versus UVES and HARPS versus FEROS, respectively. The 1:1 relation in each case is plotted as the dotted line.

needed and some stars in our sample do not have reliable  $V$  magnitudes. Additionally, our stars cover the age range  $\approx 5$ -150 Myr and therefore can be at very different evolutionary stages, which could hinder a robust  $\sigma_0$  calculation.

### $v \sin i$ lower limit

From our calibration of  $v \sin i$  values described in the previous section, we arrive at lower limits of 0.83, 4.47 and 8.36  $\text{km s}^{-1}$  using a star rotating with a projected rotational velocity of 1  $\text{km s}^{-1}$  for UVES, HARPS and FEROS, respectively. However, as highlighted in Sect. 2.11.3, we take a more realistic lower limit on  $v \sin i$  values for UVES is 6  $\text{km s}^{-1}$ , where  $\sigma_0 \approx \sigma_{\text{obs}}$ .

### Limitations on $v \sin i$ measurements of extremely fast rotators

In the case of very large rotational broadening ( $v \sin i \geq 60 \text{ km s}^{-1}$ ), some stars'  $v \sin i$  values can be underestimated. This is due to the width of the profile approaching the width of the velocity span used in the CCF calculation. This causes a lack of continuum and when the profile is fitted the outer wings of the profile can be wrongly ignored. For fast rotators in our sample ( $v \sin i \geq 50 \text{ km s}^{-1}$ ), we reran our CCF calculation using a wider velocity window of -250 to +250  $\text{km s}^{-1}$ . Even with this broader window some star's CCF profile widths were still underestimated. In these cases, we use our calculated value as a lower limit.

**Measurement uncertainties on  $v \sin i$  values**

We compared our calibrated  $v \sin i$  values with the fitted linear relation (see Sect. 2.11.3) and calculate the quadratic sum of the error as tracer of uncertainties. We set three uncertainties values based on three order of magnitude from residuals. These values were selected from the mean uncertainty value from the errors between the calibrated  $v \sin i$  and the fitted linear relation on each range of profile fit residuals (see Fig. 2.17).

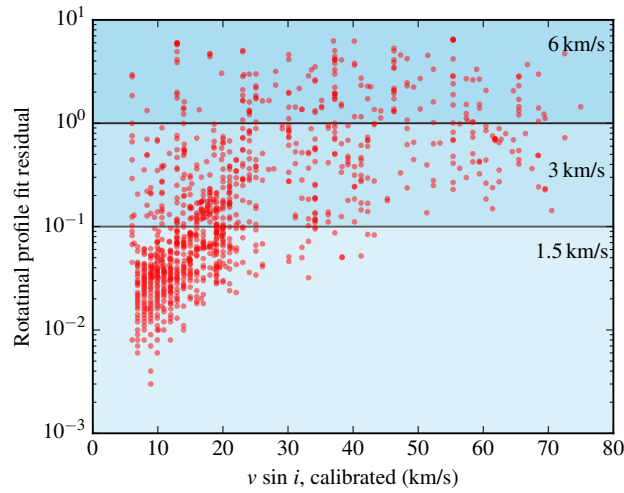


**Figure 2.17:** Rotational profile fit residual as a function of calibrated  $v \sin i$  values. The  $v \sin i$  uncertainties value is defined depending on the range of fit residual values.

## 2.11.4 SB1 systems identified in this work

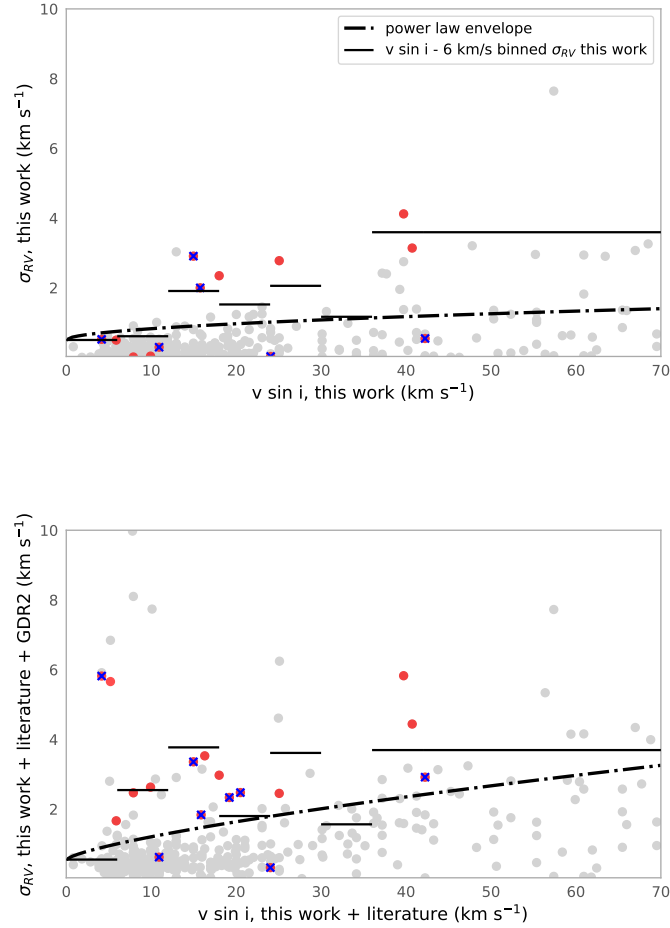


**Figure 2.18:** *Upper panel:* Standard deviation in RV as a function of  $v \sin i$  for measurements calculated in this work. The  $3\sigma$  value from binning in  $6 \text{ km s}^{-1}$  bins are represented by the solid lines. The power law envelope is represented by dash-dotted line. The SB1s identified in this work are plotted as a red dots and the previously identified SB1s from literature are represented as a blue crosses. *Bottom panel:* Same as upper panel but including values from literature and Gaia DR2. Some SB1 were confirmed only when literature values were included (red dots under the  $3\sigma$  envelope in upper panel). Details on each candidate can be found in Appendix 2.11.2.

### 2.11.5 Gaia DR2

Example of the sanity checks performed regarding the correct identification of the Gaia DR2 counterparts to the SACY members.

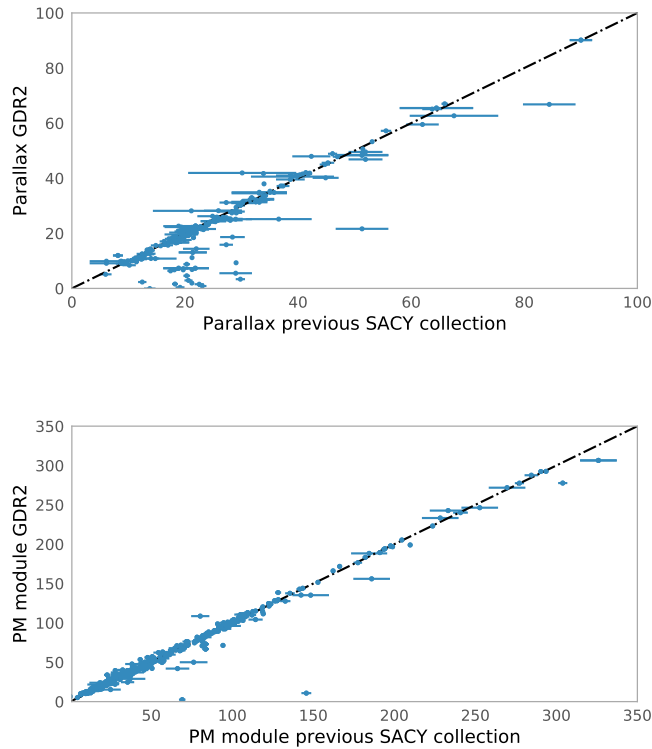


**Figure 2.19:** Possible mismatched results was visually inspected and crosschecked to avoid false positives. The dotted-dashed line represent the 1:1 relation.

### 2.11.6 Rotational periods from light curves

In Fig. 2.20, we show an example of the TESS light curve folded to the period estimated in this work for GSC 07396-00759. The lower panel shows the residuals obtained after subtraction of the binned and smoothed phased light curve to be used to asses the reliability of the period. We can see that despite possible flares in the data-set, our procedure offers a simple but robust diagnostic. On the other hand, as it is evident from Fig. 2.21, the aperture used to derive the TESS light curve is contaminated by similar brightness objects and, therefore, we cannot assure that the reported value is the rotational period of this particular source.

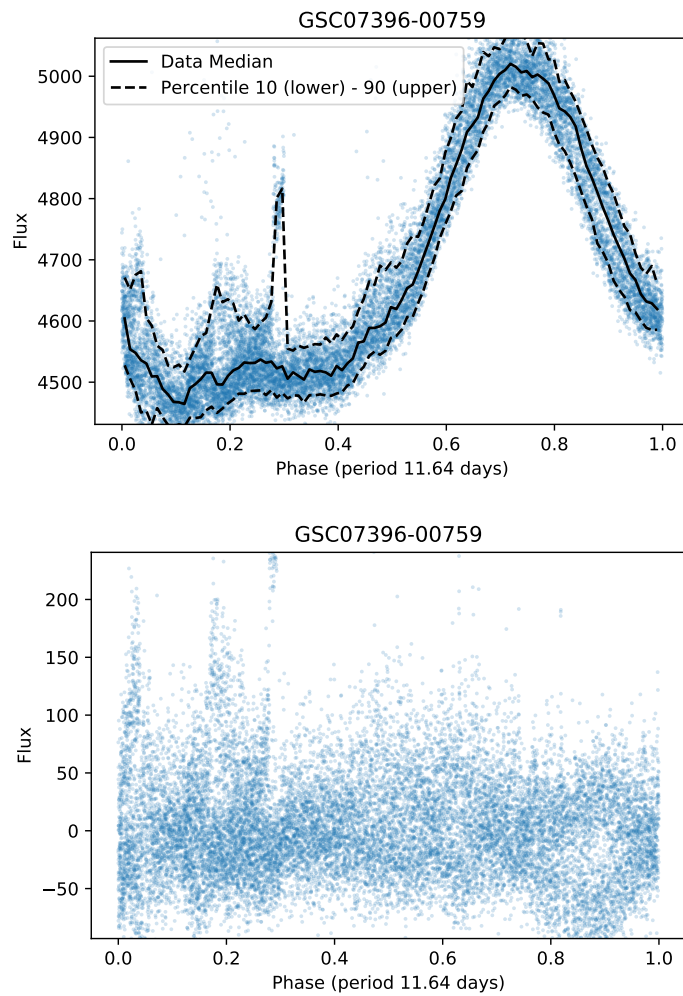


**Figure 2.20:** *Upper panel:* Phased light curve for GSC 07396-00759. The solid line represent the median calculated by binning the phased curve in 100 bins. The MAD for the phased curve for this object is 652.67. *Bottom panel:* Residuals from subtracting light curve values from the ‘median model’ (solid line). The MAD of the residuals is 121.84.

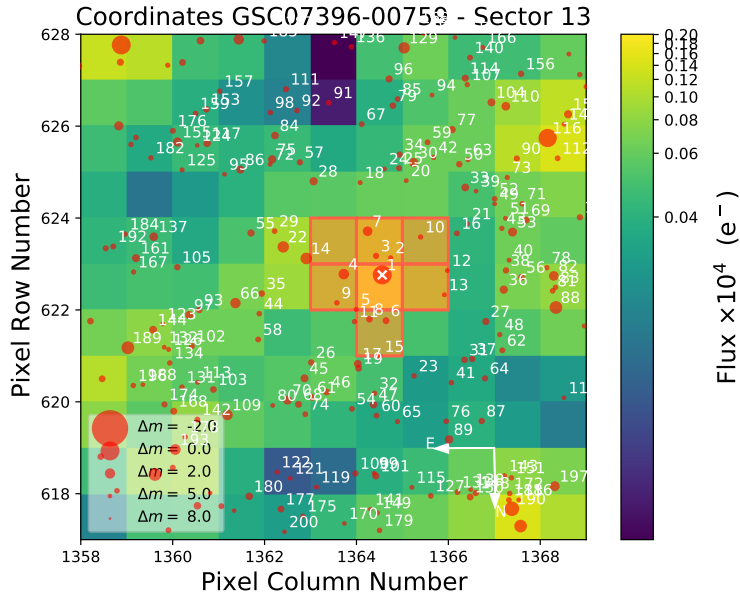


**Figure 2.21:** Output figure for GSC 07396-00759 from the package `tpfplotter` (Aller et al. 2020). We count the number of Gaia sources within a  $\Delta G \text{ mag} \leq 5$  of the science target that fall in the pipeline aperture of TESS and save the minimum  $\Delta G \text{ mag}$  value to assess the quality of the rotational period.

### 2.11.7 Sensitivity maps

Average detection probability maps (contours from red, 100%, to white, 0%) computed for the population of binaries described in Sect. 2.7. Detected spectroscopic companions (white stars) and visual binaries (black crosses) in the physical separation versus mass ratio. The solid, dashed, and dash-dotted lines encompass areas with detection probabilities  $\geq 90\%$ ,  $50\%$  and  $10\%$ , respectively. For THA and BPC association see Fig. 2.8

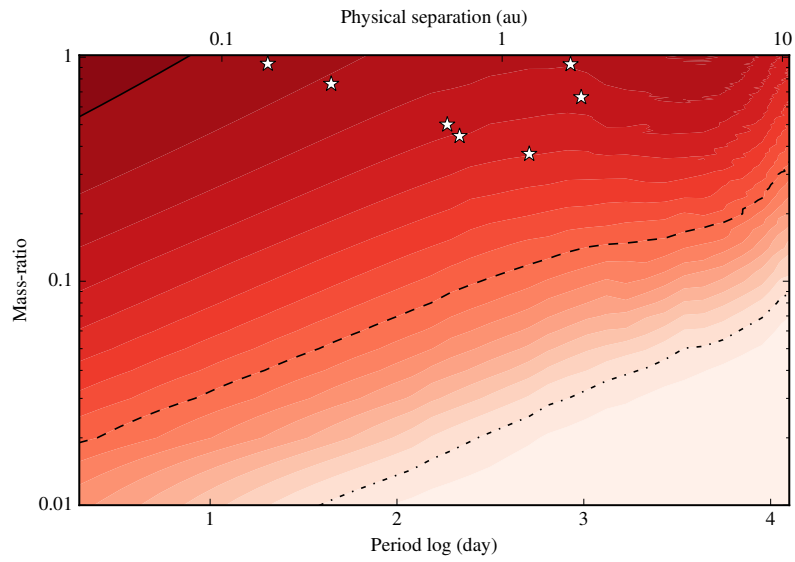


**Figure 2.22:** Average detection probabilities for ABD association.

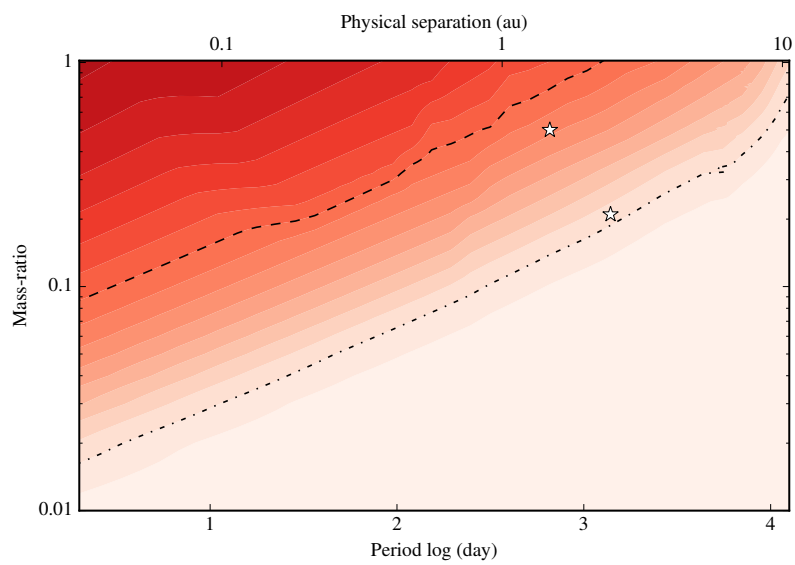


**Figure 2.23:** Average detection probabilities for ARG association.

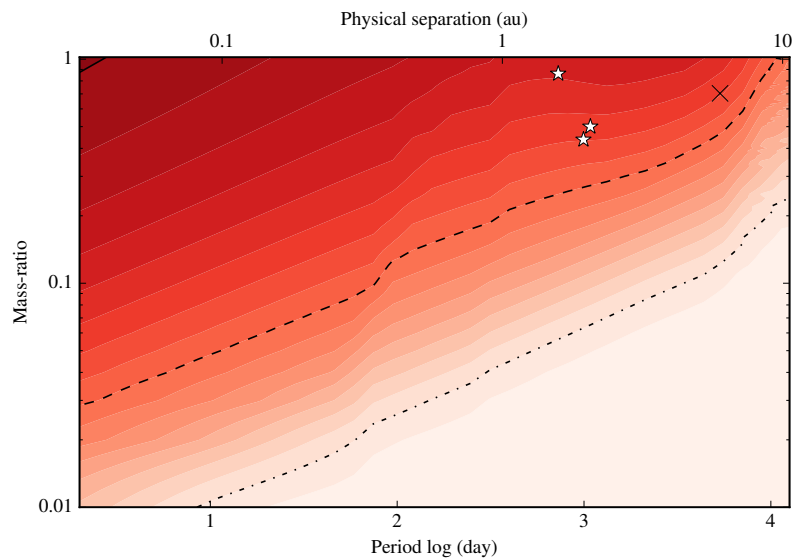


**Figure 2.24:** Average detection probabilities for COL association.

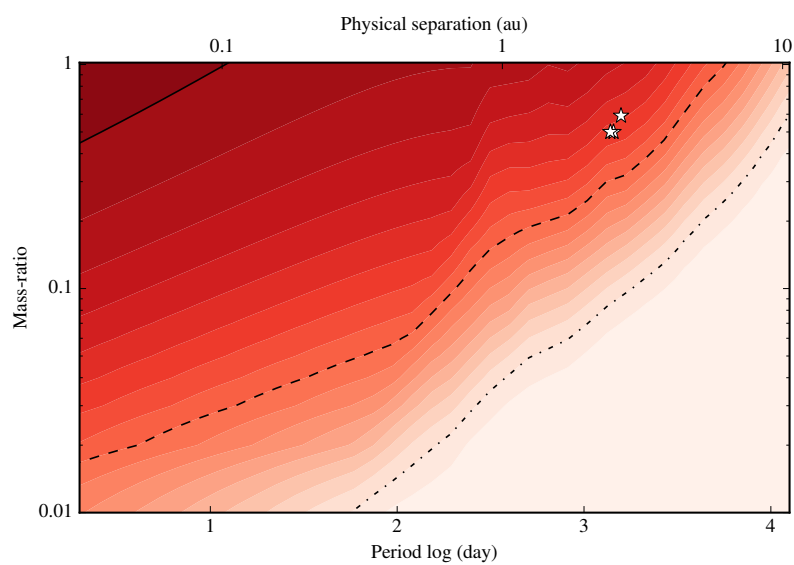


**Figure 2.25:** Average detection probabilities for ECH association.

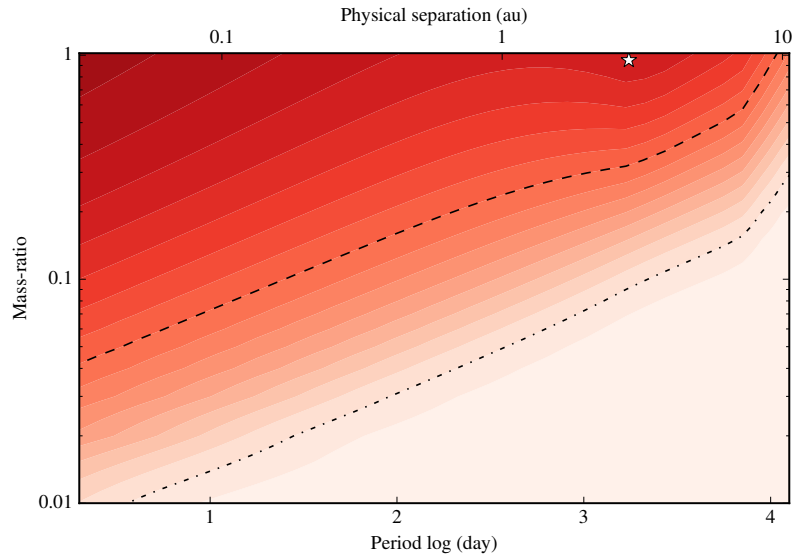


**Figure 2.26:** Average detection probabilities for OCT association.

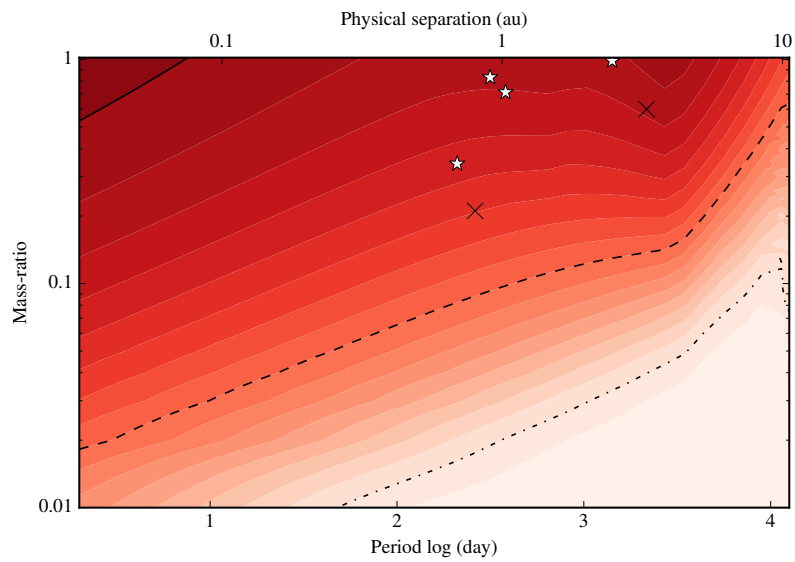


**Figure 2.27:** Average detection probabilities for TWA association.

### 2.11.8 Individual and summary tables

**Table 2.4:** Table of all individual radial velocity values calculated in this work and compiled from the literature/Gaia DR2 (first 10 rows). The full table (2048 RV values) is published online in the machine-readable format. The high order features (BIS,  $b_b$ ,  $c_b$ ) are available for all our CCF calculations. The reference code in *Ref.* column correspond to: ZF20: this work or updated value of Elliott et al. (2014), SC12: Schlieder et al. (2012), SH12: Shkolnik et al. (2012), TO06: Torres et al. (2006), LO06: Lopez-Santiago et al. (2006), RO13: Rodriguez et al. (2013), MA10: Maldonado et al. (2010), MO13: Moór et al. (2013), RE09: Reiners & Basri (2009), GO06: Gontcharov (2006), MA14: Malo et al. (2014), KR14: Kraus et al. (2014), MO01b: Montes et al. (2001), MO02: Mochnacki et al. (2002), BA12: Bailey et al. (2012), DE15: Desidera et al. (2015) and GDR2: Gaia DR2, Gaia Collaboration et al. (2018). The MJD and instrument information is not available for all rows in the table, more details in Sect. 2.2.

SIMBAD ID	RA J2000 (deg)	DEC J2000 (deg)	RV	RV err	MJD	BIS	$b_b$	$c_b$	Instrument	Ref.
BD-202977	144.964005	-21.571400	18.87	0.532750	53906	-0.404	-8.353	-0.150	FEROS	ZF20
BD-202977	144.964005	-21.571400	17.73	0.532750	54240.1	-0.103	-2.283	-0.138	UVES	ZF20
BD-202977	144.964005	-21.571400	17.75	0.532750	54240.1	-0.089	-1.893	-0.133	UVES	ZF20
HD99827	171.324005	-84.954399	20.01	1.390170	54906.3	-0.430	-73.848	-0.676	UVES	ZF20
HD99827	171.324005	-84.954399	19.94	1.390170	54906.3	-0.747	-60.319	-0.830	UVES	ZF20
HD99827	171.324005	-84.954399	16.30	1.390170	55371.1	0.894	7.246	-1.184	UVES	ZF20
HD99827	171.324005	-84.954399	19.42	1.390170	56734.3	1.609	81.204	-0.746	UVES	ZF20
HD99827	171.324005	-84.954399	19.55	1.390170	56748.1	0.810	9.514	-2.268	UVES	ZF20
CD-691055	194.606995	-70.480301	13.70	0.894763	54577	-1.860	-90.714	4.322	FEROS	ZF20
CD-691055	194.606995	-70.480301	12.53	0.894763	55978.4	1.439	13.629	2.944	UVES	ZF20

**Table 2.5:** Table of all individual rotational velocity values calculated in this work and compiled from literature (first 10 rows). The full table (1480  $v \sin i$  values) is published online in the machine-readable format. The reference code in *Ref.* column correspond to: ZF20: this work, SC12: Schlieder et al. (2012), TO06: Torres et al. (2006), MA14: Malo et al. (2014), BA12: Bailey et al. (2012) and DE15: Desidera et al. (2015).

SIMBAD ID	RA J2000 (deg)	DEC J2000 (deg)	vsini	vsini err	Ref.
BD-202977	144.964005	-21.571400	13.49	1.5	ZF20
BD-202977	144.964005	-21.571400	9.92	1.5	ZF20
BD-202977	144.964005	-21.571400	9.92	1.5	ZF20
HD99827	171.324005	-84.954399	41.23	3.0	ZF20
HD99827	171.324005	-84.954399	40.22	3.0	ZF20
HD99827	171.324005	-84.954399	39.21	3.0	ZF20
HD99827	171.324005	-84.954399	41.23	3.0	ZF20
HD99827	171.324005	-84.954399	41.23	6.0	ZF20
CD-691055	194.606995	-70.480301	15.20	6.0	ZF20
CD-691055	194.606995	-70.480301	28.10	6.0	ZF20

**Table 2.6:** Component radial velocity values for SB2 systems estimated in this work.

SIMBAD ID	RA J2000 (deg)	DEC J2000 (deg)	RV1	RV1 err	RV2	RV2 err	MJD
GSC08077-01788	72.970802	-46.791901	-21.2927	1.618303	70.72530	0.694135	56735.1
GSC08077-01788	72.970802	-46.791901	-15.4776	1.312729	65.67440	1.338559	56738.1
HD199058	313.588013	9.040000	-30.0904	1.000865	-11.77740	1.547928	56828.4
HD199058	313.588013	9.040000	-24.9204	0.972239	-13.04740	1.352694	56836.3
HD199058	313.588013	9.040000	-24.5381	0.860092	-15.96410	1.037438	57275.1
HD199058	313.588013	9.040000	-25.0000	0.904851	-13.90000	1.964319	54783.0
HD36329	82.350403	-34.515598	23.8599	0.979925	23.85990	0.904718	57271.4
HD36329	82.350403	-34.515598	-44.8610	1.290879	90.64900	1.382289	57276.4
HD36329	82.350403	-34.515598	-19.5175	1.143967	68.21940	1.918715	57295.3
HD51062	103.447998	-43.114201	14.6000	0.912295	38.90000	0.997951	55522.3
HD99827	171.324005	-84.954399	1.7000	1.269730	33.50000	1.642376	54169.2
UCAC3116-474938	299.011993	-32.121899	-29.8203	1.363111	15.90560	1.102911	57255.3
UCAC3116-474938	299.011993	-32.121899	-66.4405	1.185148	54.73050	1.044546	57272.1
UCAC3116-474938	299.011993	-32.121899	-40.6756	1.003758	28.52240	1.520679	57275.1
UCAC3116-474938	299.011993	-32.121899	-14.4882	1.280286	2.47079	0.857250	57292.2

**Table 2.7:** Summary table of the sample presented in this work. This table is available only in electronic format.

Label	Units	Description
Simbad ID		Simbad identifier
RA J2000	degrees	Right ascension at J2000
DEC J2000	degrees	Declination at J2000
$RV_{\text{median}}$ CCF	$\text{km s}^{-1}$	Median RV from our CCF calculation
$\sigma_{RV}$ CCF	$\text{km s}^{-1}$	Standard deviation in RV from our CCF calculation
$v\text{sini}_{\text{median}}$ CCF	$\text{km s}^{-1}$	Median $v \sin i$ from our CCF calculation
$\sigma_{v \sin i}$ CCF	$\text{km s}^{-1}$	Standard deviation in $v \sin i$ from our CCF calculation
$N_{\text{obs}}$ CCF		Number of observation from our CCF calculation
$RV_{\text{median}}$	$\text{km s}^{-1}$	Median RV from our work + literature
$\sigma_{RV}$	$\text{km s}^{-1}$	Standard deviation in RV from our work + literature
$N_{\text{obs}}$ RV		Number of RV observations from our work + literature
$v\text{sini}_{\text{median}}$	$\text{km s}^{-1}$	Median $v \sin i$ from our work + literature
$\sigma_{v \sin i}$	$\text{km s}^{-1}$	Standard deviation in $v \sin i$ from our work + literature
$N_{\text{obs}}$ vsini		Number of vsini observations from our work + literature
Period	days	Period from light curves
$\sigma_{\text{Period}}$	days	Period uncertainty
FAP		False alarm probability
Phased-MAD		MAD on phased light curve
Residual-MAD		MAD on residuals of phased light curve
P-MAD/R-MAD		Ratio between phased-MAD and residuals-MAD
INSTR.		Instrument that has measured the light curve
TESS sector		TESS sector
TESS/K2 ID		TESS or K2 identifier
$N_{\text{sources}}$ TESS		number of sources in TESS aperture with $\Delta G\text{mag} < 5$
$\text{Min}_{\Delta G\text{mag}}$ TESS	mag	Minimum $\Delta G\text{mag}$ in TESS aperture
LC notes		Light curves notes on the object
LC $q_{\text{flag}}$		Light curve quality flag (Good, Caution or Bad)
GaiaDR2 ID		Gaia DR2 source identification
mass	$M_{\odot}$	Stellar mass
Spt		Spectral type
$\text{SACY}_{MG}$		Best MG match from SACY convergence method
$\text{SACY}_p$		SACY membership probability
$\text{BAN}_{MG}$		Best MG match from BANYAN $\Sigma$
$\text{BAN}_p$		BANYAN $\Sigma$ membership probability
Notes		Notes on SB candidates

## CHAPTER 3

# The HD 98800 quadruple pre-main sequence system

This chapter have been previously published as “The HD 98800 quadruple pre-main sequence system. Towards full orbital characterisation using long-baseline infrared interferometry”. Zúñiga-Fernández, S., Olofsson, J., Bayo, A., Haubois, X., Corral-Santana, J. M., Lopera-Mejía, A., Ronco, M. P., Tokovinin, A., Gallenne, A., Kennedy, G. M., and Berger, J.-P, *A&A*, 655, A15 (2021).

### 3.1 Introduction

Solar-type multiple systems are at least as common as individual stars: the fraction of triple-star systems was found to be  $8 \pm 1\%$ , and it drops to  $3 \pm 1\%$  for higher-multiplicity systems (Raghavan et al. 2010). Similarly, observations of F and G stars within 67 pc of the Sun (Tokovinin 2014a,b) show that  $\approx 10\%$  of all stellar systems are triple and  $\approx 4\%$  are quadruple. The high-order multiplicity fraction increases with stellar mass (Duchêne & Kraus 2013). Multiple star systems with  $n > 2$  are nearly always hierarchical, meaning that they can decompose into binary or single sub-systems based on their relative separations (e.g. two close binaries that orbit each other with a wide separation). A hierarchical system can have many distinct config-

urations. For instance, quadruple systems can have two possible configurations. A triple system orbited by a distant fourth companion corresponds to the 3+1 configuration. The 2+2 configuration consists in two close binaries orbiting around each other. The 2+2 configuration seems to be  $\sim 4$  times more frequent than the 3+1 configuration for solar-type stars (Tokovinin 2014b). The orbital parameters in hierarchical systems could provide additional information about their formation history. It is expected that different formation processes, such as core fragmentation, disk instability, dynamical interactions, or a combination of different formation channels, leave imprints on the mass ratio, periods, eccentricities, and mutual orbit inclination of hierarchical systems (Kozai 1962; Lidov 1962; Whitworth 2001; Sterzik & Tokovinin 2002; Lee et al. 2019; Tokovinin & Moe 2020). In the last decades, observational and theoretical efforts have led to a better understanding of the formation and dynamical stability of such multiple systems (Kiselev & Kiyayeva 1980; Tokovinin et al. 2006; Eggleton 2009; Tokovinin 2018a; Hamers et al. 2021).

Wide binaries show a strong preference to be in hierarchical systems in low density young associations (Elliott et al. 2016a; Elliott & Bayo 2016) and star-forming regions (Joncour et al. 2017). The fact that this relation is not seen in the same proportion in denser environments or systems in the field suggests that this could be the result of dynamical processing or the unfolding of hierarchical systems (Sterzik & Tokovinin 2002; Reipurth & Mikkola 2012). In that regard, characterising young (1-100 Myr), hierarchical systems helps to observe their early evolution. The formation channels of hierarchical systems cannot be easily determined by only characterising field stars, where billions of years of dynamical evolution may have erased their formation history. Consequently, the study of young (1-100 Myr) hierarchical systems is an important step to better understand their formation pathway. Large-scale surveys provide crucial information that helps to discover such multiple systems, but they are not well suited to finely constrain their orbital architecture. We need high-precision astrometry and radial velocity (RV) follow-up observations of the identified hierarchical systems to accurately constrain parameters of their inner and outer orbits.

The HD 98800 is a well-known hierarchical quadruple star system, and a member of the 10-Myr old TW Hydrae association (Torres et al. 2008). Located at  $44.9 \pm 4.6$  pc from Earth according to the latest reduction of Hipparcos data<sup>1</sup> (van Leeuwen 2007), corresponding to a parallax of  $22.27 \pm 2.32$  mas, it consists of two pairs of spectro-

---

<sup>1</sup>There is no reliable Gaia eDR3 parallax for HD 98800 (Gaia Collaboration et al. 2016, 2021).

scopic binaries (hereafter, AaAb and BaBb, see Fig 3.1). Both binaries orbit each other with a semi-major axis of  $\approx 45$  au (Tokovinin et al. 2014). The AaAb system is a single-lined spectroscopic binary (SB1) with a period of 262 days (Torres et al. 1995). The mass of the Aa was estimated from pre-main sequence evolutionary models as  $1.1 \pm 0.1 M_{\odot}$  (Prato et al. 2001). The BaBb subsystem is a double-lined spectroscopic binary (SB2) with a period of 315 days, the astrometric orbital solution of this binary was first presented in Boden et al. (2005) using five Keck Interferometer (KI) epochs combined with Hubble Space Telescope astrometry, and available RV observations. From this orbital solution, Boden et al. (2005) estimated a parallax of  $23.7 \pm 2.6$  mas, and dynamical masses for Ba and Bb of  $0.699 \pm 0.064$  and  $0.582 \pm 0.051 M_{\odot}$ , respectively. The BaBb pair also harbours a bright circumbinary protoplanetary disk (Skinner et al. 1992; Zuckerman & Becklin 1993), and ALMA observations revealed that the disk and the binary orbital planes are perpendicular to each other (Kennedy et al. 2019). Numerical simulations suggest that this ‘exotic’ (yet stable) configuration can be reached in some multiple systems, the so-called polar configuration (Verrier & Evans 2008; Farago & Laskar 2010; Aly et al. 2018). Dynamical evolution studies show that an inclined circumbinary disk around a highly eccentric ( $e \gtrsim 0.7$ ) inner binary can evolve towards this configuration (Aly et al. 2015; Zanazzi & Lai 2017; Cuello & Giuppone 2019).

Recently, the orbital characterisation of hierarchical systems hosting disks has provided new insights on the mechanism involved in the formation of multiple systems and their interaction with the disk (Kraus et al. 2020; Czekala et al. 2021). To better understand the source of disk misalignment and the formation process behind hierarchical systems, better information on well-characterised multiple systems’ architectures will be necessary. In that regard, the full characterisation of the HD 98800 quadruple system presents an opportunity to expand the sample of hierarchical systems hosting a protoplanetary disk.

In this work, we present new long-baseline infrared interferometric observations of both AaAb and BaBb subsystems, as well as new RV measurements from original observations and archival reduced spectra. The new interferometric observations resolve the relative position of Ab with respect to Aa for the first time, providing one of the missing keys for the full characterisation of this quadruple system. Additionally, we also present two new astrometric positions for BaBb, allowing us to refine the orbital solution reported in Boden et al. (2005). With the new orbital solutions of AaAb

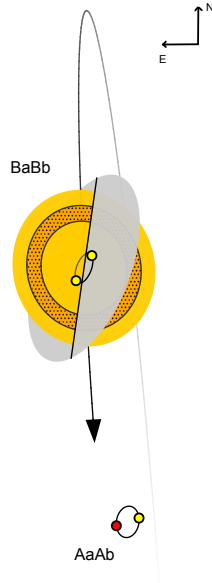


**Figure 3.1:** Schematic view of HD98800 orbital configuration. The BaBb subsystem hosts a circumbinary disk in polar configuration and is orbiting around the AaAb binary in a highly inclined orbit with a semi-major axis of  $\approx 45$  au.

and BaBb, we re-estimated the orbital parameters of the AB outer orbit, evaluate the dynamical stability of this system, and discuss possible formation scenarios for this 2+2 quadruple.

## 3.2 Observations, astrometry, and RV

### 3.2.1 PIONIER observations and data reduction

We used the Very Large Telescope Interferometer (VLTI, Haguenaer et al. 2008; Haubois et al. 2020) with the four-telescope combiner PIONIER in the H band ( $1.5 - 1.8 \mu\text{m}$ , Le Bouquin et al. 2011) to observe the HD98800 quadruple system. Our observations were carried out using the 1.8 m Auxiliary Telescopes with small and medium configurations, providing six projected baselines per configuration ranging from  $\sim 20$  to 100 m. This configuration provides an angular resolution of  $\sim 4$  mas. The estimated interferometric field of view for PIONIER is  $\sim 160$  mas (Hummel et al. 2016), but given the loss of coherence caused by spectral smearing of the companion,

with our given configuration, we have a field of view  $\lesssim 60$  mas (Le Bouquin & Absil 2012; Gallenne et al. 2015).

The first observations of both sub-systems were taken in April and May 2019 as a part of the science verification (SV) campaign<sup>2</sup> of the New Adaptive Optics Module for Interferometry (NAOMI, Woillez et al. 2019). These observations showcase the improvement provided by NAOMI on the sharpness of the point spread function (PSF) (despite  $\sim 1''$  seeing conditions), which led to a better injection of the light in the fibre, and allowed us to mitigate light-contamination effects between A and B subsystems (A-B separation  $\lesssim 0.4''$ ). After the SV run, we obtained six more PIONIER epochs for the AaAb binary between February 2020 and March 2021 (see Table 3.1).

To monitor the instrumental and atmospheric transfer functions, the standard observing procedure is to interleave science and reference stars (CAL-SCI-CAL-SCI-CAL sequence). The calibrators, listed in Table 3.6, were selected using the `SearchCal` software (Bonneau et al. 2006, 2011; Chelli et al. 2016) provided by the Jean-Marie Mariotti Center (JMMC<sup>3</sup>). The data were reduced with the `pndrs` package described in Le Bouquin et al. (2011). The main procedure is to compute squared visibilities ( $V^2$ ) and triple products for each baseline and spectral channel, and to correct for photon and readout noise. The calibrated data are available in the Optical Interferometry DataBase<sup>4</sup>. In Fig. 3.2, an example of the squared visibilities and closure phases (CP) for one of our observations of AaAb is presented.

#### 3.2.2 Determining the AaAb and BaBb astrometry

For each PIONIER observation, we determined the astrometric positions by fitting the  $V^2$  and CP with a binary model using the interferometric tool `CANDID`<sup>5</sup> (Gallenne et al. 2015). For each epoch, the tool delivered the binary parameters, namely the flux ratio ( $f_2/f_1$ ) and the relative astrometric position ( $\Delta\alpha$ ,  $\Delta\delta$ ). `CANDID` can also fit the angular diameter of both components, however, in our case, we kept them fixed at 0.3 mas during the fitting process as the VLTI baselines did not allow us to resolve such small diameters. Briefly, the tool provides a 2D-grid of a multi-parameter fit using a least-squares algorithm (see Fig. 3.3). Given the small separation between AaAb

<sup>2</sup><https://www.eso.org/sci/activities/vltsv/naomisv.html>

<sup>3</sup><https://www.jmmc.fr>

<sup>4</sup><http://oidb.jmmc.fr/index.html>

<sup>5</sup><https://github.com/agallenne/GUIcandid>

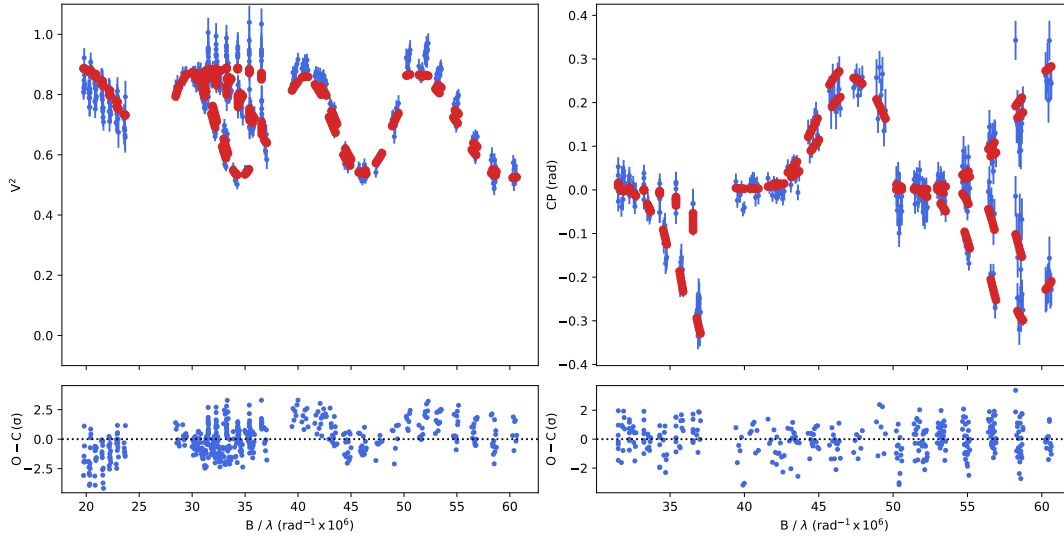


**Figure 3.2:** Squared visibility and closure phase measurements from one observation of AaAb taken in March 2021. The data are in blue, while the red dots represent the best binary model fitted with CANDID for this epoch. The bottom panels show the residuals in the number of sigmas.

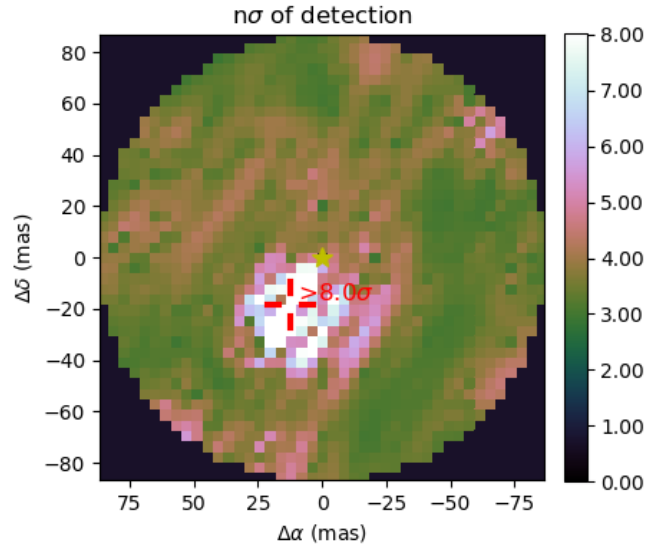


**Figure 3.3:** Detection level map from CANDID for the observation of AaAb taken in April 2019. The colourbar shows the significance of the companion detection in the number of sigmas. The red cross points to the best-fit position.

and BaBb ( $\lesssim 0.4''$ ), we also fitted an additional parameter to take the background cross-contamination into account, the non-coherent light, parametrised in CANDID as

### 3.2. OBSERVATIONS, ASTROMETRY, AND RV

**Table 3.1:** Relative astrometric position of the secondary component, flux ratio, and resolved flux from PIONIER observations. The last two columns correspond to the atmospheric conditions for each epoch: the seeing and coherence time ( $\tau_0$ ), measured by the seeing monitor.

MJD	$\Delta\alpha$ (mas)	$\Delta\delta$ (mas)	$\sigma_{PA}$ ( $^\circ$ )	$\sigma_{maj}$ (mas)	$\sigma_{min}$ (mas)	$f_2/f_1$ (%)	$f_{res}^a$ (%)	Baselines	Seeing (arcsec)	$\tau_0$ (ms)
AaAb										
58601.100162	12.38	-18.35	-13.68	0.02	0.01	$15.2 \pm 0.2$	$8.6 \pm 0.5$	D0-G2-J3-K0	1.05	4.98
58615.047718	15.21	-16.68	-75.72	0.07	0.01	$15.3 \pm 0.2$	$8.9 \pm 0.5$	A0-B2-C1-D0	1.08	5.50
58882.282610	15.80	-16.10	68.64	0.04	0.02	$15.4 \pm 0.1$	$9.1 \pm 0.9$	A0-B2-C1-D0	0.93	4.05
58899.329997	18.34	-13.19	53.01	0.02	0.01	$14.6 \pm 0.3$	$7.2 \pm 1.1$	D0-G2-J3-K0	0.73	6.23
58931.293872	20.32	-5.61	-6.01	0.03	0.02	$13.8 \pm 0.2$	$6.7 \pm 0.3$	D0-G2-J3-K0	0.58	10.01
59282.347290	6.26	14.37	-4.01	0.01	0.01	$14.5 \pm 0.2$	$9.3 \pm 0.7$	D0-G2-J3-K0	0.92	6.19
59292.225719	2.72	14.33	21.17	0.01	0.01	$15.3 \pm 0.3$	$8.7 \pm 0.6$	D0-G2-J3-K0	0.45	5.14
59295.208560	1.50	14.08	66.67	0.01	0.01	$13.8 \pm 0.3$	$8.8 \pm 0.7$	D0-G2-J3-K0	0.81	5.13
BaBb										
58601.106553	16.90	-1.44	-50.59	0.01	0.01	$70 \pm 1$	$12 \pm 1$	D0-G2-J3-K0	1.05	4.98
58615.013389	17.62	-3.40	33.15	0.03	0.01	$65 \pm 1$	$13 \pm 1$	A0-B2-C1-D0	1.08	5.50

**Notes.** <sup>(a)</sup> Parameter to take the background cross-contamination into account (non-coherent light), parametrised in CANDID as a resolved flux.

a resolved flux ( $f_{res}$ ). The final astrometric positions for all epochs of each subsystem are listed in Table 3.1. CANDID estimates the uncertainties using a bootstrapping approach (with replacement) using 10 000 bootstrap samples. For the flux ratio and resolved flux, we used the bootstrap sample distributions and took the median value as the best-fit result and the maximum value between the 16th and 84th percentiles as uncertainty. For the astrometry, the  $1\sigma$  error region of each position is defined with an error ellipse parametrised with the semi-major axis  $\sigma_{maj}$ , the semi-minor axis  $\sigma_{min}$ , and the position angle  $\sigma_{PA}$  measured from north to east. We also quadratically added the systematic uncertainty of 0.35% from the precision of the PIONIER wavelength calibration to  $\sigma_{maj}$  and  $\sigma_{min}$  (Kervella et al. 2017; Gallenne et al. 2018).

### 3.2.3 AB astrometry

We gathered astrometric measurements from the Washington Double Star catalogue (WDS, Mason et al. 2001). The AB pair has been observed since 1909, and observations before 1991 have no reported uncertainties. For those observations, the expected astrometric uncertainty was found to be between  $0.02 - 0.1''$ , depending on the target brightness and observing conditions (Douglass & Worley 1992; Torres et al. 1999).

Since 2009, the pair has been regularly observed with the speckle camera (HRCam, Tokovinin 2018b) mounted on the 4.1 m Southern Astrophysical Research Telescope (SOAR); the last observation presented in this work was obtained in April 2021.

### 3.2.4 CTIO spectroscopy

Five observations were taken with the 1.5 m telescope located at the Cerro Tololo Inter-American Observatory (CTIO) in Chile, and operated by the Small and Moderate Aperture Research Telescopes System (SMARTS) Consortium<sup>6</sup>, from April-July 2021. Observations were made with the CHIRON optical echelle spectrograph (Tokovinin et al. 2013). The RVs were determined from the cross-correlation function (CCF) of echelle orders with the binary mask based on the solar spectrum, as detailed in Tokovinin (2016a). From these observations, we obtained five RV measurements for Aa (brighter component). The Ba and Bb components were totally blended with Aa at two epochs and they could not be separated by a multi-component fit. However, the blending certainly biases the RVs of Aa, increasing the uncertainty of these measurements. In three observations, we were able to obtain reliable RV measurements for Ba and Bb; in one of them, however, the components were still partially blended, so a larger uncertainty was assigned to it.

### 3.2.5 Reduced spectra from public archives

We found nine science-ready datasets in the ESO Phase 3 public archive<sup>7</sup> taken with the Fibre-fed Extended Range Échelle Spectrograph (FEROS/2.2 m, Kaufer et al. 1999). The 1D Phase 3 spectra are given in the barycentric reference frame. One observation was taken in 2015 and the remaining eight were acquired between July and August 2007. The RVs were determined by cross-correlation with the same solar-type binary mask as used in CHIRON. The lines are blended and dominated by the lines of Aa. Consequently, with these FEROS spectra, we obtained only RV measurements for the Aa component, potentially biased by blending with Ba and Bb. Additionally, we found two reduced spectra in the ELODIE public archive<sup>8</sup> at the Observatoire de Haute-Provence (OHP, Moultaika et al. 2004). The observations were taken in 1998, on January

---

<sup>6</sup><http://www.astro.yale.edu/smarts/>

<sup>7</sup><http://archive.eso.org/scienceportal/home>

<sup>8</sup><http://atlas.obs-hp.fr/elodie/>

28 and 29. The spectra are not given in the barycentre reference frame; a correction was therefore applied after retrieving the data. The RVs were determined from the CCF of the spectra with a CORAVEL-type G2 numerical mask using a standalone CCF tool<sup>9</sup> (for further details, see ?). The spectra from ELODIE show partially blended lines and were fitted by three Gaussian components. The RV measurements for BaBb from ELODIE have large uncertainties, but still allowed us to compute the systemic velocity of BaBb at this epoch.

### 3.2.6 Literature data

From the literature, we collected a diverse dataset for this system. The RV measurements of the primary star of AaAb (single-line spectroscopic system, SB1) and both components for BaBb (double-line spectroscopic system, SB2) were taken from Torres et al. (1995), hereafter TO95. For the BaBb binary, we also retrieved interferometric  $V^2$  measurements, obtained with the KI, and published in Boden et al. (2005). Additionally, assuming that the RV of B is the same as the systemic velocity of the disk, we include the disk RV derived from the CO modelling presented in Kennedy et al. (2019), hereafter KE19.

## 3.3 Orbital fitting

We modelled our dataset with the `exoplanet` software package (Foreman-Mackey et al. 2020), which extends the `PyMC3` framework (Salvatier et al. 2016) to support many of the custom functions and distributions required when fitting orbital parameters. Some of the parameters describing the primary or the secondary star orbits around the centre of mass are identical for both components, for example, the period ( $P$ ), eccentricity ( $e$ ), inclination ( $i$ ), and longitude of the ascending node ( $\Omega$ ). But others depend on the component used as a reference, for example, the semi-amplitude of the RV ( $K_{\text{primary}}$  and  $K_{\text{secondary}}$ ) and the argument of the periastron ( $\omega_{\text{primary}} = \omega_{\text{secondary}} + \pi$ ). In an astrometric-only orbital fitting, it is common practice to report  $\omega = \omega_{\text{secondary}}$ , whereas with an RV orbit it is generally common practice to report  $\omega = \omega_{\text{primary}}$ . Then, in a joint astrometric-RV orbit, there could be ambiguity regarding the convention used for  $\omega$ . We adopted the orbital convention

<sup>9</sup>[https://github.com/szunigaf/CCF\\_functions](https://github.com/szunigaf/CCF_functions)

from *exoplanet*<sup>10</sup>, where the argument of periastron  $\omega$  is reported with respect to the primary star, and the longitude of the ascending node  $\Omega$  is the node where the secondary is moving away from the observer (see Fig. 3.4).

Given that BaBb is an SB2, the orbital fitting procedure is slightly different compared to the AaAb subsystem (SB1). The different steps for each orbital fitting are explained below. The Markov chain Monte Carlo (MCMC) samples and PyMC3 models corresponding to both subsystems are available online<sup>11</sup>. The prior distributions and corner plots from the orbital parameters' posterior samples are displayed in Appendix 3.7.2.

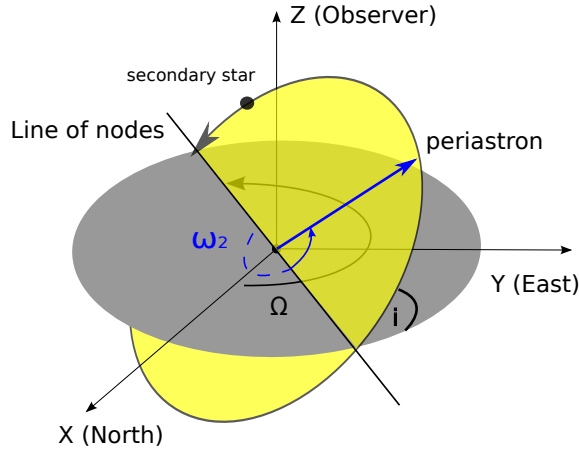


**Figure 3.4:** Diagram of the orbit of the secondary star around the centre of mass (yellow plane) and the reference plane (grey). This diagram follows the orbital convention of *exoplanet*.

### 3.3.1 BaBb orbit

Given that BaBb is an SB2, we can fit the astrometric points from PIONIER together with the RV amplitude of each component,  $K_{Ba}$  for the primary and  $K_{Bb}$  for the secondary, as well as the systemic velocity  $\gamma_B$ . Additionally, we extended *exoplanet* to include the  $V^2$  model for individually unresolved components in a binary system. Briefly, the fringe contrast  $V^2$  of a binary system depends on the properties of the

<sup>10</sup><https://docs.exoplanet.codes/en/latest>

<sup>11</sup><https://github.com/szunigaf/HD98800>

individual components and the binary separation (Berger & Segransan 2007),

$$V_{\text{binary}}^2 = \frac{1 + \left(\frac{f_2}{f_1}\right)^2 + 2 \left(\frac{f_2}{f_1}\right) \cos\left(\frac{2\pi C (u \Delta\alpha + v \Delta\delta)}{\lambda}\right)}{\left(1 + \frac{f_2}{f_1}\right)^2}, \quad (3.1)$$

where  $\Delta\alpha$  and  $\Delta\delta$  are the relative separation in right ascension and declination, respectively (from the exoplanet model),  $u$  and  $v$  are the projected baselines (in meters),  $f_2/f_1$  is the flux ratio, and  $\lambda$  is the wavelength. The parameter  $C$  is a conversion factor so that the astrometry is in arcsec and the wavelength in  $\mu\text{m}$ . The  $V^2$  measurements from KI were then included in the fitting process, where the flux ratio  $f_2/f_1$  was fitted as a free parameter along with the other orbital parameters (see Table 3.2).

All the orbital parameters were estimated from the posterior distributions, taking the median values as the best-fit results and the maximum values between the 16th and 84th percentile as uncertainties. From these distributions, we could then calculate the distribution of the masses for both components as well as the distance to the system using the following equations (Torres et al. 2010; Gallenne et al. 2019):

$$M_{Ba} = \frac{1.036149 \times 10^{-7} (K_{Ba} + K_{Bb})^2 K_{Bb} P (1 - e^2)^{3/2}}{\sin^3 i}, \quad (3.2)$$

$$M_{Bb} = \frac{1.036149 \times 10^{-7} (K_{Ba} + K_{Bb})^2 K_{Ba} P (1 - e^2)^{3/2}}{\sin^3 i}, \quad (3.3)$$

$$a_{\text{au}} = \frac{9.191940 \times 10^{-5} (K_{Ba} + K_{Bb}) P \sqrt{1 - e^2}}{\sin i}, \quad (3.4)$$

$$\pi = \frac{a}{a_{\text{AU}}}, \quad (3.5)$$

where  $M_{Ba}$  and  $M_{Bb}$  correspond to the masses of the primary and the secondary stars, respectively, expressed in solar mass,  $P$  is the period in days,  $K_{Ba}$  and  $K_{Bb}$  are the RV semi-amplitudes of the primary and secondary star in  $\text{km s}^{-1}$ , respectively, and  $a$  is the angular semi-major axis in arcseconds. The parameter  $a_{\text{au}}$  is the semi-major axis expressed in astronomical units. Table 3.2 lists a full description of the inferred orbital parameters. Fig. 3.5 shows the best-fit RV curve. Fig. 3.6 shows the best-fit visual orbit; the black dots are the phase coverage of the KI observations, that is the astrometric positions from the best-fit orbit corresponding to the observation date of each  $V^2$  dataset (see Fig. 3.13). Some parameters seem incompatible with the previous result taking the uncertainties into account; this may be due to the fact that some of the uncertainties could have been underestimated.

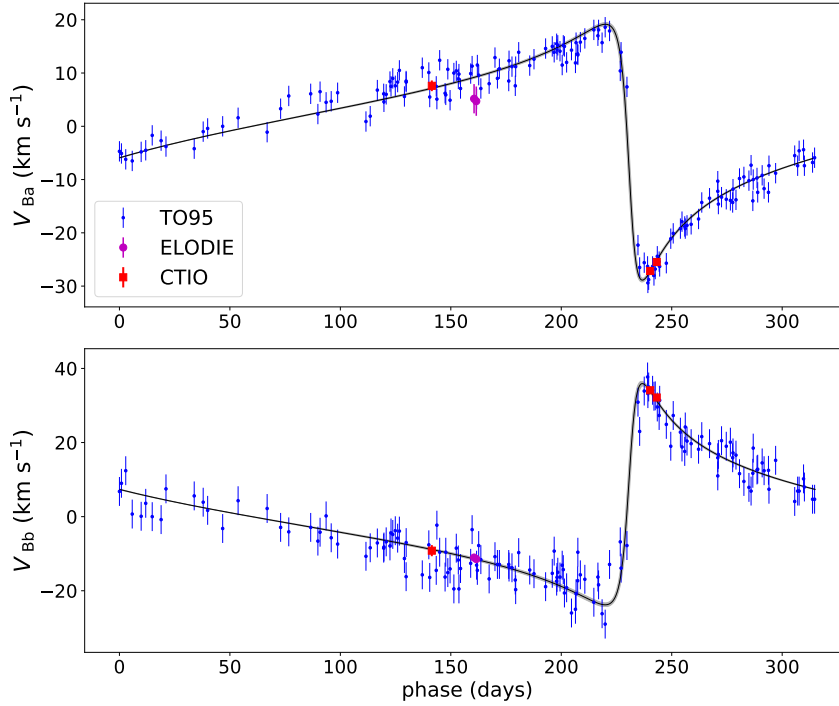


**Figure 3.5:** Phase-folded RVs orbit for BaBb. The systemic velocity  $\gamma$  for each set of observations was subtracted. The solid line corresponds to the best-fit model. The upper panel plots the RVs of Ba, and the lower panel corresponds to Bb.

### 3.3.2 AaAb orbit

This subsystem is an SB1, therefore it is not possible to break the degeneracy between the parallax and the semi-major axis and determine individual stellar masses. The orbit is based on the astrometric points from PIONIER and on the RVs of the primary star Aa. Consequently, we only fitted the RV semi-amplitude of the Aa component of the system  $K_{Aa}$ , and the systemic velocity  $\gamma_A$ . To estimate the masses of the individual components of an SB1, we must assume a distance. We tested two parallax values, the one obtained from the orbital fitting of BaBb and the Hipparcos one (van Leeuwen 2007), as there is currently no reliable Gaia parallax for the system. In our MCMC model, we included these parallax values as a prior using a normal distribution ( $22.27 \pm 2.31$  mas and  $22.0 \pm 0.6$  for the Hipparcos one and the one based from the orbital solution of BaBb, respectively). The parallax is then a free parameter in our orbital fitting using the abovementioned priors. Using Kepler’s third law and

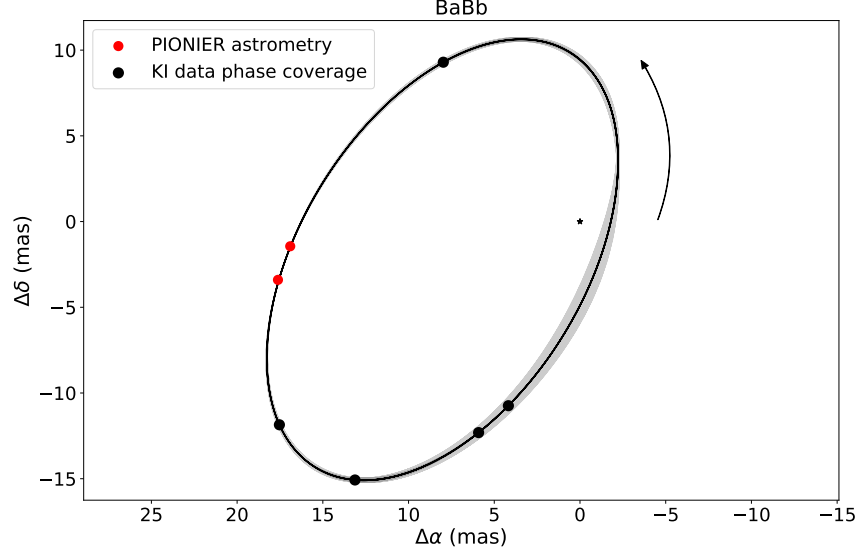


**Figure 3.6:** Best orbital solution for BaBb. The solid line corresponds to the best-fit model and the shaded area to the  $1\sigma$  region. The primary star Ba is located at the origin. The relative positions of Bb are plotted as filled dots. The error ellipses from PIONIER astrometry are smaller than the markers.

combining equations (3.3) and (3.4), we calculated

$$M_{tot} = \frac{a_{AU}^3}{P_{years}^2}, \quad (3.6)$$

$$M_{Ab} = \frac{1.036149 \times 10^{-7} K_{Aa} \sqrt{1 - e^2} a_{AU}^2}{(9.191940 \times 10^{-5})^2 P \sin i}, \quad (3.7)$$

$$M_{Aa} = M_{tot} - M_{Ab}, \quad (3.8)$$

where  $M_{tot}$ ,  $M_{Aa}$ , and  $M_{Ab}$  correspond to the total mass, and the primary and secondary star masses, respectively, expressed in solar mass,  $P_{years}$  the period in years,  $P$  the period in days,  $K_{Aa}$  the RV semi-amplitude of the primary star in  $\text{km s}^{-1}$ , and  $a_{AU}$  the semi-major axis expressed in astronomical units.

The posterior distributions for the masses and parallaxes, assuming different initial priors for the parallaxes are shown in Fig. 3.7 in blue and red, respectively. The orbital parameters converge and have the same results for both cases, only the physical parameters that are dependent on the distance are affected by the choice of the prior distribution for the parallax (i.e.  $M_{Aa}$ ,  $M_{Ab}$ , and  $a_{AU}$ ).

All the orbital parameters were estimated from the posterior distributions taking the median values as the best-fit results and the maximum values between the 16th

**Table 3.2:** Orbital parameters for the HD 98800 BaBb binary.

Orbital parameters	Boden et al. (2005)	This work
Period (days)	$314.327 \pm 0.028$	$314.86 \pm 0.02$
$T_0$ (MJD)	$52481.34 \pm 0.22$	$48707.5 \pm 0.2$
$e$	$0.7849 \pm 0.0053$	$0.805 \pm 0.005$
$\omega_{Ba}$ ( $^\circ$ )	$109.6 \pm 1.1$	$104.5 \pm 0.3$
$\Omega$ ( $^\circ$ )	$337.6 \pm 2.4$	$342.7 \pm 0.4$
$i$ ( $^\circ$ )	$66.8 \pm 3.2$	$66.3 \pm 0.5$
$a$ (mas)	$23.3 \pm 2.5$	$22.2 \pm 0.4$
$K_{Ba}$ ( $\text{km s}^{-1}$ )	$22.94 \pm 0.34$	$24.0 \pm 0.3$
$K_{Bb}$ ( $\text{km s}^{-1}$ )	$27.53 \pm 0.61$	$29.9 \pm 0.6$
$\gamma_{\text{TO95}}$ ( $\text{km s}^{-1}$ )	$5.73 \pm 0.14$	$5.6 \pm 0.1$
$\gamma_{\text{ELODIE}}$ ( $\text{km s}^{-1}$ )	...	$3.4 \pm 0.7$
$\gamma_{\text{CTIO}}$ ( $\text{km s}^{-1}$ )	...	$6.4 \pm 0.4$
$f_2/f_1$ (K band)	$0.612 \pm 0.046$	$0.76 \pm 0.08$
Derived parameters		
$\pi$ (mas)	$23.7 \pm 2.6$	$22.0 \pm 0.6$
$M_{Ba}$ ( $M_\odot$ )	$0.70 \pm 0.06$	$0.77 \pm 0.04$
$M_{Bb}$ ( $M_\odot$ )	$0.58 \pm 0.05$	$0.62 \pm 0.02$
$d$ (pc)	$42.2 \pm 4.7$	$45 \pm 1$
$a$ (AU)	$1.0 \pm 0.2$	$1.01 \pm 0.01$

and 84th percentile as uncertainties (see Table 3.3). Fig. 3.8 shows the best-fit binary orbit (identical in the plane of the sky for both parallax scenarios). In the rest of the paper, we assume the masses of AaAb as derived with the parallax obtained from the BaBb best orbital fit.

### 3.3.3 Outer orbit A-B

Using our orbital solutions of the inner binaries of the system, we recalculated the orbital parameters of AB. We assume that the systemic velocities of AaAb and BaBb from Torres et al. (1995), FEROS, CHIRON, and ELODIE observations in our orbital fitting

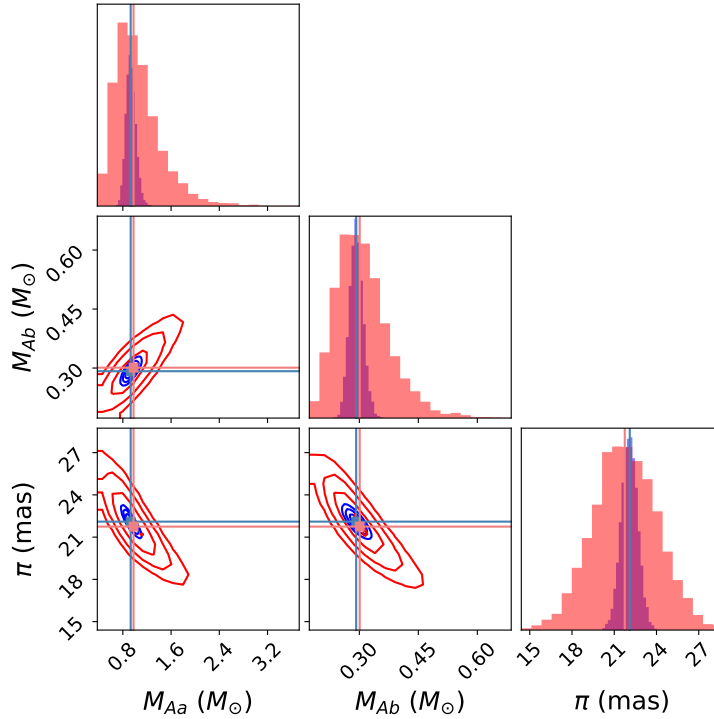


**Figure 3.7:** Posterior distribution of masses and parallax of AaAb subsystem assuming the Hipparcos value (red) and the solution from BaBb fitting (blue) as a prior distribution of the parallax in our MCMC model. The red and blue lines highlight the median of each distribution.

results, and the one from CO modelling by Kennedy et al. (2019) (KE19), correspond to the centre-of-mass RVs of A and B in the outer orbit (see Table 3.9). We jointly fitted the astrometric position with the RV measurements of AB. In our MCMC model, we included the parallax and the masses obtained from the inner orbits' results as priors. For consistency, we used the AaAb masses derived from the parallax obtained from the orbital fitting of BaBb. The normal distribution priors for the masses and parallax are  $M_A : 1.22 \pm 0.5 M_\odot$ ,  $M_B : 1.38 \pm 0.5 M_\odot$ , and  $\pi : 22.0 \pm 0.6$  mas, respectively. The  $\gamma_{AB}$  was included as a free parameter, with a uniform prior between 0 and  $20 \text{ km s}^{-1}$ . Given that the visual micrometric measurements made before 1991 have unknown uncertainties, we defined the large ( $\sigma \sim 0.1''$ ) and the small ( $\sigma \sim 0.02''$ ) uncertainty cases for these measurements (solutions I and II in Table 3.4), according to the typical range of errors reported in the astrometry measurements by USNO (Douglass & Worley 1992; Torres et al. 1999).

**Table 3.3:** Orbital parameters for HD 98800 AaAb binary.

Orbital parameters	Torres et al. (1995)	This work
Period (days)	$262.15 \pm 0.51$	$264.51 \pm 0.02$
$T_0$ (MJD)	$48737.1 \pm 1.6$	$48742.5 \pm 0.8$
$e$	$0.484 \pm 0.020$	$0.4808 \pm 0.0008$
$\omega_{Aa}$ ( $^\circ$ )	$64.4 \pm 2.1$	$68.7 \pm 0.1$
$\Omega$ ( $^\circ$ )	...	$170.2 \pm 0.1$
$i$ ( $^\circ$ )	...	$135.6 \pm 0.1$
$a$ (mas)	...	$19.03 \pm 0.01$
$K_{Aa}$ ( $\text{km s}^{-1}$ )	$6.8 \pm 0.2$	$6.7 \pm 0.2$
$\gamma_{\text{TO95}}$ ( $\text{km s}^{-1}$ )	$12.7 \pm 0.1$	$12.8 \pm 0.1$
$\gamma_{\text{FEROS07}^a}$ ( $\text{km s}^{-1}$ )	...	$14.7 \pm 0.4$
$\gamma_{\text{FEROS15}^b}$ ( $\text{km s}^{-1}$ )	...	$12 \pm 2$
$\gamma_{\text{CTIO}}$ ( $\text{km s}^{-1}$ )	...	$11.8 \pm 0.2$
$\gamma_{\text{ELODIE}}$ ( $\text{km s}^{-1}$ )	...	$12.1 \pm 0.5$
Derived parameters		
Hipp. $\pi$ (mas)	...	$22 \pm 2$
$M_{Aa}$ ( $M_\odot$ )	...	$0.9 \pm 0.4$
$M_{Ab}$ ( $M_\odot$ )	...	$0.29 \pm 0.07$
$a$ (AU)	...	$0.9 \pm 0.1$
BaBb $\pi$ (mas)	...	$22.0 \pm 0.6$
$M_{Aa}$ ( $M_\odot$ )	...	$0.93 \pm 0.09$
$M_{Ab}$ ( $M_\odot$ )	...	$0.29 \pm 0.02$
$a$ (AU)	...	$0.86 \pm 0.02$

**Notes.** <sup>(a)</sup> Systemic velocity of FEROS observations taken in 2007. <sup>(b)</sup> Same as (a), but for the FEROS observation taken in 2015.

All the orbital parameters were estimated from the posterior distributions, taking the median values as the best-fit results and the maximum values between the 16th and 84th percentile as uncertainties (see Table 3.4). The best-fit orbits for solutions I and II are shown in Fig. 3.9, which are in good agreement with the astrometric

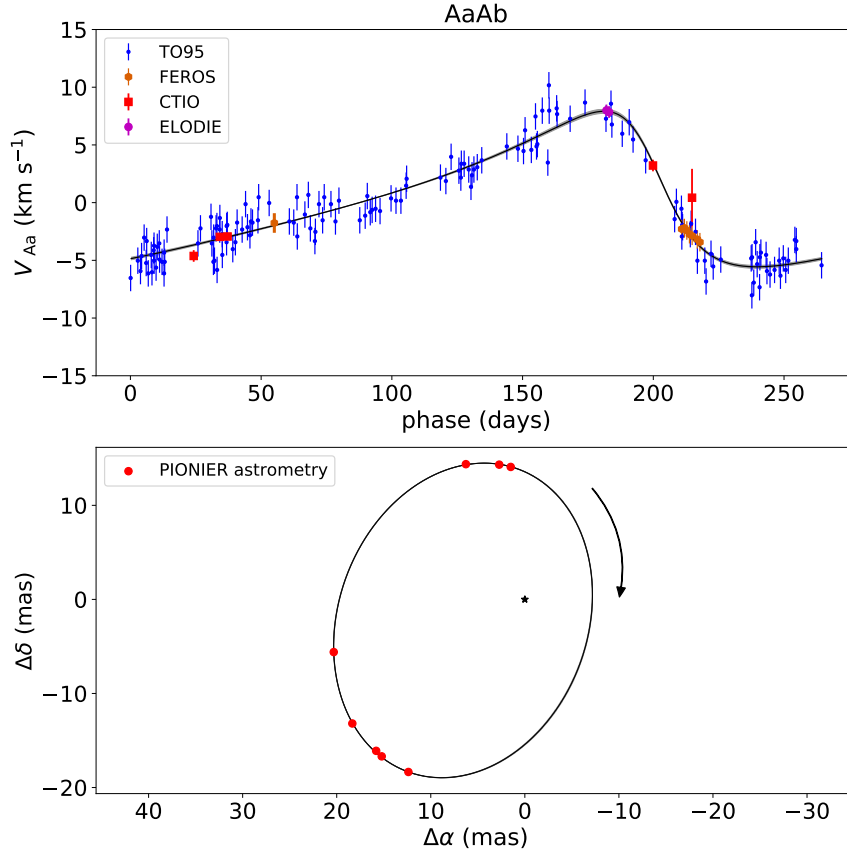


**Figure 3.8:** Best orbital solution for AaAb. In both panels, the solid line corresponds to the best-fit model. *Bottom panel:* The primary star Aa is located at the origin. The relative positions of Ab are plotted as filled dots; the error ellipses from PIONIER astrometry are smaller than the marker. *Upper panel:* The coloured markers correspond to the primary star RV measurements. The systematic velocity  $\gamma$  for each set of observations was subtracted.

measurements. We show the phase-folded RV best-fit orbit in Fig. 3.10; the narrow 1-sigma region in this figure mainly comes from the constraints imposed by the AB masses and parallax prior distributions. There are likely small instrumental zero-point offsets among the data sets that were used to determine the systemic velocity variation, which are difficult to determine and could bias the outer orbit solution. As a reminder, all these results rely on the masses and parallax estimated in the orbital fitting of the inner subsystems. The parallax and masses derived from BaBb RV semi-amplitudes ( $K_{Ba}$  and  $K_{Bb}$ ) are proportional to  $K^2$  and  $K^3$ , respectively. Thus, a small systematic error in  $K_{Ba}$  or  $K_{Bb}$  can bias the masses and parallax results substantially. The RV amplitudes may be biased, especially for the weakest lines of Bb. Therefore,

the masses and the parallax of the BaBb pair that mainly rely on the RVs by Torres et al. (1995) should be considered with caution. A small change in the method of splitting the blended spectra can lead to different masses. The posterior samples of the orbital parameters and all prior distributions used in the MCMC model are available in Appendix 3.7.2.

Accurate astrometry of AB reveals a wavy motion caused by the subsystems (wobble); its amplitude gives an independent constraint on the inner mass ratios. Neglecting the smaller wobble of BaBb, we modelled the astrometry of AB by a combination of two Keplerian orbits, with the orbital parameters of AaAb fixed to the values determined above. A simple least-squares fit yielded the AB orbital parameters similar to solution I, for example  $P = 233 \pm 41$  yr. The ratio of the wobble amplitude to the semi-major axis of AaAb was found to be  $f = 0.18 \pm 0.04$ . Neglecting the influence of the faint light of Ab on the photo-centre of A, this factor gives the inner mass ratio  $q = f/(1 - f) = 0.22$ , compatible within errors with the mass ratio of 0.31 estimated above from the orbit of AaAb.

### 3.4 Short- and long-term future of the quadruple system

Several studies investigated the stability of the system over time (e.g. Verrier & Evans 2008; Kennedy et al. 2019), but those studies mostly focused on the stability of the disk around BaBb and less about the evolution of the quadruple system itself. In this section we intend to study both the short- and long-term dynamical evolution of the two pairs of binary systems. Using the new (or revised) orbits obtained for AaAb, BaBb, and AB, we first quantify the dynamical stability over time of the four stars, and second make preliminary predictions for the transit of BaBb and its disk in front of AaAb. To make such predictions, we use the N-body code REBOUND<sup>12</sup> (Rein & Liu 2012). For the simulations, we used the orbital solutions for AaAb and BaBb listed in Tables 3.3 and 3.2, and we tested both solutions I and II for the orbit of AB (Table 3.4). The best-fit parameters are directly taken from the posterior distributions, as their median values.

---

<sup>12</sup>Available at <https://github.com/hannorein/rebound>

### 3.4. SHORT- AND LONG-TERM FUTURE OF THE QUADRUPLE SYSTEM

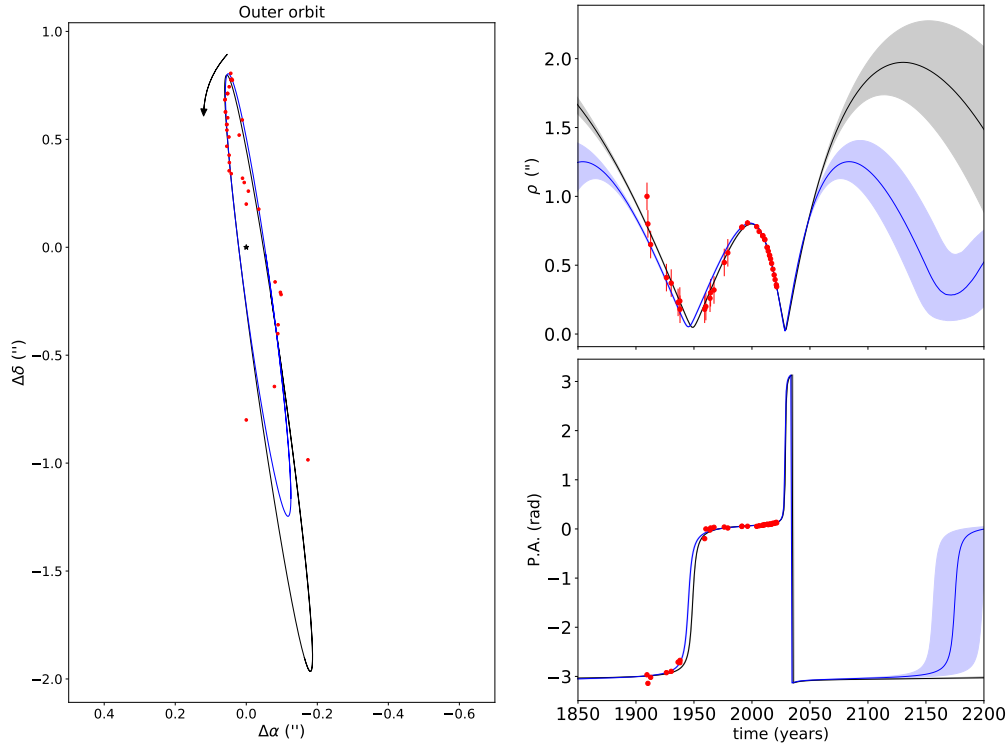


**Figure 3.9:** Best orbital solution for AB outer orbit for both uncertainty assumptions in the astrometry before 1991. The solid black line corresponds to the best orbital solution assuming small uncertainties ( $\sigma \sim 0.02''$ ) and the blue one assumes large uncertainties ( $\sigma \sim 0.1''$ ). *Left:* The red dots correspond to the astrometric measurements as seen in the plane of the sky. *Right:* The red dots corresponds to the astrometric measurements expressed in separation (upper sub-panel) and position angle (bottom sub-panel). The error bars shown in the astrometry before 1991 correspond to the large uncertainty case. The shaded area corresponds to the orbital solutions'  $1\sigma$  region.

#### 3.4.1 Dynamical stability

For our dynamical stability analysis, we use the ‘mean exponential growth of nearby orbits’ (MEGNO) criterion implemented in the REBOUND package. As discussed in Hinse et al. (2010), the MEGNO factor, first introduced in Cincotta & Simó (2000), provides an estimate of how ordered or chaotic a system is. The MEGNO factor is the integral of variational vectors for a given integration time and a given set of parameters. It is therefore necessary to sample different timescales as the MEGNO is expected to vary over time (and converge to a value of 2 for a stable system), tracing the different orbital timescales. In our case, we want to study the stability of the orbits by changing the masses of Aa and Ab. To do so, we computed the MEGNO value

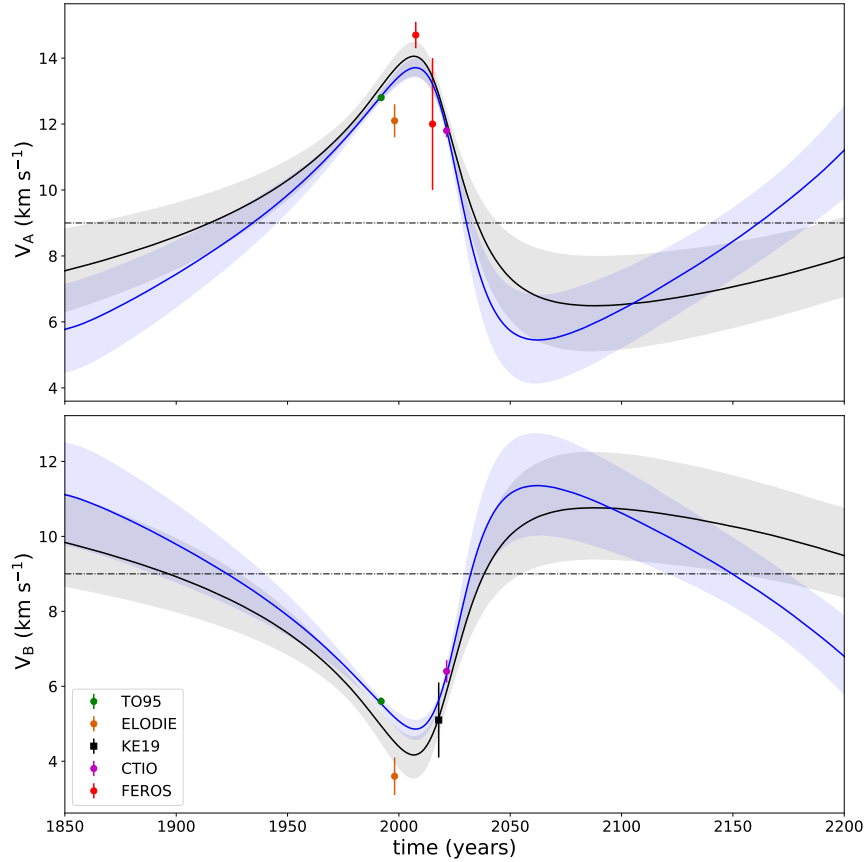


**Figure 3.10:** Best orbital solution for AB outer orbit for both uncertainty assumptions in the astrometry before 1991. In both panels the solid line corresponds to the best fit model and the shaded area to the  $1\sigma$  region. The solid black lines correspond to the best orbital solution assuming small uncertainties ( $\sigma \sim 0.02''$ ) and the blue ones assume large uncertainties ( $\sigma \sim 0.1''$ ). The dots markers correspond to the RV measurement of systemic velocities from our orbital solutions and the one obtained from CO modelling.

for a matrix of masses, the rows of the matrix consist of 12 linearly spaced masses for  $M_{Aa}$  in the range  $[0.5, 1.5] M_{\odot}$  and 10 linearly spaced masses for  $M_{Ab}$  in the range  $[0.1, 1.0] M_{\odot}$ .

To setup the simulation, we sequentially added Aa and Ab, and then included a third particle representing BaBb as a single star. We then integrated the motion of all stars forward in time, using the IAS15 integrator (Rein & Spiegel 2015). Since it is necessary to capture the different timescales for the evolution of the system, we used several integration times, in years: 1 000, 2 000, 5 000, 10 000, 20 000, 50 000, 100 000, 250 000, 500 000, and 1 000 000. For all the simulations, none of the stars escaped the

### 3.4. SHORT- AND LONG-TERM FUTURE OF THE QUADRUPLE SYSTEM

**Table 3.4:** Orbital parameter for HD 98800 AB system.

Fitted parameters	This work		
	KE19	Solution I <sup>a</sup>	Solution II <sup>b</sup>
Period (years)	246 ± 10	230 ± 20	340 ± 50
T <sub>0</sub> (years)	2023.0 ± 0.5	2023 ± 1	2018 ± 1
<i>e</i>	0.517 ± 0.007	0.46 ± 0.02	0.55 ± 0.04
$\omega_A$ (°)	63 ± 2	65 ± 5	44 ± 4
$\Omega$ (°)	184.6 ± 0.2	184.5 ± 0.1	184.6 ± 0.1
<i>i</i> (°)	88.6 ± 0.1	88.1 ± 0.1	88.39 ± 0.09
$\gamma_{AB}$ (km s <sup>-1</sup> )	...	8.7 ± 0.7	8.7 ± 0.9
$M_A$ (M <sub>⊙</sub> )	1.3 ± 0.1	1.1 ± 0.3	1.2 ± 0.4
$M_B$ (M <sub>⊙</sub> )	[1.28]	1.4 ± 0.3	1.4 ± 0.4
$\pi$ (mas)	[22.2]	22.2 ± 0.5	22.5 ± 0.6
Derived parameters			
$K_A$ (km s <sup>-1</sup> )	...	4.2 ± 0.8	3.8 ± 0.9
$K_B$ (km s <sup>-1</sup> )	...	3.2 ± 0.8	3 ± 1
<i>a</i> (″)	1.2 ± 0.03	1.13 ± 0.08	1.5 ± 0.2
<i>a</i> (AU)	...	51 ± 3	67 ± 8
<i>d</i> (pc)	...	45 ± 1	44 ± 1

**Notes.** KE19: Kennedy et al. (2019). <sup>(a)</sup> Assuming large uncertainties in astrometry before 1991. <sup>(b)</sup> Assuming small uncertainties in astrometry before 1991.

system, suggesting that it is stable over thousands of AB orbits. Since the final matrices all are homogeneous, in Figure 3.11 we show the mean MEGNO value (over the 12 × 10 matrix) as a function of the integration time, for both solutions I and II, and we computed the standard deviation as the uncertainties. The stability criterion displays an exponential decay, converging towards a value of 2 (Hinse et al. 2010), therefore indicating that the system should be stable over a long period of time, regardless of the uncertainties on the AB orbital parameters. In the exercise above, we treated BaBb as a single star, and it might be worth re-visiting the stability of the system when

considering all four stars, but given the large uncertainties on the AB orbit, this is out of the scope of this study.

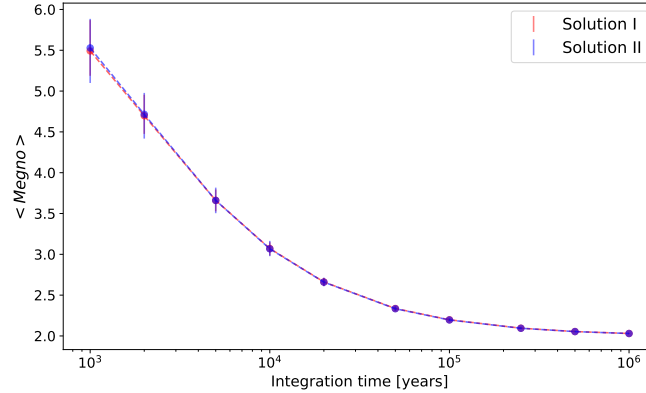


**Figure 3.11:** Mean MEGNO value for the 12x10 matrix for different integration times. Error bars correspond to  $1\sigma$ .

### 3.4.2 The transit of the disk in front of AaAb

The orbital parameters of AB strongly suggest that the BaBb pair and its disk will pass in front of the AaAb system (Kennedy et al. 2019), starting sometime in 2026 (depending on the solution used for AB). This presents a unique opportunity to observe and characterise the properties of the dust and gas disk via photometric (and spectroscopic) monitoring of the whole system. In virtue of this possible occultation, we investigate how the photometric light curve might look, including the four stars in the simulation to account for possible interactions between the two binary systems (in App.3.7.3 we provide a more detailed explanation on how the simulation is initialised).

To make the predictions for the transit, the starting time of the simulation was set to 2015.17. The choice of the starting date does not matter as we are using the orbital solutions determined in this paper. We integrated the simulation over 18 years and saved 10 000 intermediate steps (one every  $\sim 0.7$  days), saving the positions of the four stars in the reference system centred at the centre of mass of BaBb. The integration was done using the IAS15 integrator, but we also compared our results with the WHfast integrator (Rein & Tamayo 2015) with a timestep of 0.011 days, and found no significant differences between the two simulations. Additionally, saving more intermediate steps does not lead to a significant improvement of the resolution of the

### 3.4. SHORT- AND LONG-TERM FUTURE OF THE QUADRUPLE SYSTEM

simulated light curve.

With the  $(x, y)$  positions of Aa and Ab, on the plane of the sky, we then estimated if they overlap with the position of the disk, which is centred at the centre of mass of the B system (Fig. 3.18). We used the parameters reported in Kennedy et al. (2019), namely, the inner and outer radii (2.5 and 4.6 au, respectively), eccentricity (0.03), position angle ( $15.6^\circ$ ), inclination ( $26^\circ$ ), and argument of periapsis ( $-73^\circ$ ). To estimate the extinction caused by the circumbinary disk, we first needed the flux ratio between Aa and Ab, and an analytical form for the integrated vertical optical depth of the disk. For the flux ratio, we used the results from the modelling of the PIONIER observations, and the normalised fluxes are  $F_{Aa} = 0.87$  and  $F_{Ab} = 0.13$  in the H band. For the vertical optical depth, it is parametrised as  $\tau(r) = 0.5 \times r_0/r$ , where  $r_0$  is the inner radius of the disk ( $\tau(r) = 0$  inside and outside the disk). Before applying the extinction law, we first needed to estimate the distance  $r$  in the midplane of the disk, accounting for projection and rotation effects. We therefore defined a rotation matrix  $\mathcal{R}$  based on the inclination, argument of periapsis, and position angle of the disk, and de-projected the on-sky  $(x, y)$  positions of the disk and Aa and Ab stars. The normalised flux at each time-step is then  $F_{Aa}e^{-\tau(r_{Aa})} + F_{Ab}e^{-\tau(r_{Ab})}$  (the contribution of BaBb is neglected here, but since the vertical optical depth of the disk remains unknown the absolute depth of the transit cannot be constrained).

We then simulated 1 000 transits and their respective light curves by modifying the AB orbital parameters (for both solutions I and II), the parallax, and all four masses randomly drawing 1 000 realisations from the MCMC fitting of the AB orbit. This ensures that the correlations between the different parameters are preserved (to avoid, for instance, a small semi-major axis and large stellar masses that would lead to a much shorter orbital period). Finally, from these 1 000 light curves, we estimated a probability distribution of the normalised flux as a function of time, which is shown in Fig. 3.12, where the transit light curve for the best-fit solution is shown in orange. The figure shows that the transit should be well constrained in time, and we predict it to start in 2026, going out and passing through the inner regions (devoid of dust) before re-entering behind the northern side of the disk. Our simulations suggest that the transit event should finish sometime between 2030 and 2031. The best-fit solution shows the complex structure of the light curve as one of the stars is sometimes not occulted by the disk. Comparing the light curves for both solutions I and II, we note that transit starts earlier for solution I, but both cases show a similar behaviour. Over-

all, regular photometric monitoring of the quadruple system between 2026 and 2031 at different wavelengths would put unique constraints on the vertical optical depth of the circumbinary disk around BaBb, offering the opportunity to directly measure the surface density of the dust and to possibly derive constraints on the typical size of the dust particles.

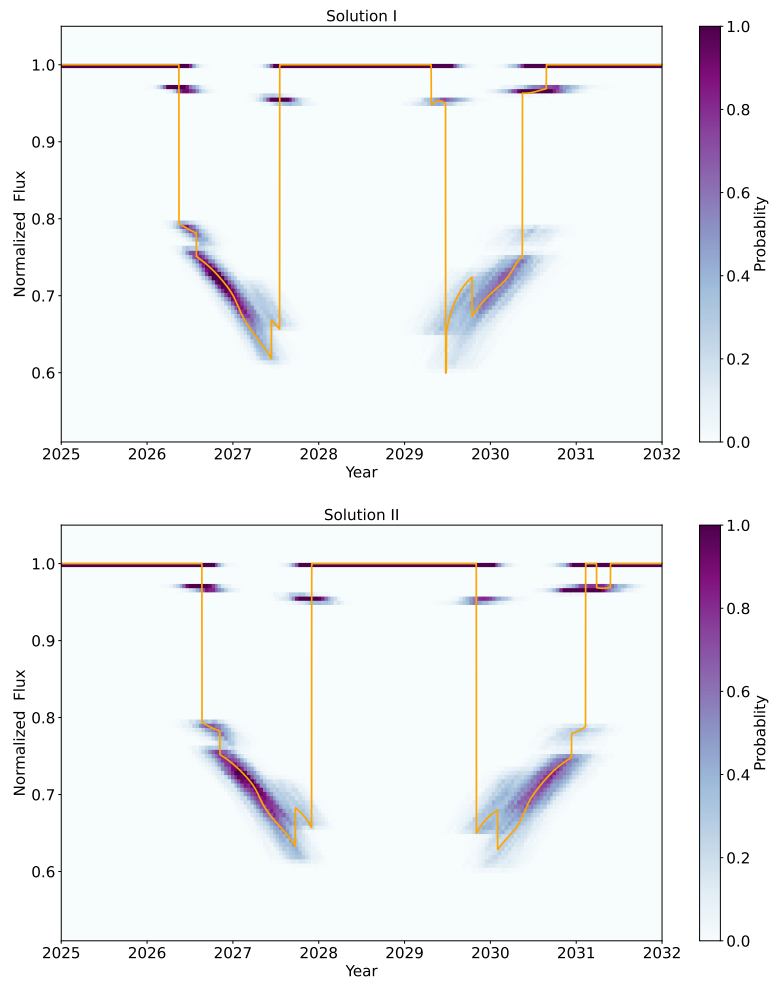


**Figure 3.12:** Probability density plot of 1000 realizations of the light curve for the occultation of AaAb behind the disk surrounding BaBb for solutions I and II (top and bottom, respectively). The colour bar shows the probability of getting a determined flux at a given time, such that the sum along each of the columns is normalised to unity. In orange we show the light curve for the best-fit parameters (Table 3.4).

## 3.5 Discussion

Here we discuss the implications of our results in the context of the formation of this quadruple system and its influence on the disk evolution. A further dynamical simulation of this system is beyond the scope of this paper.

### 3.5.1 Comparisons with previous results

We refined the orbital results from Boden et al. (2005) and resolved the orbit of the AaAb subsystem for the first time using PIONIER observations (see Table 3.2 and 3.3). Using our orbital solution of BaBb, we derived a dynamical parallax of  $22.0 \pm 0.6$  mas corresponding to a distance of  $45 \pm 1$  pc. Boden et al. (2005) placed the system at  $42.2 \pm 4.7$  pc using their orbital solution, and the updated reduction of the Hipparcos data (van Leeuwen 2007) measured a parallax of  $22 \pm 2$  mas, corresponding to a distance of  $45 \pm 5$  pc likely biased by the unresolved A-B components. There are two entries at the Gaia EDR3 catalogue (Gaia Collaboration et al. 2021) at  $\sim 0.1''$  and  $\sim 0.3''$  from the positions of AaAb and BaBb, respectively, corresponding to the angular distance after correction using Gaia EDR3 proper motion from J2000 to J2016. Additionally, both subsystems were identified in the cross-matched catalogue between Gaia EDR3 and the Tycho-2 merged with the TDSC (I/350/tyc2tdsc, Marrese et al. 2021). The parallax values from Gaia EDR3 are  $20.1 \pm 0.3$  mas and  $23.7 \pm 0.4$  mas for BaBb and AaAb, respectively. However, both measurements have a large re-normalised unit weight error (RUWE) value (Lindgren et al. 2018) and then are considered unreliable. The RUWE value is expected to be around 1.0 for a good fit to the astrometric observations, while in this case it is  $\sim 9$  and  $\sim 6$  for AaAb and BaBb, respectively, meaning that in both cases the unresolved companions produce motion in the photo-centre, so the 5-parameter Gaia astrometric model performs poorly. The distance inferred with our new results remains consistent with Boden et al. (2005) within  $2.3\sigma$  and is compatible with the Hipparcos value. Using the new distance of BaBb and the orbital solution of AaAb, we derived, for the first time, the dynamical masses of the AaAb binary as  $M_{Aa} = 0.93 \pm 0.09 M_{\odot}$  and  $M_{Ab} = 0.29 \pm 0.02 M_{\odot}$ . Using the Baraffe et al. (2015) 10 Myr isochrones and the dynamical masses of AaAb, we estimated an H-band flux ratio of 15.85% and 15.06% for solar and sub-solar ( $[M/H] = -0.5$ ) metallicity, respectively (see Appendix 3.7.4). These flux ratio values are compatible with the flux ratio derived with our PIONIER observations ( $\sim 14\%$ , see Table 3.1).

Prato et al. (2001) compared the stellar properties derived from near- and mid-infrared diffraction-limited imaging with pre-main sequence evolutionary tracks, yielding masses of  $M_{Aa} = 1.1 \pm 0.1 M_{\odot}$ ,  $M_{Ba} = 0.93 \pm 0.08 M_{\odot}$ , and  $M_{Bb} = 0.64 \pm 0.1 M_{\odot}$  and an age of  $\sim 10$  Myr. These values are compatible with the dynamical masses derived in this paper within  $\sim 1.5\sigma$ . On the other hand, the SED models presented in Boden et al. (2005) suggested stellar properties compatible with the ones published in Prato et al. (2001). However, the predicted masses from evolutionary tracks were significantly higher than the dynamical masses from Boden et al. (2005). The authors claimed that this discrepancy came from the assumption of solar abundances in the evolutionary models, proposing sub-solar abundances ( $[M/H] = -0.5$ ) with an age in the range 8 – 20 Myr. Later, Laskar et al. (2009) estimated a metallicity of  $[M/H] = -0.2 \pm 0.1$  using high-resolution echelle spectra. Additionally, they determined the visible-band flux ratio for Bb/Ba to be  $0.416 \pm 0.005$ . This value is compatible with the visible-band flux ratios estimated from Baraffe et al. (2015) isochrones at 10 Myr and our BaBb dynamical masses results of 0.458 and 0.428 for solar and sub-solar ( $[M/H] = -0.5$ ) metallicity, respectively (see Appendix 3.7.4). Given the uncertainty on the derived dynamical masses due to the degeneracy between  $K_{Ba}$  and  $K_{Bb}$ , we cannot use the quadruple system yet to benchmark evolutionary track models, calling for additional observations to better constrain both the orbital solutions and the abundances of the four stars. Both I and II AB orbital solutions feature comparable values for the inclination and longitude of the ascending node  $\Omega$ , within  $\lesssim 0.5^{\circ}$  from the latest orbital solution (Kennedy et al. 2019, see Table 3.4). This result shows that despite the fact that the orbit of AB will remain uncertain for several years as more observations are collected, its orientation is already well constrained and robust.

### 3.5.2 Mutual alignment

The mutual inclinations between the inner and outer orbits in a hierarchical system can constrain the initial conditions of its formation (Fekel 1981; Sterzik & Tokovinin 2002). Hierarchical fragmentation of a rotating cloud (Bodenheimer 1978) or fragmentation of a circumbinary disk (Bonnell & Bate 1994) should result in near co-planar configurations. On the other hand, misaligned orbits could be the result of turbulent fragmentation or dynamical interactions (Lee et al. 2019). Similarly, the relation between circumbinary disk orientation and the orbital parameters of the host binary can

**Table 3.5:** Mutual inclinations between all orbital planes in HD 98800 and the circumbinary disk.

Mutual inclination		
$\Phi_{BaBb-AB}$ ( $^\circ$ )	$146.8 \pm 0.5$	
$\Phi_{AaAb-AB}$ ( $^\circ$ )	$49.2 \pm 0.1$	
$\Phi_{AaAb-BaBb}$ ( $^\circ$ )	$157.3 \pm 0.5$	
	$i_{disk} = 26^\circ \quad i_{disk} = 154^\circ$	
$\Phi_{BaBb-Disk}$ ( $^\circ$ )	$89 \pm 1$	$134.2 \pm 1$
$\Phi_{AaAb-Disk}$ ( $^\circ$ )	$111 \pm 1$	$23 \pm 1$
$\Phi_{AB-Disk}$ ( $^\circ$ )	$63 \pm 1$	$66 \pm 1$

be used to better constrain their formation scenarios (Czekala et al. 2019). The relative inclination  $\Phi$  between the inner and outer orbits (or disk) is given by

$$\cos \Phi = \cos i_1 \cos i_2 + \sin i_1 \sin i_2 \cos (\Omega_1 - \Omega_2), \quad (3.9)$$

where  $i_1, i_2$  are the inclinations of each orbit (or disk and orbit) and  $\Omega_1, \Omega_2$  are the corresponding longitudes of the ascending nodes. The mutual inclination  $\Phi$  ranges from  $0^\circ$  to  $180^\circ$ , where  $\Phi = 0^\circ$  corresponds to co-planar and co-rotating orbits. When  $\Phi > 90^\circ$  the systems are retrograde, and  $\Phi = 90^\circ$  means polar configuration. The circumbinary disk of BaBb was initially thought to be co-planar with the host binary (Tokovinin 1999; Prato et al. 2001), but recent ALMA observations revealed that the circumbinary disk is actually in polar configuration (Kennedy et al. 2019). Additionally, Giuppone & Cuello (2019) suggested that the near polar configuration between the circumbinary disk and BaBb orbit is the most stable configuration among all possible disk inclinations. Given that we reduced the uncertainty of  $i$  and  $\Omega$  for the BaBb orbit from  $\sim 3^\circ$  to  $\sim 0.5^\circ$ , it is important to re-calculate the mutual inclination. Kennedy et al. (2019) found that the disk is inclined either by  $26^\circ$  or  $154^\circ$  with respect to the sky plane. The  $\Omega_{disk}$  published in Kennedy et al. (2019) is defined as the node where rotation of the disk is moving towards the observer, that is with a difference of  $\pi$  with respect to our convention. For consistency, we added  $\pi$  to the published value result-

ing in  $\Omega_{disk} = 196^\circ \pm 1^\circ$ . The new mutual inclinations between all the orbital planes of HD 98800 are reported in Table 3.5, including the mutual inclination of the disk with respect to the inner and outer binaries. For these mutual inclination values, we used the AB orbital parameters from solution I (see Table 3.4). Given that the inclination and  $\Omega$  value of solutions I and II are close to each other within  $\sim 0.1^\circ$ , the subsequent analysis remains valid for both outer orbit solutions. The uncertainties were calculated using a Monte-Carlo uncertainty propagation, assuming Gaussian errors. We confirmed the near polar configuration of the disk relative to the orbital plane of BaBb in the case  $i_{disk} = 26^\circ$  and found  $\Phi_{BaBb-Disk} = 134.2^\circ$  in the case  $i_{disk} = 154^\circ$ . Using the posterior distributions from our fitting, and the posteriors from the disk fitting from Kennedy et al. (2019), yields a nominally significant misalignment of the disk angular momentum vector and the binary pericentre vector;  $1.7 \pm 0.5^\circ$ . In principle, this misalignment provides a measurement of the disk mass, but given likely systematic uncertainties, for example, in estimating blended RVs, we consider this measurement to be an upper limit. Updating the calculation from Martin & Lubow (2019) using the 99.7th percentile from our posteriors, the upper limit on the disk mass is  $0.02 M_\odot$ . The angle from polar is slightly smaller, but the binary mass is larger, so our limit is essentially the same as the upper limit computed by Martin & Lubow. Circumbinary disks are preferentially co-planar around short period ( $< 40$  days) host binaries (Czekala et al. 2019), while for longer orbital periods, mutual inclinations are found in a wide range of configurations (Kennedy et al. 2019; Gravity Collaboration et al. 2021; Czekala et al. 2021). In that regard, determining the orbital parameters of binaries and the mutual inclination of the circumbinary disk at intermediate periods (40 - 300 days), such as the presented HD 98800 results, can contribute to better understand the dynamical scenario leading to co-planar or polar disk configurations.

### 3.5.3 Formation history of HD 98800

The HD 98800 system is a member of the TWA Hydrae young loose association (Torres et al. 2008), therefore it is unlikely that it experienced strong external dynamical interactions with other stars. In general, hierarchical systems that formed under high dynamical interactions between nascent protostars have misaligned and eccentric orbits, and their masses are not comparable (Sterzik & Tokovinin 2002). The AB and AaAb orbits are moderately misaligned (see Table 3.5) and, excluding the Ab component,

the masses are comparable. It is expected that the orbital and physical parameters of this quadruple system contain imprints of its formation scenario. Near co-planarity and comparable masses in wide solar-type hierarchical systems can be a sign of their formation from a common core (Tokovinin 2020a). The collapse of two nearby clouds and their inward accretion-driven migration by accretion (Tokovinin & Moe 2020) can result in compact co-planar hierarchical systems with moderate eccentricities and period ratios. However, HD 98800 is a quadruple system with a 2+2 configuration where the inner orbits are counter-rotating and the BaBb is misaligned with the outer orbit AB.

The encounter of two clumps can create shock fronts that lead to the fragmentation of each core into a binary, forming a 2+2 quadruple system (Whitworth 2001). Hypothetically, this formation scenario can produce wide quadruple systems with similar masses between all four components and comparable inner periods, called  $\epsilon$  Lyr type (Tokovinin 2008), where the inner orbits are expected to be mutually misaligned. Generally,  $\epsilon$  Lyr type have wide outer separations ( $P_{outer} \gtrsim 450$  kyr), but more compact 2+2 systems are known as well (HIP 41171,  $P_{outer} \sim 900$  yr, Tokovinin 2019; FIN 332,  $P_{outer} \sim 3000$  yr, Tokovinin 2020b). Although the outer period of HD 98800 is shorter than usual for these systems ( $P \sim 200 - 400$  yr), the orbital configuration still matches this  $\epsilon$  Lyr type except for the expectation of similar masses of its components. The mass-ratio of BaBb and AB are  $\sim 0.8$  and  $\sim 0.9$ , respectively, while the mass-ratio of AaAb binary is  $\sim 0.31$ .

The large BaBb eccentricity and its counter-rotating configuration with respect to the AaAb and AB orbits could be explained as the result of dynamical interactions. Tidal forces may have ripped away circumbinary material from AaAb, and in the same way, may have perturbed the BaBb circumbinary disk and the eccentricity of the host binary. In consequence, the formation process of the HD 98800 system remains unclear.

### 3.5.4 The low mass ratio of AaAb and its lack of a disk

An intriguing characteristic of HD 98800 is that it still holds a massive circumbinary gas disk around the system BaBb (Ribas et al. 2018; Kennedy et al. 2019). Nonetheless, no circumbinary disk has been found around the system AaAb. A possible explanation for the persistent existence of the detected disk has been proposed by Ribas et al.

(2018). These authors speculated that the disk has survived for so long because of the tidal torques exerted by BaBb on the inner edge and by AB on the outer edge, which stopped or significantly reduced viscous accretion, leading to a scenario in which the disk is only losing mass due to photo-evaporation. On the other hand, the lack of a disk around system A, which could have evolved in a similar way as the disk around B, could be related to a faster disk dispersal due to a higher X-ray luminosity, estimated to be  $\sim 4$  times the one of system B (Kastner et al. 2004).

Recently, with a 1D+1D model of gas disk evolution, Ronco et al. (2021) explored the scenario proposed by Ribas et al. (2018) in arbitrary hierarchical triple star systems and, particularly, in HD 98800. They show that the current age and mass of gas of HD 98800 B can be reproduced if the disk was originally an intermediate to high-mass disk ( $\sim 0.05 - 0.1 M_{\odot}$ ), and if it had a moderate to low viscosity ( $10^{-4} - 10^{-3}$ ). To evaluate the current non-existence of a disk around system A, these authors considered, for simplicity, that both the disk parameters and the characteristics of system A (i.e. its mass ratio and separation) were the same as those of the system B, except for its higher X-ray luminosity, as suggested by Kastner et al. (2004). Under these considerations, their simulations show that the possible disk around A may have dissipated in less than 7 – 10 Myr, the estimated age of HD 98800. We know that the assumption of equal inner mass ratios in HD 98800 does not hold. However, Ronco et al. (2021) also show that the smaller the mass ratio of the inner binary in a hierarchical triple star system, the faster the circumbinary disk dissipates, suggesting that the disk around system A in HD 98800 may have dissipated even faster. Our new findings and the characterisation of system A, presented in sec. 3.3.2, effectively show a mass ratio that is much lower than that of system B, reaffirming this possibility and contributing to the explanation of the absence of the A disk.

### 3.6 Summary and conclusions

In this work, we present a new orbital solution for the HD 98800 quadruple system. Using PIONIER observations, we obtained new astrometric positions and a flux ratio of AaAb and BaBb subsystems. We refined the orbital solution presented by Boden et al. (2005) and derived, for the first time, the full orbital solution for the AaAb binary. From our orbital solution, we confirmed the polar configuration of the circumbinary disk around BaBb. Using the dynamical parallax of BaBb, we calculated the dynamical

### 3.6. SUMMARY AND CONCLUSIONS

masses of the AaAb pair. The dynamical masses and parallax are strongly dependent on the RV semi-amplitude  $K_{Ba}$  and  $K_{Bb}$ , estimated mainly from the RV measurements by Torres et al. (1995). New high-resolution spectroscopic observations of HD 98800 could remove possible biases in the estimation of the RV semi-amplitude of the inner systems. Spectroscopic observation with adaptive optics correction could allow us to acquire resolved spectra of each subsystem, thus avoiding line blending of the four components. The estimated visible-band AaAb flux ratio is  $\lesssim 1\%$  (Laskar et al. 2009), making it difficult to disentangle the RV of Ab. From our PIONIER observations, we estimated an H-band flux ratio of  $\sim 14\%$  for the AaAb binary. This more favourable flux ratio opens the possibility to measure, for the first time, the RV of Ab using high resolution infrared spectroscopy. This would allow us to calculate the dynamical masses and parallax of Aa and Ab independently from the parallax of BaBb. Spectroscopic monitoring of HD 98800 is relevant not only for more robust dynamical masses and parallax estimates, but also to properly establish the abundances of the four stars. These measurements will provide valuable inputs to test and improve pre-main sequence evolutionary models and better constrain models of dust disk evolution.

We tested the dynamical stability of the quadruple using N-body simulations. Using the orbital parameters and the mass values of the inner binaries, the simulation probed the long-term stability of this system for both outer orbit solutions; we found that the system should be stable over thousands of orbital periods. The AB outer orbit predicts that the AaAb binary will pass behind the disk around BaBb in the coming years. Using our N-body simulation, we predicted that the transit will start in 2026 and should finish between 2030-2031. This transit presents an unprecedented opportunity to characterise the disk structure along a  $\sim 10$  au long chord, with the width of this chord set by the projected extent of the AaAb orbit.

From mass ratios, periods, eccentricities, and mutual orbit orientations, we evaluate possible formation scenarios for HD 98800. The similarity of the components' masses suggests a common formation history. The misalignment between the orbital planes of the inner binaries and the high eccentricity of the BaBb pair suggest a possible dynamical perturbation. Assuming AaAb as a binary exactly equal to that of system B, but with a higher X-ray luminosity as suggested by Kastner et al. (2004), simulations from Ronco et al. (2021) show that the disk around A can dissipate in less than 10 Myr due to photo-evaporation. This scenario can explain the lack of a cir-

cumbinary disk around the AaAb subsystem. These authors also show that a lower mass ratio could indeed promote faster photo-evaporation of the disk. Thus, the low mass ratio derived here actually agrees with faster disk dispersal.

With the current observational evidence, we cannot properly establish the formation process of HD 98800 as there are still some uncertainties in the parallax of A as well as in the orbit of AB. Recently, other works have also used long-baseline infrared interferometry to characterise hierarchical multiple systems (Kraus et al. 2020; Gravity Collaboration et al. 2021; Czekala et al. 2021). Further monitoring of other hierarchical systems, especially at young ages (1-100 Myr), in combination with large survey data, will improve our understanding of the formation and dynamical evolution of these kinds of systems.

## 3.7 Appendix

### 3.7.1 Observations

This section presents complementary information regarding the observations used in this work. The calibrator stars used in our PIONIER observations are listed in Table 3.6. These calibrators were chosen using the SearchCal tool.

**Table 3.6:** Calibrator stars for HD 98800 observations. The distance column refers to the calibrator to science object angular distance in degrees.

SIMBAD id	distance (deg)	V mag	H mag
HD 98828	0.42	7.83	5.35
HD 98729	0.79	7.77	5.42

Most of the RV measurements used in this work were published by Torres et al. (1995). Here we present the new RV measurements from CHIRON observations and science ready archive spectra, see Table 3.7 and Table 3.8. The RVs used in the orbital fitting of the AB orbit are listed in Table 3.9.

The AB astrometric measurements before 2016 are available at the Washington Double Star catalogue (WDS, Mason et al. 2001) and Tokovinin (2018c). The new as-

**Table 3.7:** Radial velocity measurements for AaAb subsystem.

MJD	$RV_{Aa}$ ( $\text{km s}^{-1}$ )	$\alpha_{Aa}$ ( $\text{km s}^{-1}$ )	(O-C) ( $\text{km s}^{-1}$ )	Instrument
50841.1287	20.1031	0.5	0.0805	ELODIE
50842.1262	19.9605	0.5	-0.0375	ELODIE
54308.4955	12.156	0.8	-0.5271	FEROS
54309.4913	12.218	0.8	-0.1113	FEROS
54309.5368	12.247	0.8	-0.0667	FEROS
54310.4710	12.036	0.8	0.0315	FEROS
54311.4629	11.713	0.8	0.0134	FEROS
54312.4900	11.572	0.8	0.1637	FEROS
54314.4636	11.270	0.8	0.3575	FEROS
54315.4672	11.022	0.8	0.3306	FEROS
57062.2727	9.919	0.8	0.2176	FEROS
59323.1553	15.05	0.5	-0.2036	CHIRON
59338.0931	12.26	2.5	3.4653	CHIRON
59411.9949	7.213	0.5	-0.9481	CHIRON
59421.9871	8.869	0.2	0.1754	CHIRON
59424.9528	8.899	0.2	0.0446	CHIRON

trometry measurement from speckle interferometry at SOAR are listed in Table 3.10.

### 3.7.2 Orbital fitting complementary information

This section presents the prior distributions used for each orbital fitting. Additionally, we also show the corner plots from the posterior samples of each MCMC model. Fig. 3.13 shows the  $V^2$  from KI observations and the best fit binary model from the BaBb orbital fitting result.

### 3.7.3 N-body simulations

In REBOUND, particles (in that case, stars) are added sequentially to the simulation. Even though a ‘primary’ keyword can be provided to indicate, for instance, that star #4 is orbiting star #3, the orbital parameters of the AB orbit are obtained with respect

**Table 3.8:** Radial velocity measurements for BaBb subsystem.

MJD	RV <sub>Ba</sub> (km s <sup>-1</sup> )	$\alpha_{Ba}$ (km s <sup>-1</sup> )	(O-C) (km s <sup>-1</sup> )	Instrument
50841.1287	8.81	2.7	-3.8347	ELODIE
50842.1262	8.35	2.7	-4.4114	ELODIE
59323.1553	14.029	1.0	0.4724	CHIRON
59421.9871	-20.740	0.2	0.0881	CHIRON
59424.9528	-19.045	0.2	-0.2985	CHIRON

MJD	RV <sub>Bb</sub> (km s <sup>-1</sup> )	$\alpha_{Bb}$ (km s <sup>-1</sup> )	(O-C) (km s <sup>-1</sup> )	Instrument
50841.1287	-7.40	0.7	0.6603	ELODIE
50842.1262	-7.82	0.7	0.3855	ELODIE
59323.1553	-2.752	1.5	-0.2293	CHIRON
59421.9871	40.533	0.5	0.2658	CHIRON
59424.9528	38.587	0.5	0.9122	CHIRON

to the centres of mass of AaAb and BaBb, respectively. Therefore, to initialise the simulation, we determined the initial conditions of the four stars. We first added Ba as our heliocentric reference frame, then added Bb by specifying its orbital parameters with respect to Ba and shifted the reference system to the centre of mass of BaBb. Later, we used the AB orbital parameters to simulate a third body with a combined mass  $M_{Aa} + M_{Ab}$  which corresponds to the centre of mass of the A system. We then saved the initial 3D positions  $\vec{x}_0$  and velocities  $\vec{v}_0$  of this third body ‘AaAb’ using the centre of mass of BaBb as the reference frame. We then set up a new simulation, only for the AaAb system to get the initial positions of Aa and Ab,  $\vec{x}_{Aa,0}$ ,  $\vec{x}_{Ab,0}$  and velocities  $\vec{v}_{Aa,0}$ ,  $\vec{v}_{Ab,0}$  with respect to the centre of mass of the AaAb pair. All the positions and velocities for all four stars were calculated at the same reference time, in our case we used  $T_0$  of the AB orbit. Finally, we set up the final simulation by adding Ba, followed by Bb by specifying its orbital parameters with respect to Ba, which moved to the centre of mass of BaBb. We then added Aa by specifying its initial position and velocity calculated earlier, the position and velocity are  $\vec{x}_0 + \vec{x}_{Aa,0}$  and  $\vec{v}_0 + \vec{v}_{Aa,0}$ ,

**Table 3.9:** Radial velocity measurements for AB system.

Median MJD	$RV_A$ ( $\text{km s}^{-1}$ )	$\alpha_A$ ( $\text{km s}^{-1}$ )	(O-C) <sup>a</sup> ( $\text{km s}^{-1}$ )	Source
48635.4564	12.8	0.1	0.0533	TO95
50841.6274	12.1	0.5	1.2209	ELODIE
54311.9669	14.7	0.4	-0.9789	FEROS <sup>b</sup>
57062.7727	12	2	1.2147	FEROS <sup>c</sup>
59375.5439	11.8	0.2	0.0359	CTIO
Median MJD	$RV_B$ ( $\text{km s}^{-1}$ )	$\alpha_B$ ( $\text{km s}^{-1}$ )	(O-C) <sup>a</sup> ( $\text{km s}^{-1}$ )	Source
48635.4564	5.6	0.1	-0.0682	TO95
50841.6274	3.4	0.7	1.5715	ELODIE
58072.3724	5.1	1	0.5269	KE19 <sup>d</sup>
59375.5439	6.4	0.4	-0.0884	CTIO

**Notes.** <sup>(a)</sup> (O-C) from solution I. <sup>(b)</sup> From FEROS observations taken in 2007. <sup>(c)</sup> From FEROS observation taken in 2015. <sup>(d)</sup> Kennedy et al. (2019).

respectively, and we then did the same for Ab.

Figure 3.18 shows the positions of the four stars as we integrated the simulation in time for both solutions I and II, overlapped with the location of the disk. The centre of mass of BaBb is located at (0,0).

### 3.7.4 Flux ratio estimation

We used evolutionary track from Baraffe et al. (2015), assuming an age of 10 Myr, and synthetic photometry with a BT-Settl model grid, provided by the Spanish Virtual Observatory (SVO) web service<sup>13</sup> to estimate the flux ratio corresponding to the dynamical masses obtained in this work. The theoretical flux from the BT-Settl model was scaled by the multiplicative dilution factor  $M_d = (R/D)^2$ ,  $R$  being the stellar radius and  $D$  the distance to the observer (see Tables 3.13 and 3.14).

<sup>13</sup><http://svo2.cab.inta-csic.es/theory/vosa/>

CHAPTER 3. THE HD 98800 QUADRUPLE PRE-MAIN SEQUENCE SYSTEM

**Table 3.10:** Astrometry measurements of AB system.

Date	sep ( $''$ )	$\sigma_{\text{sep}}$ ( $''$ )	(O-C) $_{\text{sep}}^a$ ( $''$ )	P.A. ( $^\circ$ )	$\sigma_{\text{PA}}$ ( $^\circ$ )	(O-C) $_{\text{P.A.}}^a$ ( $^\circ$ )
1909.5	1.0	0.1	0.3106	190.0	2.0	-1.2605
1910.3	0.8	0.1	0.1243	180.0	2.0	8.8414
1912.66	0.65	0.1	0.0153	187.0	2.0	2.1753
1926.25	0.41	0.1	0.0266	192.5	2.0	0.0270
1930.39	0.37	0.1	0.0667	194.0	2.0	0.6809
1936.32	0.23	0.1	0.0422	204.7	2.0	-3.7228
1937.83	0.24	0.1	0.0813	204.1	2.0	-0.0558
1937.98	0.18	0.1	0.0241	206.8	2.0	-2.3872
1959.25	0.18	0.1	-0.1072	348.7	1.0	6.4093
1960.27	0.2	0.1	-0.1068	0.0	1.0	-4.1886
1963.85	0.26	0.1	-0.1151	358.7	1.0	-1.0060
1964.35	0.3	0.1	-0.0845	1.1	1.0	-3.1961
1967.28	0.32	0.1	-0.1188	1.9	1.0	-2.9466
1976.13	0.52	0.1	-0.0713	2.2	1.0	-1.1944
1979.21	0.59	0.1	-0.0486	1.1	1.0	0.3996
1991.25	0.775	0.01	-0.0021	2.9	1.0	0.0363
1991.3882	0.777	0.01	-0.0011	3.2	1.0	-0.2498
1996.1826	0.807	0.02	0.0045	3.1	1.0	0.3122
2004.0860	0.78	0.01	-0.0032	3.0	1.0	1.1590
2006.1913	0.745	0.01	-0.0169	3.7	1.0	0.6725
2009.2638	0.7139	0.002	-0.0021	4.22	0.71	0.4920
2009.2638	0.7144	0.002	-0.0016	4.22	0.9	0.4920
2009.2638	0.714	0.002	-0.0020	4.26	0.31	0.4520
2011.0355	0.6853	0.002	0.0045	5.04	0.61	-0.1085
2011.0355	0.6877	0.002	0.0069	4.95	0.98	-0.0185
2013.1272	0.63	0.002	-0.0003	5.33	0.34	-0.1047
2013.1272	0.6291	0.002	-0.0012	5.34	0.56	-0.1147
2014.0581	0.6021	0.002	-0.0027	4.98	0.43	0.3929
2015.1696	0.571	0.002	-0.0006	5.56	0.26	0.0073
2015.1696	0.572	0.002	-0.0001	5.46	0.71	0.1073
2016.0485	0.546	0.002	0.0019	5.74	0.33	-0.0015
2016.9603	0.513	0.002	0.0005	5.46	0.33	0.4765
2018.0856	0.471	0.002	-0.0009	6.68	0.33	-0.4625
2019.1399	0.429	0.002	-0.0021	6.46	0.20	0.0700
2019.9503	0.395	0.002	-0.0036	6.92	0.22	-0.1055
2020.9961	0.357	0.002	0.0023	7.75	0.22	-0.4891
2021.3159	0.344	0.002	0.0022	7.08	0.24	0.3404

Notes. <sup>(a)</sup> (O-C) from solution I.

**Table 3.11:** Prior distribution used in AaAb and BaBb orbital fitting.

Parameters	AaAb	BaBb
Period (days)	LogUniform [200, 300]	LogUniform[250, 350]
$T_0$ (MJD)	Normal [48737, 20]	Normal [48709, 20]
$e$	Uniform [0, 1]	Uniform [0, 1]
$\omega_{Aa/Ba}$ (rad)	Uniform [0, $2\pi$ ]	Uniform [0, $2\pi$ ]
$\Omega$ (rad)	Uniform [0, $2\pi$ ]	Uniform [0, $2\pi$ ]
$\cos(i)$	Uniform [-1, 1]	Uniform [-1, 1]
$a$ (mas)	Uniform [5, 30]	Uniform [5, 30]
$K_1$ ( $\text{km s}^{-1}$ )	Uniform [0, 20]	Uniform [0, 50]
$K_2$ ( $\text{km s}^{-1}$ )	...	Uniform [0, 50]
$\gamma$	Uniform [0, 20]	Uniform [0, 20]

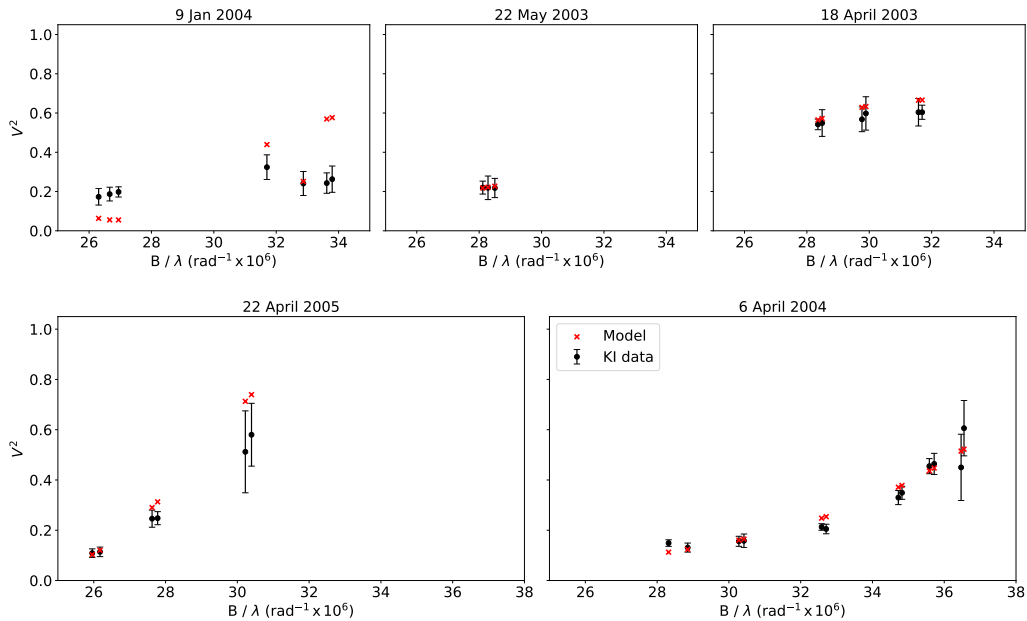


**Figure 3.13:** Squared visibilities from Keck Interferometer observations published in Boden et al. (2005). The black circles represent the observed values and the red crosses represent the best-fit BaBb binary model from this work.

**Table 3.12:** Prior distribution used in AB orbital fitting.

Parameters	AB
Period (years)	LogUniform [100, 500]
$T_0$ (years)	Uniform [2 000, 2 040]
$e$	Uniform [0, 1]
$\omega_A$ (rad)	Uniform [0, $2\pi$ ]
$\Omega$ (rad)	Uniform [0, $2\pi$ ]
$\cos(i)$	Uniform [-1, 1]
$M_A$ ( $M_\odot$ )	Normal [1.22, 0.5]
$M_B$ ( $M_\odot$ )	Normal [1.38, 0.5]
$\pi$ (mas)	Normal [22.0, 0.6]
$\gamma_{AB}$ ( $\text{km s}^{-1}$ )	Uniform[0, 20]

**Table 3.13:** Stellar parameters used for the flux ratio estimation in H-band ( $1.50 - 1.80 \mu\text{m}$ )

Star	Adopted stellar parameters			predicted observed flux	
	$T_{\text{eff}}$ (K)	$\log g$	$R$ ( $R_\odot$ )	([M/H] = 0) <sup>a</sup> ( $\text{erg/cm}^2/\text{s}/A$ )	([M/H] = -0.5) <sup>b</sup> ( $\text{erg/cm}^2/\text{s}/A$ )
Aa	4400	4.5	1.133	$2.2423 \times 10^{-13}$	$2.1823 \times 10^{-13}$
Ab	3400	4.5	0.662	$3.5559 \times 10^{-14}$	$3.2881 \times 10^{-14}$

**Notes.** <sup>(a)</sup> From theoretical flux obtained with the BT-Settl (CIFIST) model (Allard et al. 2013; Caffau et al. 2011) multiplied by the dilution factor  $M_d$ . <sup>(b)</sup> Same as (a), but using the theoretical flux obtained with the BT-Settl (AGSS2009) model (Allard et al. 2013; Asplund et al. 2009).

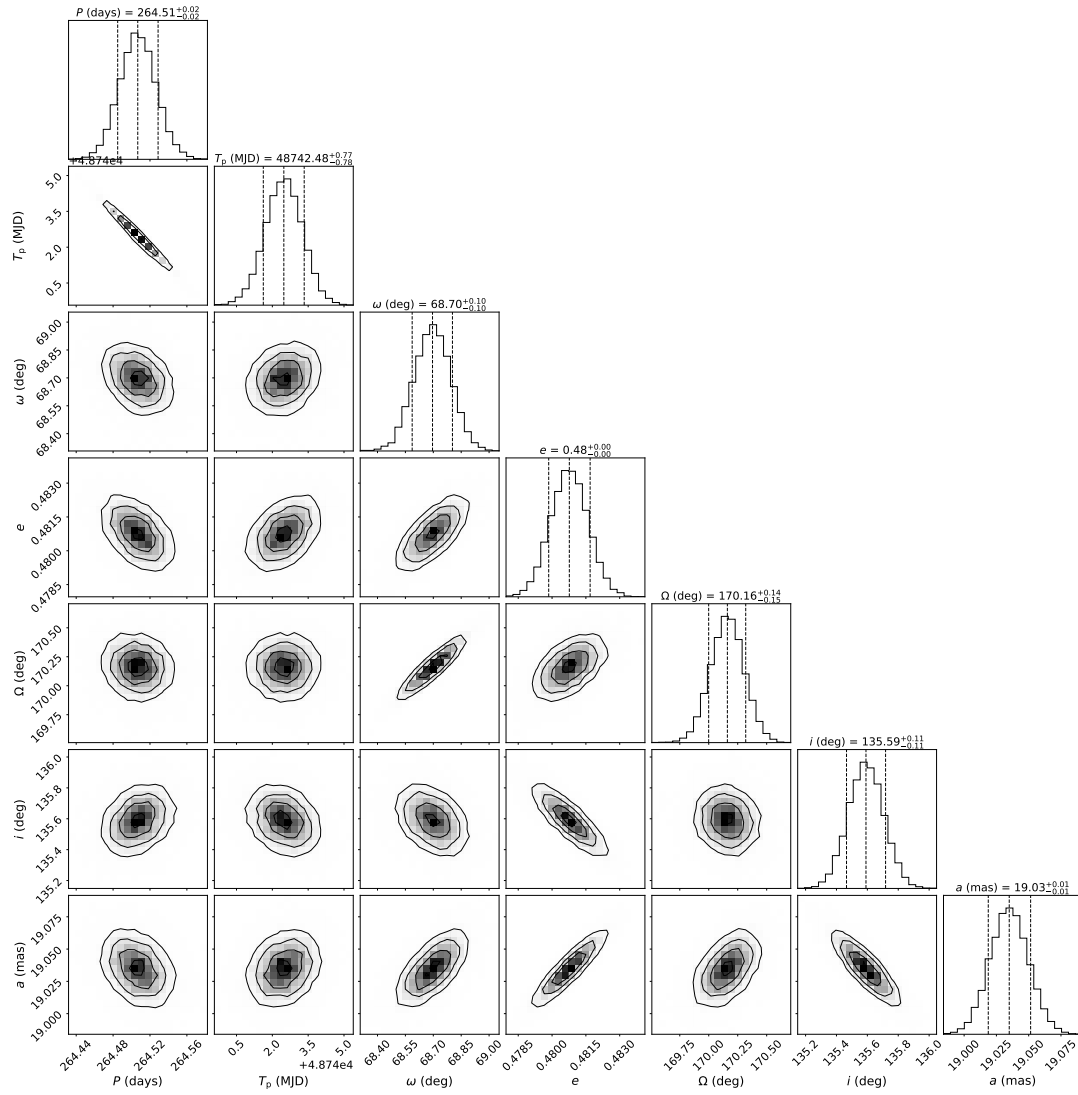


**Figure 3.14:** Posterior samples of AaAb orbital parameters. Contoured sub-panels show the distribution of points from the MCMC chains, where high-density regions are indicated by the greyscale and contours. Histogram sub-panels show the posterior distributions, with median and 68% confidence intervals marked by dashed lines, with titles quantifying those ranges.

CHAPTER 3. THE HD 98800 QUADRUPLE PRE-MAIN SEQUENCE SYSTEM

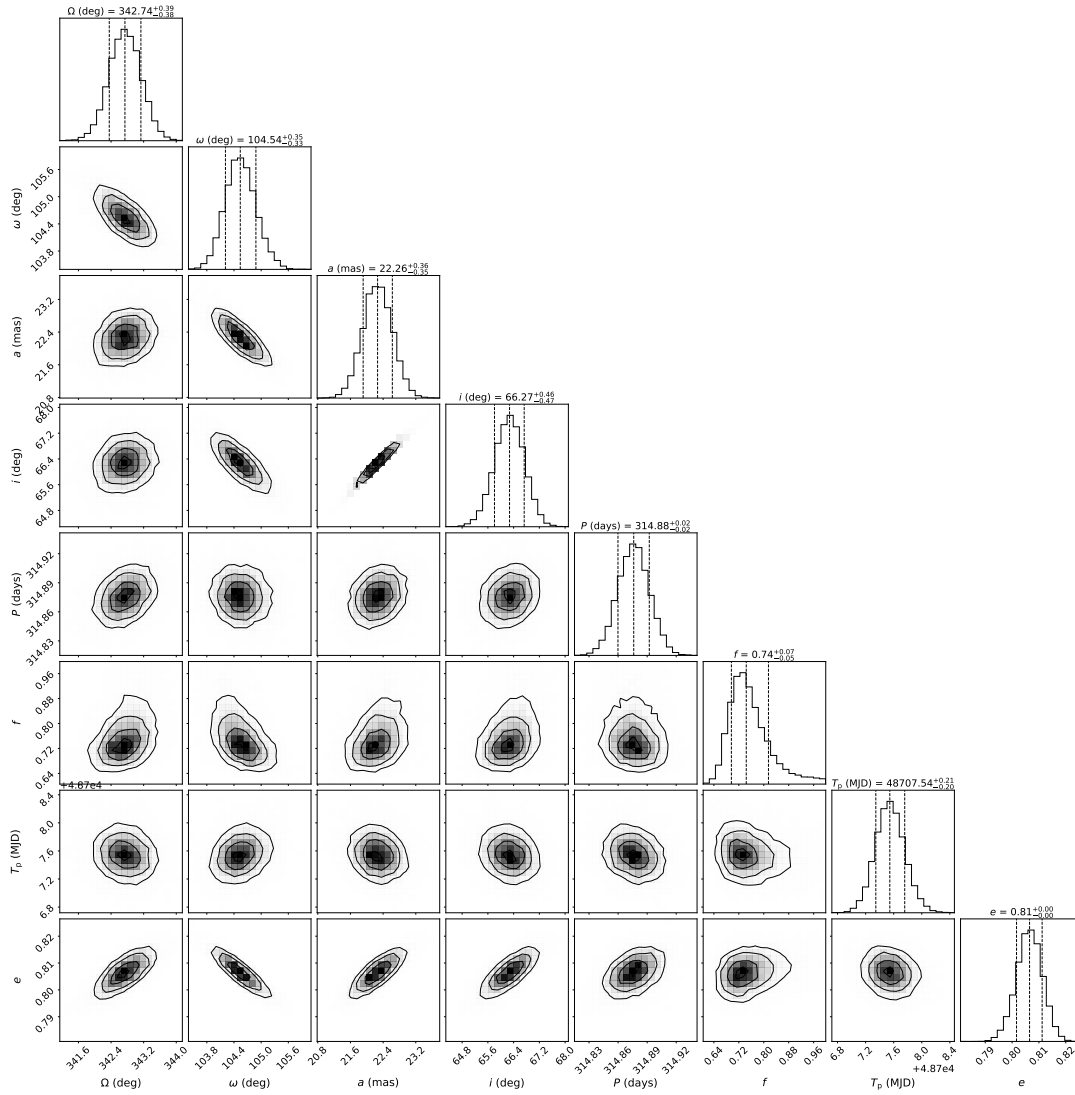


**Figure 3.15:** Posterior samples of BaBb orbital parameters. Contoured sub-panels show the distribution of points from the MCMC chains, where high-density regions are indicated by the greyscale and contours. Histogram sub-panels show the posterior distributions, with median and 68% confidence intervals marked by dashed lines, with titles quantifying those ranges.

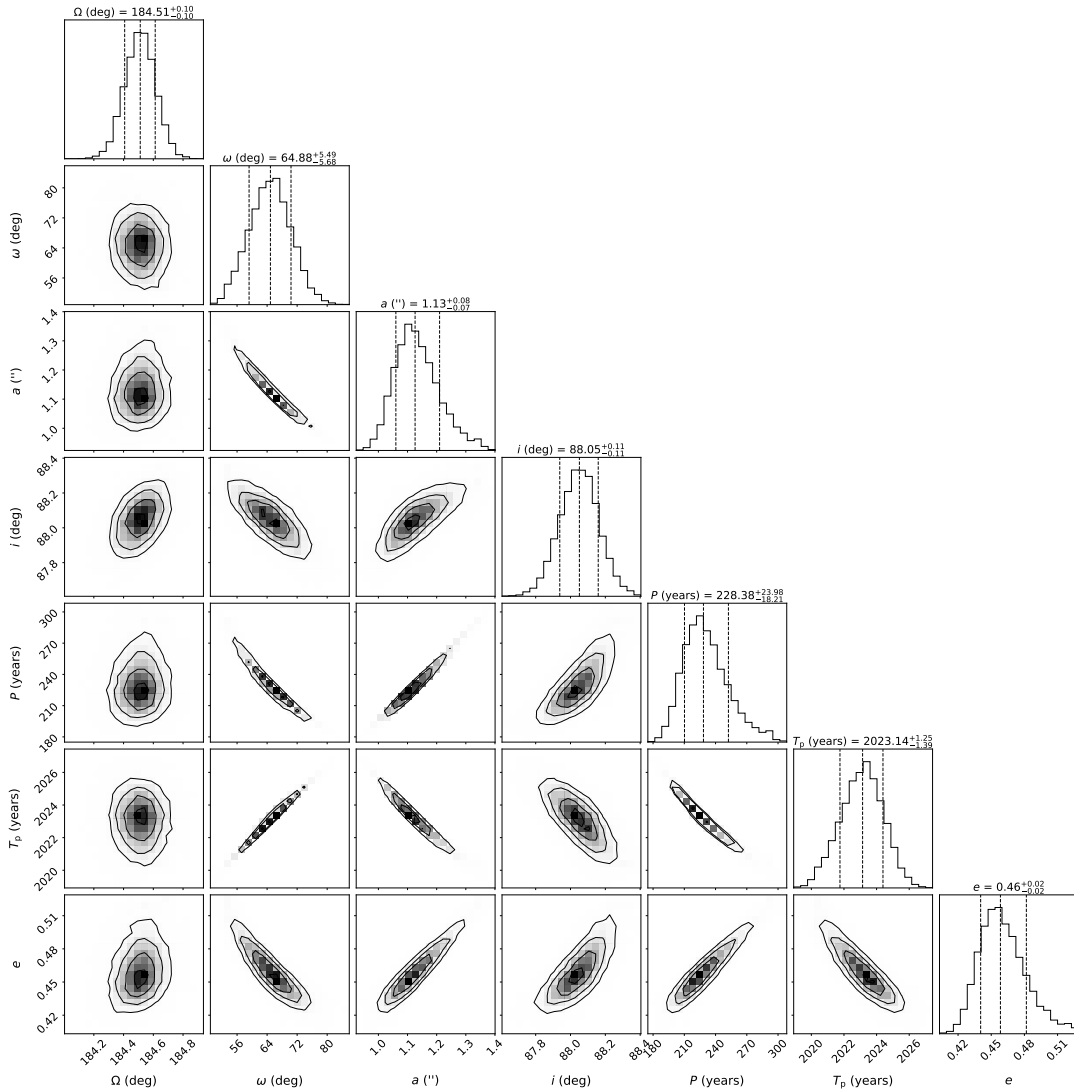


**Figure 3.16:** Posterior samples of AB orbital parameters for solution I. Contoured sub-panels show the distribution of points from the MCMC chains, where high-density regions are indicated by the greyscale and contours. Histogram sub-panels show the posterior distributions, with median and 68% confidence intervals marked by dashed lines, with titles quantifying those ranges.

CHAPTER 3. THE HD 98800 QUADRUPLE PRE-MAIN SEQUENCE SYSTEM

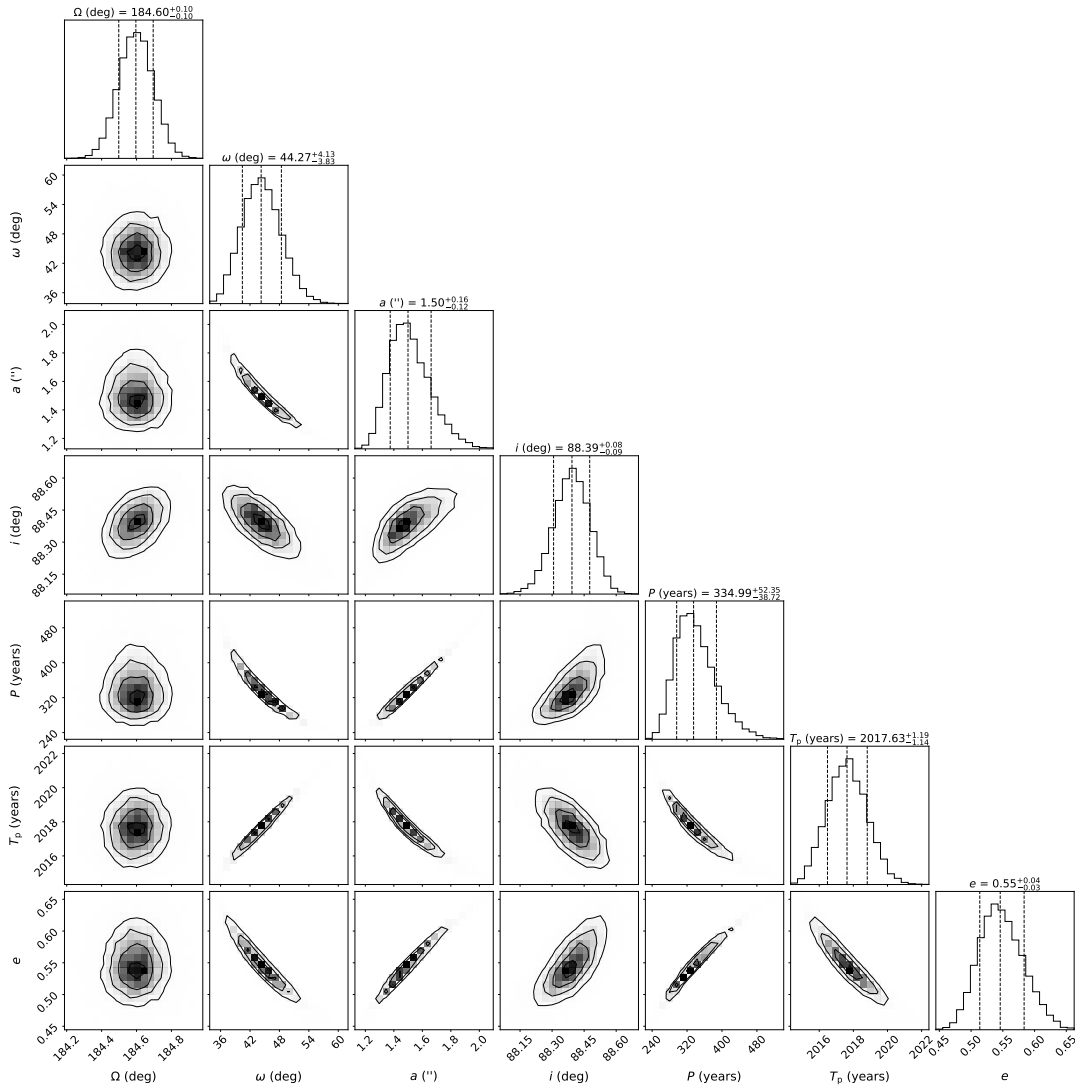


**Figure 3.17:** Posterior samples of AB orbital parameters for solution II. Contoured sub-panels show the distribution of points from the MCMC chains, where high-density regions are indicated by the greyscale and contours. Histogram sub-panels show the posterior distributions, with median and 68% confidence intervals marked by dashed lines, with titles quantifying those ranges.

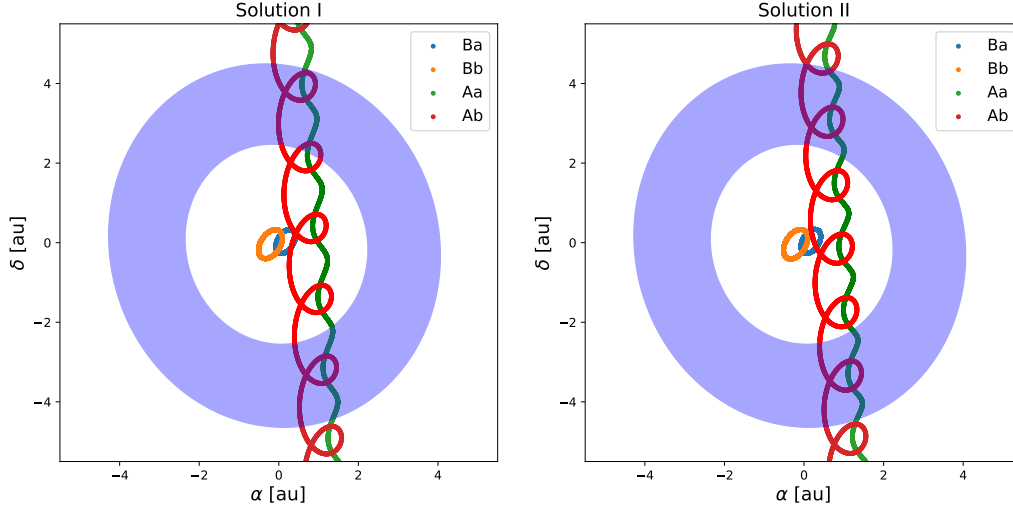


**Figure 3.18:** Integrated orbits at the times of transit of AaAb behind the disk surrounding BaBb, using the best-fit parameters. The disk and the four orbits are referred to the centre of mass of BaBb located at (0,0).

**Table 3.14:** Stellar parameters used for the flux ratio estimation in visible-band (6040.35 – 6128.93 Å)

Star	Adopted stellar parameters			predicted observed flux	
	$T_{\text{eff}}$ (K)	$\log g$	$R$ ( $R_{\odot}$ )	([M/H] = 0) <sup>a</sup> ( $\text{erg}/\text{cm}^2/\text{s}/A$ )	([M/H] = -0.5) <sup>b</sup> ( $\text{erg}/\text{cm}^2/\text{s}/A$ )
Ba	4000	4.5	1.064	$2.8660 \times 10^{-13}$	$3.0026 \times 10^{-13}$
Bb	3700	4.5	0.942	$1.2269 \times 10^{-13}$	$1.3758 \times 10^{-13}$

**Notes.** <sup>(a)</sup> From theoretical flux obtained with the BT-Settl (CIFIST) model (Allard et al. 2013; Caffau et al. 2011) multiplied by the dilution factor  $M_d$ . <sup>(b)</sup> Same as (a), but using the theoretical flux obtained with the BT-Settl (AGSS2009) model (Allard et al. 2013; Asplund et al. 2009).



## CHAPTER 4

# Astrometrically resolved binaries

This chapter presents the work in progress towards full orbital solution determination and dynamical masses calculation for a sample of previously identified binary star systems. These systems are part of our SACY database and were observed using Adaptive Optics (AO) imaging and long-baseline infrared interferometry.

### 4.1 Introduction

So far, within the SACY collaboration, we have identified spectroscopic binaries (Elliott et al. 2014; Zúñiga-Fernández et al. 2021a), close visual binaries (Elliott et al. 2015) and wide and extremely wide binaries (Elliott et al. 2016a; Elliott & Bayo 2016) in young associations. Elliott et al. (2015) analysed AO imaging data for 113 members of the young associations and identified 44 companions around 38 stars. Since then, we have collected data from 27 other AO imaging surveys targeting these young associations, reaching over 2000 AO observations of about 190 individual objects. Similarly, as a part of the multiplicity studies within the SACY project, two VLTI/PIONIER observing runs<sup>1</sup> were conducted in 2016 and 2017. The combination of the AO-imaging and VLTI observations can “bridge the gap” between spectroscopy and direct imaging, covering the angular separation range of  $\sim 1 - 10\,000$  mas. This combination

---

<sup>1</sup>Programs 097.C-0587 and 099.C-0195 (PI: P. Elliott)

of techniques can yield comprehensive multiplicity statistics over a continuous range of projected separations with single-epoch observations, and inclinations, orbits and dynamical masses with multi-epoch observations. One of the great advantages of the SACY sample is the proximity of the stars ( $< 200$  pc) and, therefore, there is a subset of identified systems that show observable orbital motion on the time-scale of  $\sim$ year. This opens up the doorway for astrometric monitoring to constrain their full orbital solutions and determine their dynamical masses.

Stellar evolutionary models are still far from providing accurate predictions of PMS stellar masses (Sheehan et al. 2019), and this discrepancy increases dramatically especially at low-masses ( $< 0.5 M_{\odot}$ , Braun et al. 2021). In this sense, the study of binaries is a powerful method to derive direct measurements of masses that will be of great importance to calibrate the mass-luminosity relationship as a function of their age (especially in the intermediate to low-mass regime for PMS), see Rodet et al. (2018) and Chapter 3 for recent examples. The targets presented here are therefore extremely valuable and full orbital solutions will enlarge the sample of dynamical masses, providing more calibrators for comparison with PMS stellar evolution models.

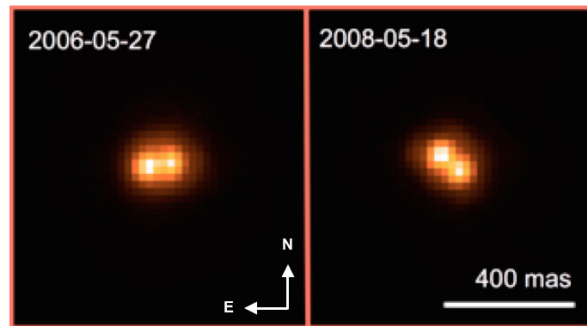


**Figure 4.1:** Two epochs of NACO data for CD-27 11535. This system was identified by Elliott et al. (2015). Note how the system shows significant orbital motion in just two years.

## 4.2 AO-imaging astrometry

From our AO-imaging data collection, there is a subset of  $\sim 20$  identified systems that show observable orbital motion on the time-scale of  $\sim$ years (see Fig. 4.1). From this sample, we selected 16 close binaries for further follow-up observations with the Magellan Adaptive Optics system (MagAO, Close et al. 2012) at Las Campanas Ob-

### 4.3. ASTROMETRY FROM INFRARED INTERFEROMETRY

servatory. These objects were observable within MagAO limiting magnitude (brighter than  $\sim 14$  I-band magnitude) and were visible at the pre-defined visitor mode available nights for proposals. We were awarded observing time for this project in periods 2017B and 2018A (PI: A. Bayo). We present in Table 4.1 the astrometric measurements for 7 systems that were observed with MagAO and have at least two previous observations, so that the full orbital solution can be determined in the near future. The Table also lists the number of MagAO observations (2017B and 2018A) for each system and the source of each astrometric measurements. The true north and the pixel scale for one astrometric field of the 2017B observations was calculated as a part of the undergrad thesis of Bruno Medina, presented as a final Bachelor's project at the Universidad de Valparaíso and supervised by Amelia Bayo. The extension of this work for the astrometric field taken during the 2018A observing campaign is still pending. The next step will be to calculate all the astrometric measurements for all those MagAO observations. It should be noted though that the AO astrometric data discussed here will not provide sufficient coverage to already derive the full orbital solutions but are an important step toward this goal. The MagAO observations provided the third epoch for most of the systems (and even a fourth for a subset of them), which can already be used to guide further observations to ensure better phase coverage.

## 4.3 Astrometry from infrared interferometry

The angular resolution of a telescope is set by the diameter of the primary mirror<sup>2</sup>, i.e. the larger the diameter of the telescope, the higher the angular resolution. However, there are physical and cost limitations to how large we can build a telescope. In that regard, one alternative is the use of smaller telescopes that are connected together to synthesise a larger aperture telescope. This array of telescopes is called an interferometer, and its resolution is defined by the distance between the telescopes known as baseline. Then, an interferometer can have the equivalent resolution of a single telescope the size of the maximum baseline. Long baseline interferometry allows us to spatially resolve components in close binaries, providing astrometric positions at  $\sim 2 - 60$  mas scale with micro-arcsecond accuracy. This observation technique is complementary to the AO observations, for example, the best angular resolution for MagAO is  $\sim 20$  mas in the visible (r'-band) and  $\sim 40$  mas in the near-infrared (J-band). We used the

---

<sup>2</sup> $\theta = 1.22\lambda/D$ , where  $D$  the telescope diameter and  $\lambda$  the wavelength of observation.

CHAPTER 4. ASTROMETRICALLY RESOLVED BINARIES

**Table 4.1:** Astrometric measurements of systems observed with AO-imaging. The last column shows the number of observations taken in our MagAO observing runs.

ID	Sep ( $''$ )	$\sigma_{\text{sep}}$ ( $''$ )	P.A. ( $^\circ$ )	$\sigma_{\text{PA}}$ ( $^\circ$ )	Comp	Date (Year)	Source	Num. MagAO observations
CD-26 13904	0.29	0.01	79.22	0.22	A, B	2006.5274	Elliott et al. (2015)	2
CD-26 13904	0.26	0.01	83.99	0.23	A, B	2008.3156	Elliott et al. (2015)	
CD-44 753	0.13	0.01	294.74	0.27	A, B	2012.5260	Elliott et al. (2015)	1
CD-44 753	0.097	0.001	212.5	1.2	A, B	2015.9800	Janson et al. (2017)	
CD-27 11535	0.09	0.01	278.82	0.22	A, B	2006.4014	Elliott et al. (2015)	2
CD-27 11535	0.09	0.01	228.83	0.22	A, B	2008.3784	Elliott et al. (2015)	
GJ 4231	0.18	0.03	309.5	...	A, B	2003.6315	Galicher et al. (2016)	1
GJ 4231	0.18	0.01	1.5	...	A, B	2006.5466	Galicher et al. (2016)	
GJ 4231	0.16	0.01	298.43	0.23	A, B	2012.5068	Elliott et al. (2015)	
GJ 4231	0.58	0.03	316.0	...	A, C	2003.6315	Galicher et al. (2016)	1
GJ 4231	0.55	0.01	338.0	...	A, C	2006.5466	Galicher et al. (2016)	
GJ 4231	0.54	0.01	360.43	0.23	A, C	2012.5068	Elliott et al. (2015)	
BD-18 4452	3.52	0.01	191.72	0.22	A, B	2006.3904	Elliott et al. (2015)	1
BD-18 4452	3.46	0.01	188.98	0.23	A, B	2008.3811	Elliott et al. (2015)	
BD-07 2388	0.11	0.01	328.65	0.22	A, B	2012.4057	Elliott et al. (2015)	1
BD-07 2388	0.14	0.02	315.0	...	A, B	2002.9904	Galicher et al. (2016)	
BD-07 2388	0.08	0.03	279.0	...	A, B	2006.9384	Galicher et al. (2016)	

VLTI with the four-telescopes combiner PIONIER. Our observations were carried out in 2016 and 2017 using the 1.8 m ATs with the longest baseline configuration (AO-G1-J2-J3), which provides an inner working angle and outer working angle of 1.5 mas and 100 mas, respectively.

Our sample of targets observed with VLTI/PIONIER has primary masses in the range of  $0.8 - 1.2 M_{\odot}$ , estimated using the evolutionary tracks of Baraffe et al. (2015). We chose this primary mass range as it is representative of our overall sample. The targets were chosen without prior information about their multiplicity. This was to avoid any inherent bias in the multiplicity statistics. Therefore, the targets have been selected based on their RA and DEC, magnitude (all brighter than 7 mag. in H-band) and primary mass estimation only. From these observations, we retrieved all the science ready data from the ESO archive<sup>3</sup>. These data have been reduced with the pndrs pipeline (more details in Sec. 3.2.1 and Le Bouquin et al. 2011). For each PIONIER

<sup>3</sup><http://archive.eso.org/scienceportal/home>

### 4.3. ASTROMETRY FROM INFRARED INTERFEROMETRY

observation, we searched for point sources within the field of view ( $\text{FOV} \leq 60 \text{ mas}$  to avoid spectral smearing of the companion, see Le Bouquin & Absil 2012; Gallenne et al. 2015). We determined the astrometric positions of the point sources detected by fitting the  $V^2$  and CP with a binary model using the interferometric tool CANDID<sup>4</sup> (for more details see Sec. 3.2.2). From the 26 targets observed, we identified seven binary candidates (detection rate  $\approx 27\%$ ). For each binary candidate detection, we searched in the literature whether the multiple nature of the system was known using other observation techniques. We report here the detection of a candidate companion for two objects that were flagged as non-confirmed SB candidates in our last update of SBs in the SACY sample (see Chapter 2). A summary of relevant information collected for the binary systems identified with the PIONIER observations is presented in Table 4.2, including the number of observations from this work, the type of binary and the period for the case of previously published orbital solutions. The astrometric positions, flux ratios and detection level for each identified binary are listed in Table 4.3, where the detection level corresponds to the improvement of using a binary model rather than a uniform disk model (i.e. single star, more details see Gallenne et al. 2019). These observations open the possibility to refine the orbital inclination of previously identified systems (V343 Nor, CD-33 7795 A and HD 217379 A) and help us to obtain preliminary orbital solutions for newly identified systems. This information will help us to plan future observations to achieve a full orbital solution.

The future work required to obtain full orbital characterisation of the astrometrically resolved binaries presented here is further discussed in Chapter 7.

---

<sup>4</sup><https://github.com/agallenne/GUICandid>

CHAPTER 4. ASTROMETRICALLY RESOLVED BINARIES

**Table 4.2:** Properties of multiple systems identified with our PIONIER observations.

ID	num. obs. (this work)	binary flag*	Period (year)	Notes from literature	Ref.
CD-53 544	2	SB1	...	Flagged as an SB candidate but not confirmed.	a
HD 3221	3	...	...	Flagged as a fast rotator.	a
HD 13183	2	SB1	...	Flagged as a confirmed SB1.	a, b, c
V343 Nor	1	VB/SB1	4.576	Triple system, wide companion at $\sim 10''$ .	d
CD-33 7795 A	1	VB/SB3	6.025	Triple system, wide companion at $\sim 2''$ .	e, f
HD 217379 A	2	SB3	0.055	Triple system, wide companion at $\sim 2''$ .	g
DK Cet	2	...	...	High proper motion star.	h

**Notes.** (\*) VB: Visual binary. SB: Spectroscopic binary. **References:** <sup>(a)</sup> Zúñiga-Fernández et al. (2021a), <sup>(b)</sup> Cutispoto et al. (2002), <sup>(c)</sup> Nordstrom et al. (1996), <sup>(d)</sup> Nielsen et al. (2016), <sup>(e)</sup> Macintosh et al. (2001), <sup>(f)</sup> Köhler et al. (2013), <sup>(g)</sup> Tokovinin (2016a), <sup>(h)</sup> Gaia Collaboration et al. (2018).

**Table 4.3:** Relative astrometric position of the secondary component and flux ratio for binary candidates identified with our PIONIER observations.

ID	$\Delta\alpha$ (mas)	$\sigma_{\Delta\alpha}$ (mas)	$\Delta\delta$ (mas)	$\sigma_{\Delta\delta}$ (mas)	MJD	$f_2/f_1$ (%)	$\sigma_{f_2/f_1}$ (%)	Detection level
HD 13183 <sup>a</sup>	-25.110	0.098	16.294	0.169	57597.412	1.771	0.285	$4.1\sigma$
HD 13183 <sup>a</sup>	-4.235	0.104	-16.955	0.129	57597.439	2.901	0.633	$3.3\sigma$
CD-53 544	-17.535	0.046	-9.917	0.016	57601.429	101.248	2.917	$> 8\sigma$
CD-53 544	-20.304	0.017	-9.478	0.193	57624.357	95.931	4.272	$> 8\sigma$
HD 3221	-20.304	0.192	8.040	0.331	57638.290	104.901	15.551	$> 8\sigma$
HD 3221	0.651	0.021	-10.614	0.010	57995.288	99.887	0.804	$> 8\sigma$
HD 3221	1.295	0.019	-10.445	0.007	57997.321	102.988	1.798	$> 8\sigma$
V343 Nor	27.286	0.091	-0.978	0.080	57873.090	6.471	0.218	$3.9\sigma$
CD-33 7795 A	29.016	0.139	49.116	0.121	57874.073	54.912	9.411	$> 8\sigma$
HD 217379 A	-5.991	0.005	1.897	0.006	57995.212	82.745	0.849	$> 8\sigma$
HD 217379 A	-5.993	0.004	1.908	0.006	57995.225	83.966	0.679	$> 8\sigma$
DK Cet <sup>a</sup>	-4.27	0.054	-10.187	0.077	57994.341	1.092	0.162	$3.6\sigma$
DK Cet <sup>a</sup>	-0.427	0.031	-2.754	0.046	57996.376	2.381	0.261	$6.3\sigma$

**Notes.** <sup>(a)</sup> Low flux ratio. The astrometry errors could be underestimated.

# CHAPTER 5

## Instrumentation

The Very Large Telescope Interferometer (VLTI) combines the light of the four Unit Telescope or the four movable 1.8 m Auxiliary Telescopes (ATs) to provide milli-arcsec angular resolution at near and mid-infrared wavelengths. Rather than the size of the individual telescopes, the resolution of an interferometer is defined by the distance between the telescopes, called the baseline<sup>1</sup>. The interferometer, instead of taking images of the stars, records the interference pattern (known as fringes) created by combining the light from two or more telescopes. To produce the interference fringes, the light coming from each telescope has to be coherently combined, or in other words, have to travel the same distance. To compensate the delay between the incoming beams, the optical paths between the two telescopes and the focal plane have to be equalised within a fraction of wavelength using optical delay lines<sup>2</sup> (see Fig. 5.1). The main measurements from interferometric observations are the amplitude of the fringes and the phase. The amplitude of the fringes is usually called the visibility. By measuring the drop in the visibility measurements, astronomer can obtain information about the size, shape, and surface features of a star. The phase of the fringes is affected by the turbulence in the Earth's atmosphere. The combination of three telescope measurements

---

<sup>1</sup> $\theta = 1.22\lambda/B$ , where  $\lambda$  and  $B$  correspond to the wavelength and the baseline, respectively.

<sup>2</sup><https://www.eso.org/sci/facilities/paranal/telescopes/vlti/subsystems/delaylines.html>

is used to cancel the atmospheric turbulence and recover the phase information, this quantity is called the closure phase. The closure phase is sensitive to asymmetries in the source distribution (for more details see Lawson 2000; Monnier 2003).

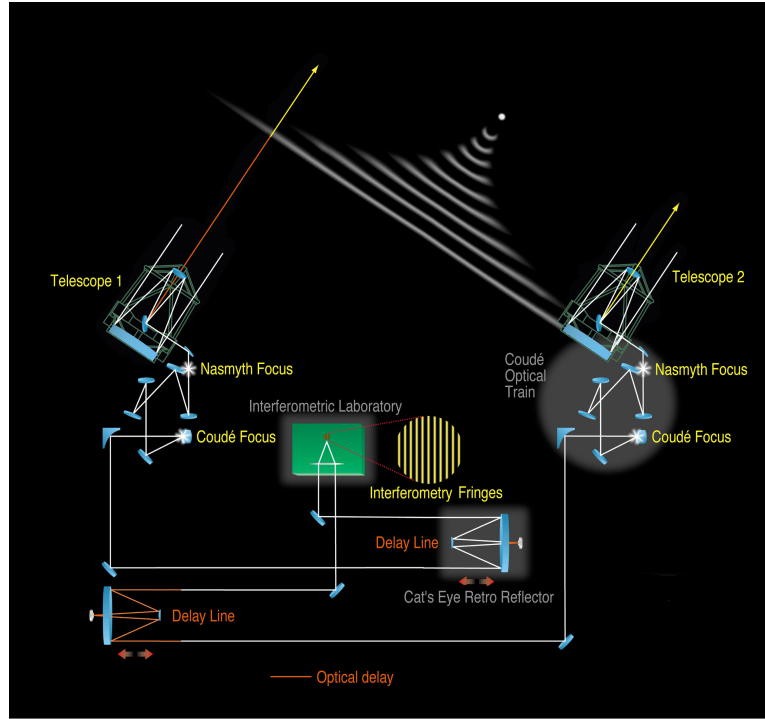


**Figure 5.1:** Schematic layout of the VLT Interferometer. The light from a celestial target is collected from two VLT telescopes and is reflected into the interferometric tunnel. Two delay lines with movable carts continuously adjust their position to keep the two beams in phase. The light is sent to the interferometric laboratory into one of VLTI instruments. The light from multiples telescopes is combined and the interference fringes are recorded in a camera (Credit: ESO).

For the science that we want to do for nearby young stars, the ATs are well suited (as the stars are usually bright), although the ATs have some limitations, such as the injection stability and limiting magnitude. The tip/tilt correction system of the ATs (STRAP, Bonaccini et al. 1997), under good seeing conditions, provided corrections that allowed astronomers to observe with the VLTI. Nevertheless, as soon as the seeing was degrading below  $1''$ , the image delivered by the telescopes degrades significantly and the amount of light injected into the single mode fibres of the interferometric instruments decreases and becomes very unstable, making the observations difficult or impossible. The wavefront errors from the telescopes either degrade the fringe con-

trast directly or lower the flux coupled into the fibre, affecting the sensitivity of the interferometric array. To remedy this situation, the New Adaptive Optics Module for Interferometry (NAOMI) was proposed and later developed by a consortium composed by the Institut de Planétologie et d’Astrophysique de Grenoble (IPAG) and ESO. The final design review was passed in early 2017, and the building of the instruments began at IPAG and ESO Headquarters. We contacted Dr. Jean-Philippe Berger, who was part of my PhD committee, and we arranged for a research stay of three months at IPAG between May and July of 2018. The aim of this visit was to develop on-sky performance simulations for NAOMI before the commissioning so that we would have a reference point during the installation in Paranal. This project culminated in my participation in the fourth commissioning stage of the instrument, when all four ATs were equipped with their NAOMI module. This collaboration resulted in my participation in the publication “NAOMI: the adaptive optics system of the Auxiliary Telescopes of the VLTI,” Woillez, J., Abad, J. A., (80 more), S. Zúñiga-Fernández, 2019, *A&A*, 629, A41. This chapter describes the work I performed for this project both during my research stay and the commissioning.

## 5.1 Glossary

This section briefly describes some concepts and acronyms frequently used in this chapter related to technical aspects of NAOMI operations.

**AO** Adaptive Optics is a technology that uses deformable mirrors, controlled by a feedback loop, that can correct in real-time the distortion caused by the turbulence of the Earth’s atmosphere.

**WFS** Wave-front sensor. A device for measuring the aberration of an optical wave-front. This device is one the major components in any AO system.

**SR** Strehl ratio, defined as the ratio of the atmospherically perturbed image peak intensity from a point source compared to the maximum intensity from an ideal optical system limited only by diffraction over the system’s aperture. This parameter is usually used to measure the performance of an AO system.

**CCD** Charge-coupled device (image sensor). A sensitive detector of photons used in telescopes to produce images.

**RON** Read-out-noise. It is one of the intrinsic CCD noise source. It comes from the physical electronic device that convert the charge (i.e. electrons) into a change in voltage.

**EM amplification** electro-multiplicative gain. Reduce the RON of the NAOMI's WFS detector.

**GS** Guide star. Reference star used by the AO system to measure the wavefront distortions. Sometimes the science targets is not bright enough for the AO systems and therefore we need a natural or laser guide star.

## 5.2 Read Out Noise and NAOMI operations modes

To simulate the performance of NAOMI we<sup>3</sup> used SOAPy<sup>4</sup>, a Monte-Carlo Adaptive Optics Simulation toolkit written in Python, establishing the proper configuration parameters that better simulate the response of NAOMI under different operation modes. These modes depend mainly on the magnitude of the GS. Thus, four detector parameters are configured to optimise the AO performance for different flux conditions: EM amplification, camera frame rate, CCD gain setting, and clock speed (or frame rate).

We tested around 40 different conditions mixing magnitude of the guide stars (GS), read out noise (RON) and frame rate. This preliminary test was also useful to visualise the influence of the RON, and so the importance of the EM amplification, in the performance of NAOMI (see Fig. 5.2). The performance of NAOMI in our simulation is quantified with the Strehl ratio (SR) value. The simulation was carried out with the same nominal seeing (1.1''), atmospheric time constant<sup>5</sup> ( $\tau_0 = 2.5$  ms) and wavelength (658 nm) used in the System Analysis Report (ESO, private communication). The EM amplification keeps the RON low and stable in all operation modes of NAOMI, therefore we kept the WFS RON parameter in the SOAPy configuration as a fixed value (10e RON). Other parameters were fixed according to the characteristic of the AO system,

---

<sup>3</sup>The plural form is used for stylistic reasons. However, the work presented in this chapter has been developed mainly by the author.

<sup>4</sup><https://github.com/AOtools/soapy>

<sup>5</sup> $\tau_0$  is proportional but not equal to the coherence time ( $\tau_c$ ) used in long-baseline interferometry. A certain  $\tau_0$  give us the minimum sample time required for optimal correction with an adaptive optics system (Roddier 1981; Kervella et al. 2017)

## 5.2. READ OUT NOISE AND NAOMI OPERATIONS MODES

like primary mirror diameter, DM actuators and the number of WFS apertures (see Table 5.1). However, there are other configuration parameters that need to be fine tuned depending on the operating modes of the system. In that regard, we ran several simulations in order to find the SOAPy configuration parameters that would reproduce the laboratory-measured SR performance for each operation mode of NAOMI (documented in the System Analysis Report, private communication). These operation modes have different loop frequency, loop gain and controlled modes depending on the observing conditions and GS magnitudes (details in Sec. 2.4 of Woillez et al. 2019). In our simulation we keep the loop gain and the controlled modes fixed (see Table 5.1), and simulated the NAOMI operation mode only by changing the loop frequency depending on the GS magnitude. Then the expected performance of these operation modes corresponds to a  $SR \sim 0.55$  for GS brighter than 13 R-band magnitude with a loop frequency of 500 Hz,  $SR \sim 0.3 - 0.2$  for GS between 12 - 13.5 R-band magnitude with a loop frequency of 100 Hz and  $SR \sim 0.1$  for GS fainter than 13.5 down to 15.5 R-band magnitude with a loop frequency of 50 Hz (coloured zones in Fig. 5.2 and Fig. 5.3). Finally, we obtained results consistent with the values previously reported by ESO (see, Fig. 5.3). As expected, every simulated operation mode achieves its best performance in the reported optimal operation modes for a given R-band magnitude range .

<b>WFS</b>	Value	Comments
Num. sub-aperture	4	4x4 lenslet array.
Pixels per sub-aperture	6	6x6 pixel array.
Sub-aperture FOV	2.25''	
Wavelength	658 nm	R-band.
<b>DM</b>		
Type	Zernike	zernike modes control in NAOMI.
Num. actuator	15	15 controlled modes.
Gain	0.7	Loop gain.
<b>Telescope</b>		
Diameter	1.82 m	ATs primary mirror diameter.
Central obscuration	0.14 m	Secondary mirror diameter.

**Table 5.1:** Parameters fixed in the configuration file of SOAPy in our simulations<sup>6</sup>.

<sup>6</sup><https://soapy.readthedocs.io/en/latest/Configuration.html>

## CHAPTER 5. INSTRUMENTATION

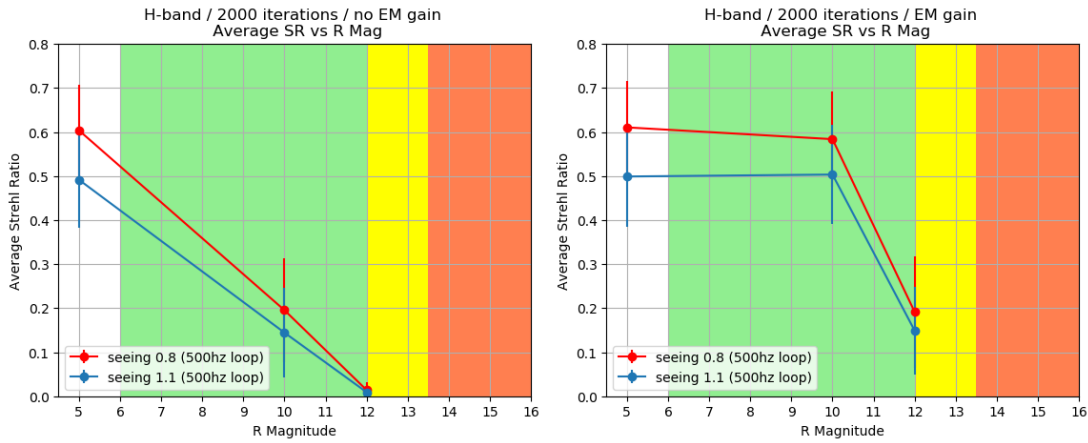


**Figure 5.2:** Average Strehl ratio as a function of the R-band magnitude to test the influence of the RON in the performance of NAOMI. *Left:* WFS detector 65e RON (no EM gain). *Right:* WFS detector 10e RON (EM gain applied). Background colours are used as a reference of the operation modes of NAOMI depending on the R-band magnitude of the GS.

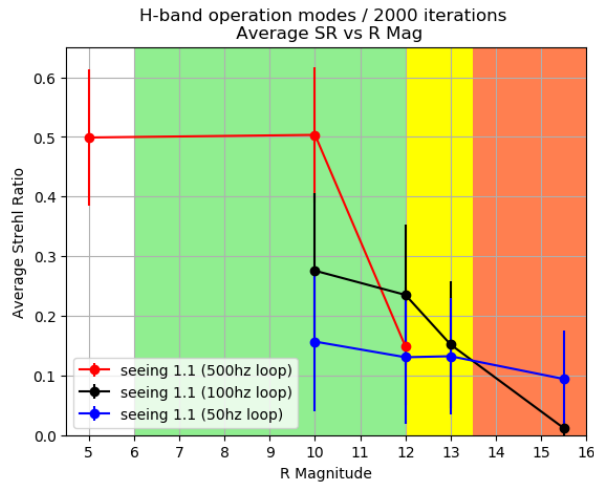


**Figure 5.3:** Average Strehl ratio as a function of R-band magnitude for different operation modes. The coloured lines correspond to the simulated performance of each operation mode configuration. The coloured areas are the optimal operation mode for a given R-band magnitude range taken the System Analysis Report (ESO, private communication).

### 5.3 NAOMI performance simulations

After the operation mode test and SOAPy configuration verification stage, we conducted a set of simulations for two different sky conditions and five GS magnitudes (see Table 5.2) in order to obtain statistical estimates of the instantaneous SR and con-

### 5.3. NAOMI PERFORMANCE SIMULATIONS

trast parameter for NAOMI. For each of these magnitudes and sky condition combinations, we ran two AO simulations (two telescopes) saving 2000 SR values for each of them. Those simulations were performed for the H-band and K-band science camera.

R Mag	Loop frequency (fps)
5	500
10	500
12	100
13	100
15.5	50

ID	Seeing (")	$\tau_0$ (ms)
Regular sky	1.1	2.5
Bad Sky	1.4	1.5

**Table 5.2:** Loop frequency for each GS magnitude (left), the simulations were conducted over two different sky condition (right). The regular sky is a pessimistic case, median seeing at Paranal is about  $0.8''$  and  $\tau_0 \sim 3.5$  ms.

The resulting data were used to build histograms and compute several statistics of interest. In addition to plotting the instantaneous SR we generated a histogram of the fringe contrast parameter  $C$ , which is a measure of the interference quality (coherence) between the light beam from two telescopes. Good fringe contrast is needed to accurately measure interference signals. Fringe contrast is scaled from 0 to 1, where 0 is no fringe contrast, and 1 is perfect fringe contrast. In our case we quantified the fringe contrast parameter using the SR simulation for two telescopes, described by the following equation

$$C = \frac{2\sqrt{SR1 \cdot SR2}}{SR1 + SR2} \quad (5.1)$$

This information will serve as predicted results of the on-sky performance of NAOMI that will be useful during the commissioning.

#### 5.3.1 H-Band results

The simulation of NAOMI performance in H-band shows that the VLTI could operate with the ATs even in degraded seeing conditions. Figures 5.4 and 5.5 show the SR and the contrast parameter results for two sky conditions: regular sky and bad sky, respectively (see Table 5.2). In each figure we show an example of the results of two GS that are close to the expected magnitude limit of NAOMI (R-band magnitude 10 and 12). The results show that for GS fainter than  $\sim 12$  R-band magnitude, under bad

sky conditions (see Fig. 5.5), the degradation of the SR begins to be more noticeable, however the contrast still remains relatively stable.

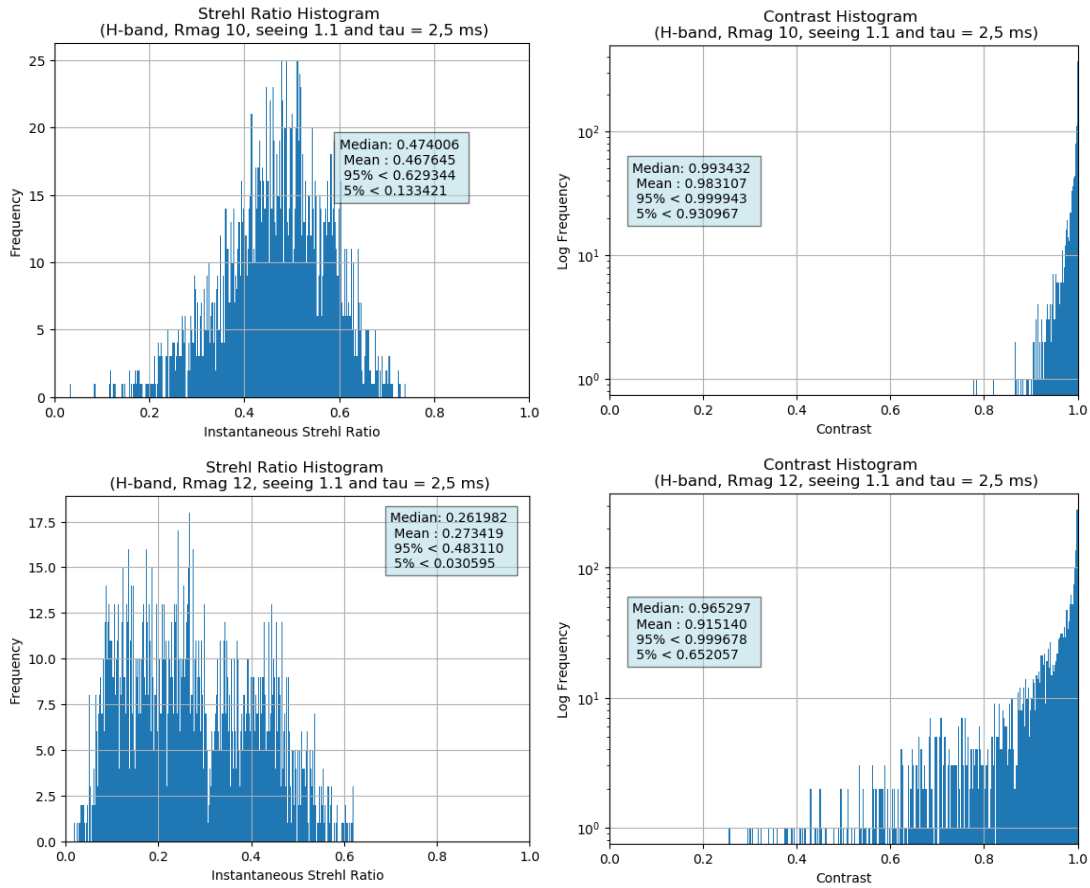


**Figure 5.4:** Instantaneous SR and contrast statistics under regular sky conditions. Each row corresponds to a different GS R magnitude. *Top:* GS Rmag = 10. *Bottom:* GS Rmag = 12.

### 5.3.2 K-Band results

For the simulations in K-band, we obtained similar results compared to the H-band case. The performance of NAOMI starts to degrade around the R-band magnitude of about 12, under bad sky conditions. Figures 5.4 and 5.5 show the SR and the contrast parameter results for two sky conditions, regular sky and bad sky respectively (see Table 5.2). In each figure we show an example of the results of two GS that are close to the expected magnitude limit of NAOMI (R-band magnitude 10 and 12).

## 5.4. COMMISSIONING AND FINAL RESULTS

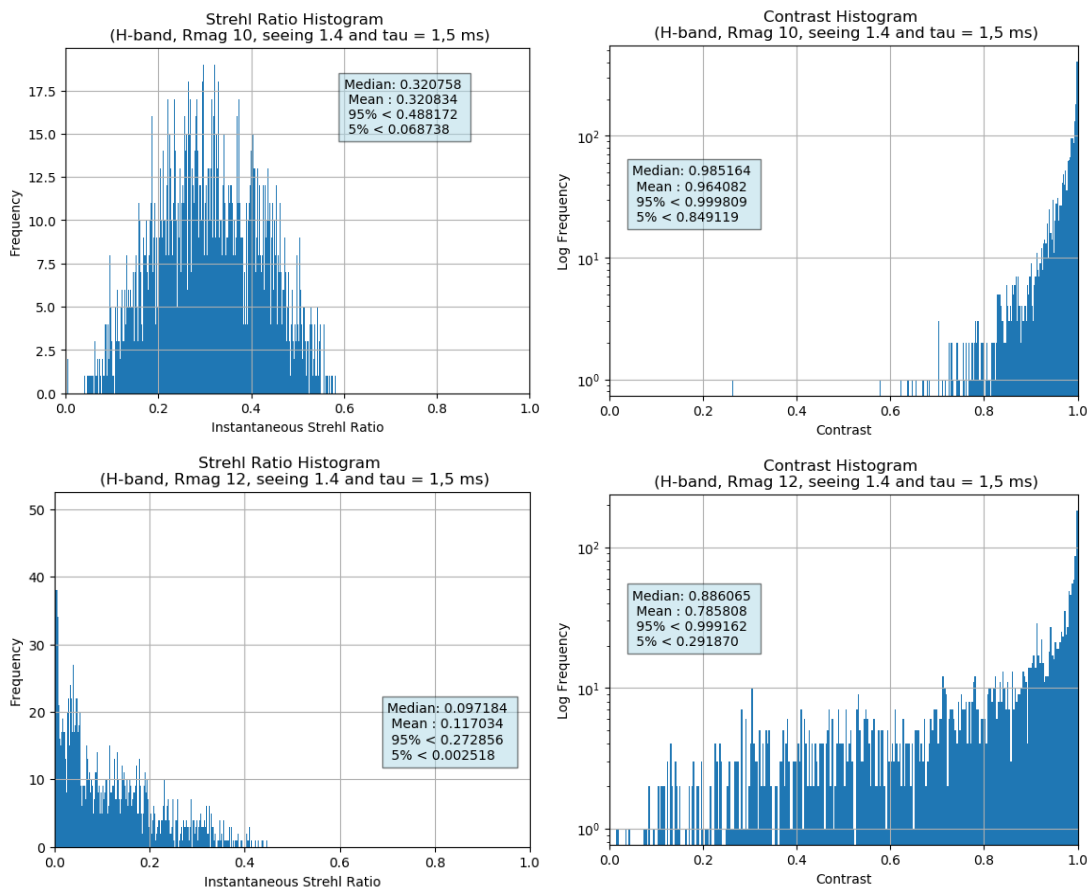


**Figure 5.5:** Instantaneous SR and contrast statistics under bad sky conditions. Each row corresponds to a different GS R magnitude. *Top:* GS Rmag = 10. *Bottom:* GS Rmag = 12.

## 5.4 Commissioning and final results

During my 3 months stay at IPAG I developed performance simulation of the NAOMI systems. These simulations provided statistical results for the SR and contrast parameter over five GS R-band magnitudes in two sky conditions. Those sets of simulations were carried out for both the H-band and K-band science cameras. The results of this work were used as an estimation of the on-sky performance of NAOMI prior the commissioning campaign.

In November 2018, I participated in the commissioning campaign at Paranal when NAOMI was installed in the four ATs during the last 12 days of the commissioning shift. My duties were mainly taking care of the operation of GRAVITY and running the new SNR simulator for NAOMI+GRAVITY (and NAOMI+PIONIER) under different atmospheric conditions. Under  $1.1''$  seeing conditions in the high Strehl regime

CHAPTER 5. INSTRUMENTATION

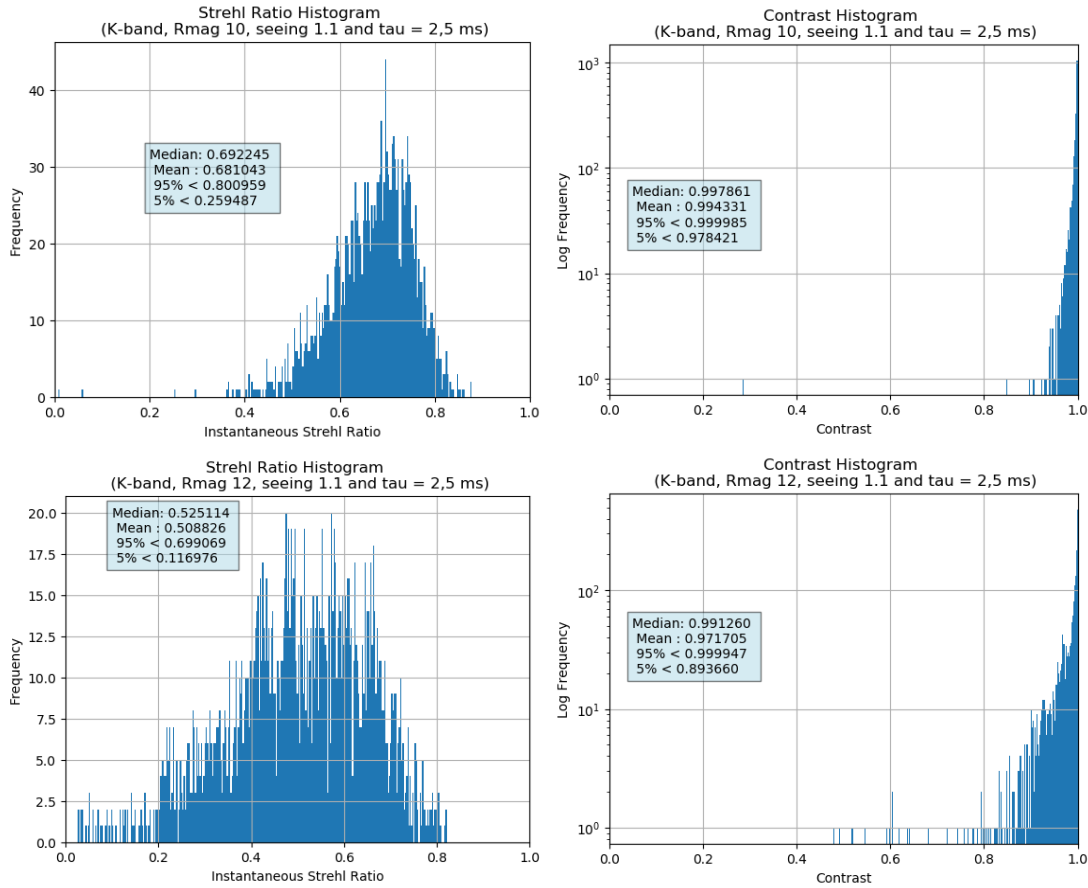


**Figure 5.6:** Instantaneous SR and contrast statistics in K-band under regular sky conditions. Each row corresponds to a different GS R magnitude. *Top:* GS Rmag = 10. *Bottom:* GS Rmag = 12.

(GS R-band < 12 mag), the resulting performance of NAOMI was in good agreement with the expected behaviour from simulations within uncertainties ( $SR \sim 0.5 \pm 0.1$ ). However, our simulations slightly under predict the performance of NAOMI under degraded seeing conditions ( $SR \sim 0.1 \pm 0.1$  with GS R-band < 12 mag), likely by our decision to keep fixed the loop gain and the number of controlled modes in all operation configurations. NAOMI is able to correct the dome seeing observed with low wind conditions and corrects the atmospheric seeing well above  $1.4''$  under the bright regime, improving the SNR of each instrument and significantly reducing the loss of fringes on the Gravity Fringe Tracker (Wuillez et al. 2019). This improvement is only possible for targets that meet the requirement of R-band < 12 mag. However, this translates to a +15% increase in usable time, based on Paranal seeing statistics. At the end of the commissioning in mid November 2018 the ATs were transferred back into

## 5.4. COMMISSIONING AND FINAL RESULTS

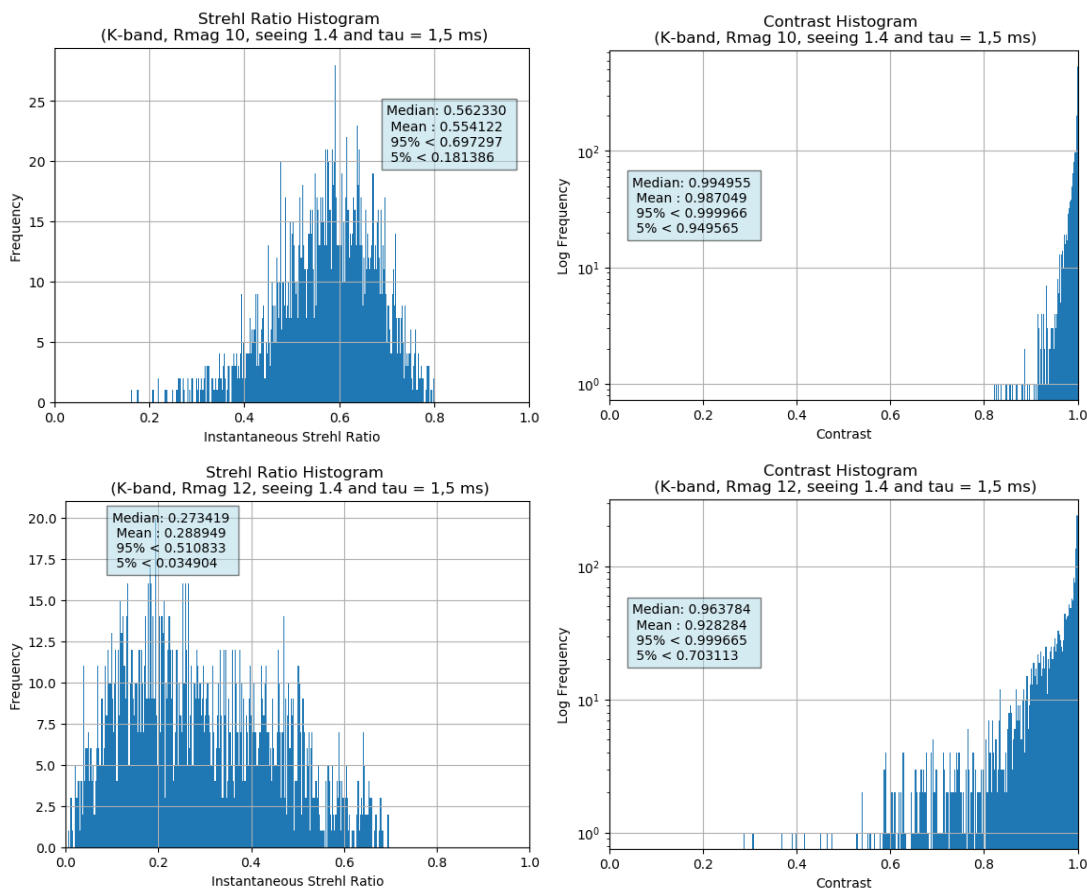


**Figure 5.7:** Instantaneous SR and contrast statistics in K-band under bad sky conditions. Each row corresponds to a different GS R magnitude. *Top:* GS Rmag = 10. *Bottom:* GS Rmag = 12.

science operation. The performances of VLTI instruments with NAOMI are detailed in Woillez et al. (2019).

One important step in the installation of a new instrument is the Science Verification (SV) observations. SV usually happens before the end of the commissioning phase, and always before the instrument is released for regular science operations. These SV observations, proposed by the community via a special call for proposals, have the goal to test and push the instrument to its limits and demonstrate the potential of the new instrument to the community. In that regard, we sent a SV proposal when the call was opened in December 2018, which was accepted with high priority. We proposed the observations of the quadruple system HD 98800, as this system was an interesting challenge for PIONIER aided with NAOMI given the angular separation between each subsystem ( $\sim 0.4''$ , see Fig. 5.8). The results of those SV observations demonstrated the capability of NAOMI to compensate the effect of atmospheric dis-

CHAPTER 5. INSTRUMENTATION

tortion, which led to a better injection of the light in the fibres (more details in Section 3.2.1). These observations, in combination with new PIONIER data (obtained through “regular” open time proposals after the commissioning), led to the work presented in Chapter 3.

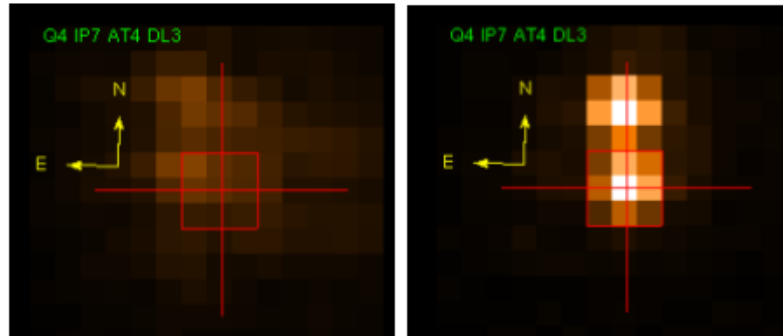


**Figure 5.8:** Infrared Image Sensor (IRIS) capture with and without NAOMI correction in one of our SV observations ( $0.4''$  AaAb-BaBb angular separation) where the upper object correspond to BaBb subsystem. More details in Chapter 3.

## CHAPTER 6

# Summary and conclusions

In this thesis we detected and characterised multiple systems in young associations. The final goal of this dissertation was to determine dynamical masses for multiple systems identified in our sample, specially needed to calibrate PMS isochrones and evolutionary tracks in the low-mas regime.

In the first place we focused on constraining the multiplicity statistics of tight multiple systems. Using high-resolution spectroscopic observations, we identified 68 SB candidates from our sample of 410 objects. Our results hinted at the possibility that the youngest associations have a higher SB fraction. Specifically, we found sensitivity-corrected SB fractions of  $22_{+15}^{-11}\%$  for  $\epsilon$  Cha,  $31_{+16}^{-14}\%$  for TW Hya and  $32_{+9}^{-8}\%$  for  $\beta$  Pictoris, in contrast to the five oldest associations we have studied ( $\sim 35 - 125$  Myr) that yielded levels of  $\sim 10\%$  or lower. We did not find any evidence that these results could have been artificially created by our sensitivity correction approach or the methodology used to asses membership to the associations. We argued that the SB fraction difference could be explained by an evolutionary effect or by non-universal primordial multiplicity properties among the young associations. An evolution of SB fraction with age has been previously proposed for dense environments but the same mechanism (dynamical processing) is very unlikely to operate at low-density environments such as those of the loose associations here studied. Therefore, we favour the non-universal multiplicity properties scenario. In those lines, similar results have

## CHAPTER 6. SUMMARY AND CONCLUSIONS

been found in the ONC (Duchêne et al. 2018) and U Sco (Tokovinin et al. 2020), both regions showing an excess of close companions ( $< 100$  au). These hard binaries are unlikely to be destroyed by dynamical interactions, the authors also favour the idea of these differences arising from lack of universality in the multiple star formation process. The SB candidates of this sample are ideal targets for follow-up campaigns using high-resolution techniques to further confirm multiplicity, resolve orbits, and, in those cases where possible, estimate dynamical masses.

One of the SBs identified in our sample is the quadruple system HD 98800, a member of the  $\sim 10$  Myr old TW Hydrae association (Torres et al. 2008). This system is composed of two SBs orbiting each other (AaAb and BaBb), with a gas-rich disc in polar configuration around BaBb (Kennedy et al. 2019). We obtained new astrometric measurements from long-baseline infrared interferometric observations with the VLTI PIONIER instrument. Combining our new astrometry with archival epochs and radial velocity measurements, we determined the orbital parameters of both subsystems. We refined the orbital solution of BaBb and derived, for the first time, the full orbital solution of AaAb. In addition, by studying the A-B orbit, we confirmed the polar configuration of the circumbinary disk around BaBb. From our analysis, we also inferred the dynamical masses of AaAb ( $M_{Aa} = 0.93 \pm 0.09$  and  $M_{Ab} = 0.29 \pm 0.02 M_{\odot}$ ). These orbital parameters are also relevant to test the long-term stability of the system and to evaluate possible formation scenarios of HD 98800. Using N-body simulations, we showed that the system should be dynamically stable over thousands of orbital periods. Finally, the orbital analysis allowed us to make preliminary predictions for the transit of the disk around BaBb in front of AaAb which is estimated to start around 2026. We explain the lack of a disk around AaAb due to its larger X-Ray luminosity can yield more efficient photoevaporation than in the case of BaBb, as already suggested in Ronco et al. (2021). We concluded the analysis highlighting the need for further high-resolution spectroscopic observations to resolve Aa from Ab and hence provide dynamical masses for those components not-tied by the parallax of B.

We presented our work in progress towards full orbital characterisation and dynamical masses determination for a sample of previously identified close binaries. We collected astrometric measurements for seven binary systems resolved with AO imaging. For these targets, we obtain additional observations with MagAO at LCO. The MagAO observations provided the third epoch of most of the systems. Additionally, we resolved seven binary systems with VLTI PIONIER observations, where three of

them are the inner components of triple hierarchical systems previously identified. These measurements will be used in combination with RV data from literature (when available), to obtain preliminary orbital solutions for the systems that will be used to better plan future observations, that will provide strong constraints on the masses of the components.

Finally, we reported our contribution to the NAOMI commissioning. This work included on-sky performance simulations of the system before the commissioning, to be used as a reference point during the installation in Paranal. During my participation in the commissioning of NAOMI, I could verify that the performance of NAOMI was in good agreement with our simulations for the high Strehl regime (GS R-mag band  $< 12$  mag). Last but not least, we proposed to observe the HD 98800 system for the SV observations of NAOMI. These observations, in combination with new PIONIER data from a regular proposal after commissioning, led to the orbital characterisation of the AaAa and BaBb subsystems of HD 98800 previously mentioned and presented in details in Chapter 3.



# CHAPTER 7

## Future work

The work presented in this thesis can be extended in several directions. In this chapter I present the projects and ideas that I did not have the time to develop in the timeline of my PhD, and other works in progress which were not quite ready for this thesis but should lead to publications in the near future.

### 7.1 Immediate work

#### 7.1.1 Full orbital characterisation of HD 98800

As we discussed in Chap. 3, the orbital solution of HD 98800 could be biased by the blending effect Aa in the BaBb RV measurements. To ensure a reliable orbital solution for both AaAb and BaBb we need to obtain new high resolution spectroscopic observations. In particular for the AaAb binary, new observations could give us the possibility to spectroscopically resolve the Ab component. The RV measurements of the Ab component would allow us to determine the masses and the parallax of AaAb independently of the BaBB parallax solution (an assumption we had to make in Chap. 3). We applied for optical and infrared spectroscopy observing time, with ESPRESSO ( $R \sim 140,000$ , regular open time proposal) and CRIRES+ ( $R \sim 100,000$ , SV proposal) respectively. These proposal were rejected, but given our recently published results

described in Chap. 3, now we should be able to make a stronger submission. The strategy was to resolve spectroscopically, as an SB4, the quadruple system with the resolving power of ESPRESSO, obtaining new RV measurements for each components. On the other hand, taking the most favourable flux ratio of AaAb in the infrared, we will propose to observe this system with CRIRES+ to obtain observations on the Ab component and RV measurements for this component (ideally less influenced by the blended effect). In any case, we still need further analysis on the technical aspects of these observation and estimate when would be the best time window in the orbital phase to maximise the feasibility of our observing goals. We want to maximise the differences in velocities of the components of the systems to improve our chances of seeing as an SB4. In addition to the spectroscopic observations, we have new PIONIER observations scheduled for BaBb in March 2022. These observations will help us to further constrain the inclination and the semi-major axis of BaBb, reducing the uncertainties on these parameters coming from the KI observational limitations and the small phase coverage of the new PIONIER observation. In that regard, the new PIONIER observations are scheduled in a time windows that would complement the previous observations.

### 7.1.2 Dynamical masses for three young hierarchical systems

Three objects with astrometric solution from our PIONIER observations are hierarchical systems with orbital solutions in the literature (see Table 4.2). CD-33 7795 and V 343 Nor are triple systems with an inner period of  $\sim 6$  and  $\sim 5$  years, respectively. Both systems have previous astrometric measurements of their inner system taken with AO-imaging observations but, given the angular resolution constraints, the coverage is limited to the orbital phase when the secondary is more separated to the primary star. Then the semi-major axis, and so the total mass, are less constrained by the orbital solutions. On the other hand, HD 217379 is an SB3 with an orbital solution for both the inner and outer system (Tokovinin 2016a). The inner system has a period of 20.34 days and is not astrometrically resolved. As we saw for the case of HD 988000 in Chapter 3, including the new PIONIER astrometric measurements for the inner orbits of these systems can lead to significant improvement in the orbital and physical parameters. With these new measurement we can recalculate the orbital solution for CD-33 7795 A and V 343 Nor A, and resolve for the first time the inclination for

HD217379A. These new orbital solutions will help us to plan future PIONIER observations. Depending on those solutions, in the worst case scenario for CD-33 7795 A and V 343 Nor A, we will need only a couple of additional observations close to the periastron passage to cover the missing part that the AO-imaging observations could not reach. In the case of HD217379A, we have two observations that should help us to solve for the first time the inclination of the inner binary. Given the short period of this system, it would be possible to reach a good orbital coverage with a couple of PIONIER observations separated by just a few weeks. I plan to propose for those new observations in the next call for proposal or the subsequent one, depending on the preliminary orbital solution results.

### 7.1.3 Towards orbital solution for tight binary candidates

Apart from the multiple systems described above, there are another four tight binary candidates detected with the PIONIER observations (see Table 4.2), where three of them were also flagged as binaries in the SB population update presented in Chapter 2. This means that for these objects we already have a set of RV measurements that can be used in combination with the new astrometry to estimate preliminary orbital solutions. With these results we can better plan future observing campaigns to obtain the astrometric measurements and radial velocities necessary to determine the orbital parameters of these systems. This analysis will not only be beneficial to plan future observations but also to confirm binarity for two high contrast candidates (flux ratio  $\sim 2\%$ ) that presents low significance detection (i.e. the significance that the observation are better described by a binary model than a single star, see Gallenne et al. 2015). Whether the multiplicity nature of those two systems is confirmed or rejected, the new observations will provide valuable information on the sample's multiplicity. For example, to refine the binary fraction presented in Chap. 2, lowering the uncertainties and update the correction factor by including the companion detection probability of the PIONIER observation in the sensitivity maps.

## 7.2 Long-term work

In this section I summarise some long-term projects that can be extended from this thesis work.

### 7.2.1 Determining the periods of spectroscopic binary systems

In the work presented in Chapter 2, we have identified  $\sim 30$  SBs, where  $\sim 70\%$  of them are part of a triple or high-order multiple system. We will propose new spectroscopic observations for these systems that will allow us to confirm the SB fraction showed in chapter 2 and to constrain the SB orbital parameters from the RV measurements. Deriving the orbital parameters of the SB sample will provide crucial upper limits to masses of PMS stars and could either give us insights in the formation and dynamical evolution of the systems that are part of a triple system. Depending on the number and the time span of the RV measurements of each SB candidate, we would need at least one semester to one year of monitoring to obtain our first SB confirmation and, for short period systems, possible preliminary orbital solutions.

### 7.2.2 The SACY sample

The SACY database is the source sample of this thesis work. In Chap. 2 we updated the SB population of young associations and in Chap. 4 we detected new binary candidates in a previously unexplored parameters space using infrared interferometric observations. These observations when combined with the upcoming GAIA DR3 data and the existing data using other observational techniques (e.g., RV, astrometry, etc), would provide new multiplicity constraints on this PMS population of solar-mass stars. The study of these young associations offers the opportunity to derive complete multiplicity statistics for a PMS population across such a wide parameter space. The derived statistics would provide insights into the formation of these nearby, young, low-density associations.

Another future project for our SACY sample is to update the structure of our database and create a web-based service to make the all information more accessible to the community. The idea is to provide the list of the public measurements of each targets, their membership status, and for systems with orbital solution the latest orbital parameters. This should be a great source for future studies in the young asso-

ciations, specially the one related to stellar multiplicity and orbital characterisation.

## 7.3 Collaborations

This section describes future works for which I will contribute as a collaborator but not lead the effort. Those projects are the natural consequences of the work I have been doing during my PhD and the collaborations that I developed at the same time.

### 7.3.1 Disc transit of HD 98800

As discussed in Chap. 3, the orbital parameters of AB strongly suggest that the BaBb pair and its disk will pass in front of the AaAb system, starting sometime in 2026 (depending on the solution used for AB). This presents a unique opportunity to observe and characterise the properties of the dust and gas disk via photometric (and spectroscopic) monitoring of the whole system. The development and the plan of these future observations will be evaluated in the upcoming years. This idea was first mentioned in Kennedy et al. (2019).

### 7.3.2 SPECULOOS

After my thesis defence I will start a postdoc position in the SPECULOOS project. The aim of the SPECULOOS project is look for transit planets at nearest ( $< 40$  pc) ultra-cool ( $< 3000\text{K}$ ) dwarf stars, based on a network of robotic 1 m telescopes especially designed for this survey (Sebastian et al. 2021). The potential collaboration with this project would be related with the extra scientific output of this survey that is activity, flares (complement with X-ray archives) and rotational periods. By cross-matching our SACY database with the SPECULOOS targets, we could analyse the rotational period information of this sub-sample. Given the characteristic of the SPECULOOS targets (spectral type M7 and later) is expected a low detection ratio of binary systems, however there is still an opportunity to characterise new eclipsing binaries using the tools developed for our work on HD 98800 presented in Chap. 3.



# APPENDIX A

## Appendix

### A.1 Publications related with this thesis

#### A.1.1 Refereed

S. Zúñiga-Fernández, J. Olofsson, A. Bayo, X. Haubois, J. M. Corral-Santana, A. Lopera-Mejía, M. P. Ronco, A. Tokovinin, A. Gallenne, G. M. Kennedy, and J. -P. Berger, “The HD 98800 quadruple pre-main sequence system. Towards full orbital characterisation using long-baseline infrared interferometry”, *A&A*, 655, A15, (2021) - 2021A&A...655A..15Z

S. Zúñiga-Fernández, A. Bayo, P. Elliott, C. Zamora, G. Corvalán, X. Haubois, J. M. Corral-Santana, J. Olofsson, N. Huélamo, M. F. Sterzik, C. A. O. Torres, G. R. Quast, and C. H. F. Melo, “Search for associations containing young stars (SACY). VIII. An updated census of spectroscopic binary systems exhibiting hints of non-universal multiplicity among their associations”, *A&A*, 645, A30, (2021) - 2021A&A...645A..30Z

J. Woillez, J. A. Abad, , (80 more co-authors), and S. Zúñiga-Fernández, “NAOMI: the adaptive optics system of the Auxiliary Telescopes of the VLTI”, *A&A*, 629, A41, (2019) - 2019A&A...629A..41W

## A.1.2 Conference and Meeting proceedings

N. Soto, C. Lobos, P. Mardones, A. Bayo, C. Rozas, S. Castillo, G. Hamilton, L. Pedrero, S. Zúñiga-Fernández, K. Maucó, H. Hakobyan, C. García, M. R. Schreiber, and W. Brooks, "Quality control of the CFRP mirror manufacturing process at NPF", SPIE, 11451, 114512I, (2020) - 2020SPIE11451E..2IS

A. Bayo, P. Mardones, S. Castillo, G. Hamilton, C. Lobos, L. Pedrero, C. Rozas, N. Soto, H. Hakobyan, C. García, M. R. Schreiber, W. Brooks, and S. Zúñiga-Fernández, "NPF update: light-weight mirror development in Chile", SPIE, 11451, 114510J, (2020) - 2020SPIE11451E..0JB

John D. Monnier, Michael Ireland, Stefan Kraus, Almudena Alonso-Herrero, Amy Bonsor, Fabien Baron, Amelia Bayo, Jean-Philippe Berger, (68 more co-authors), and Sebastián Zúñiga-Fernández, "Planet formation imager: project update", SPIE, 10701, 1070118, (2018) - 2018SPIE10701E..18M

Sebastián Zúñiga-Fernández, Maja Vučković, Nikolaus Vogt, Omar Cuevas, and Yerko Chacon, "Revival of an abandoned telescope: the Boller and Chivens Bochum 0.61-metre telescope of Universidad de Valparaiso", SPIE, 10700, 107002X, (2018) - 2018SPIE10700E..2XZ

Sebastián Zúñiga-Fernández, Amelia Bayo, Johan Olofsson, Leslie Pedrero, Claudio Lobos, Elias Rozas, Nicolás. Soto, Matthias Schreiber, Pedro Escárate, Christian Romero, Hayk Hakobyan, Jorge Cuadra, Cristopher Rozas, John D. Monnier, Stefan Kraus, Mike J. Ireland, and Pedro Mardones, "NPF: mirror development in Chile", SPIE, 10700, 107003X, (2018) - 2018SPIE10700E..3XZ

# Bibliography

- Allard, F., Homeier, D., Freytag, B., et al. 2013, *Memorie della Societa Astronomica Italiana Supplementi*, 24, 128
- Aller, A., Lillo-Box, J., Jones, D., Miranda, L. F., & Barceló Forteza, S. 2020, *A&A*, 635, A128
- ALMA Partnership, Brogan, C. L., Pérez, L. M., et al. 2015, *ApJ*, 808, L3
- Aly, H., Dehnen, W., Nixon, C., & King, A. 2015, *Monthly Notices of the Royal Astronomical Society*, 449, 65
- Aly, H., Lodato, G., & Cazzoletti, P. 2018, *MNRAS*, 480, 4738
- Appenzeller, I. & Mundt, R. 1989, *A&A Rev.*, 1, 291
- Asplund, M., Grevesse, N., Sauval, A. J., & Scott, P. 2009, *ARA&A*, 47, 481
- Bailey, J. I., White, R. J., Blake, C. H., et al. 2012, *ApJ*, 749, 16
- Baraffe, I., Homeier, D., Allard, F., & Chabrier, G. 2015, *A&A*, 577, A42
- Baranne, A., Queloz, D., Mayor, M., et al. 1996, *A&AS*, 119, 373
- Bate, M. R. 2019, *MNRAS*, 484, 2341
- Bate, M. R., Bonnell, I. A., & Bromm, V. 2002, *Monthly Notices of the Royal Astronomical Society*, 336, 705
- Berger, J. P. & Segransan, D. 2007, *New Astronomy Reviews*, 51, 576, observation and Data Reduction with the VLT Interferometer
- Bergin, E. A. & Tafalla, M. 2007, *ARA&A*, 45, 339

## BIBLIOGRAPHY

- Blitz, L., Fukui, Y., Kawamura, A., et al. 2007, in *Protostars and Planets V*, ed. B. Reipurth, D. Jewitt, & K. Keil, 81
- Boden, A. F., Sargent, A. I., Akeson, R. L., et al. 2005, *ApJ*, 635, 442
- Bodenheimer, P. 1978, *ApJ*, 224, 488
- Boisse, I., Eggenberger, A., Santos, N., et al. 2010, *Åp*, 523, A88
- Bonaccini, D., Gallieni, D., Biasi, R., et al. 1997, in *Society of Photo-Optical Instrumentation Engineers (SPIE) Conference Series*, Vol. 3126, *Adaptive Optics and Applications*, ed. R. K. Tyson & R. Q. Fugate, 580
- Bonneau, D., Clausse, J. M., Delfosse, X., et al. 2006, *A&A*, 456, 789
- Bonneau, D., Delfosse, X., Mourard, D., et al. 2011, *A&A*, 535, A53
- Bonnefoy, M., Chauvin, G., Dumas, C., et al. 2009, *A&A*, 506, 799
- Bonnell, I. A. & Bate, M. R. 1994, *Monthly Notices of the Royal Astronomical Society*, 271, 999
- Boss, A. P. 1986, *ApJS*, 62, 519
- Bouchy, F., Hébrard, G., Udry, S., et al. 2009, *A&A*, 505, 853
- Braun, T. A. M., Yen, H.-W., Koch, P. M., et al. 2021, *ApJ*, 908, 46
- Briceño, C., Luhman, K. L., Hartmann, L., Stauffer, J. R., & Kirkpatrick, J. D. 2002, *ApJ*, 580, 317
- Burgasser, A. J., Kirkpatrick, J. D., Reid, I. N., et al. 2003, *The Astrophysical Journal*, 586, 512
- Caffau, E., Ludwig, H. G., Steffen, M., Freytag, B., & Bonifacio, P. 2011, *Sol. Phys.*, 268, 255
- Chauvin, G., Vigan, A., Bonnefoy, M., et al. 2015, *A&A*, 573, A127
- Chelli, A., Duvert, G., Bourguès, L., et al. 2016, *A&A*, 589, A112
- Chen, X., Arce, H. G., Zhang, Q., et al. 2013, *ApJ*, 768, 110
- Cincotta, P. M. & Simó, C. 2000, *A&AS*, 147, 205

- Clark Cunningham, J.-M., Felix, D. L., Dixon, D. M., et al. 2020, arXiv e-prints, arXiv:2009.03872
- Close, L., Lenzen, R., C Guirado, J., et al. 2005, *Nature*, 433, 286
- Close, L. M., Males, J. R., Kopon, D. A., et al. 2012, in Society of Photo-Optical Instrumentation Engineers (SPIE) Conference Series, Vol. 8447, Adaptive Optics Systems III, ed. B. L. Ellerbroek, E. Marchetti, & J.-P. Véran, 84470X
- Connelley, M. S., Reipurth, B., & Tokunaga, A. T. 2008, *AJ*, 135, 2526
- Cuello, N. & Giuppone, C. A. 2019, *A&A*, 628, A119
- Cutispoto, G., Pastori, L., Pasquini, L., et al. 2002, *A&A*, 384, 491
- Czekala, I., Chiang, E., Andrews, S. M., et al. 2019, *The Astrophysical Journal*, 883, 22
- Czekala, I., Ribas, Á., Cuello, N., et al. 2021, *ApJ*, 912, 6
- Daemgen, S., Bonavita, M., Jayawardhana, R., Lafrenière, D., & Janson, M. 2015, *ApJ*, 799, 155
- Dall, T. H., Santos, N. C., Arentoft, T., Bedding, T. R., & Kjeldsen, H. 2006, *A&A*, 454, 341
- De Furio, M., Reiter, M., Meyer, M. R., et al. 2019, *ApJ*, 886, 95
- de la Reza, R., Torres, C. A. O., Quast, G., Castilho, B. V., & Vieira, G. L. 1989, *ApJ*, 343, L61
- Dekker, H., D’Odorico, S., Kaufer, A., Delabre, B., & Kotzlowski, H. 2000, in Society of Photo-Optical Instrumentation Engineers (SPIE) Conference Series, Vol. 4008, Optical and IR Telescope Instrumentation and Detectors, ed. M. Iye & A. F. Moorwood, 534–545
- Delfosse, X., Forveille, T., Beuzit, J.-L., et al. 1999, *A&A*, 344, 897
- Desidera, S., Covino, E., Messina, S., et al. 2015, *A&A*, 573, A126
- Desort, M., Lagrange, A.-M., Galland, F., Udry, S., & Mayor, M. 2007, *A&A*, 473, 983
- Douglas, S. T., Agüeros, M. A., Covey, K. R., et al. 2016, *ApJ*, 822, 47

## BIBLIOGRAPHY

- Douglass, G. G. & Worley, C. E. 1992, in *Astronomical Society of the Pacific Conference Series*, Vol. 32, IAU Colloq. 135: Complementary Approaches to Double and Multiple Star Research, ed. H. A. McAlister & W. I. Hartkopf, 311
- Duchêne, G., Bontemps, S., Bouvier, J., et al. 2007, *A&A*, 476, 229
- Duchêne, G. & Kraus, A. 2013, *ARA&A*, 51, 269
- Duchêne, G., Lacour, S., Moraux, E., Goodwin, S., & Bouvier, J. 2018, *MNRAS*, 478, 1825
- Dunham, M. M., Stutz, A. M., Allen, L. E., et al. 2014, in *Protostars and Planets VI*, ed. H. Beuther, R. S. Klessen, C. P. Dullemond, & T. Henning, 195
- Duquennoy, A. & Mayor, M. 1991, *A&A*, 500, 337
- Eggleton, P. P. 2009, *MNRAS*, 399, 1471
- Elliott, P. & Bayo, A. 2016, *Monthly Notices of the Royal Astronomical Society*, 459, 4499
- Elliott, P., Bayo, A., Melo, C. H. F., et al. 2014, *A&A*, 568, A26
- Elliott, P., Bayo, A., Melo, C. H. F., et al. 2016a, *A&A*, 590, A13
- Elliott, P., Huélamo, N., Bouy, H., et al. 2015, *A&A*, 580, A88
- Elmegreen, B. G. 1997, *ApJ*, 486, 944
- Farago, F. & Laskar, J. 2010, *MNRAS*, 401, 1189
- Feiden, G. A. 2016, *A&A*, 593, A99
- Fekel, F. C., J. 1981, *ApJ*, 246, 879
- Fischer, D. A. & Marcy, G. W. 1992, *ApJ*, 396, 178
- Flagg, L., Shkolnik, E. L., Weinberger, A., et al. 2020, arXiv e-prints, arXiv:2007.15799
- Flores, C., Connelley, M. S., Reipurth, B., & Duchêne, G. 2021, arXiv e-prints, arXiv:2111.03957
- Foreman-Mackey, D., Luger, R., Czekala, I., et al. 2020, *exoplanet-dev/exoplanet v0.4.0*

- Freedman, D. & Diaconis, P. 1981, *Zeitschrift fur Wahrscheinlichkeitstheorie und Verwandte Gebiete*, 57, 453
- Gagné, J., Mamajek, E. E., Malo, L., et al. 2018a, *ApJ*, 856, 23
- Gaia Collaboration, Brown, A. G. A., Vallenari, A., et al. 2021, *A&A*, 649, A1
- Gaia Collaboration, Brown, A. G. A., Vallenari, A., et al. 2018, *A&A*, 616, A1
- Gaia Collaboration, Prusti, T., de Bruijne, J. H. J., et al. 2016, *A&A*, 595, A1
- Galicher, R., Marois, C., Macintosh, B., et al. 2016, *A&A*, 594, A63
- Gallenne, A., Mérand, A., Kervella, P., et al. 2015, *A&A*, 579, A68
- Gallenne, A., Pietrzyński, G., Graczyk, D., et al. 2018, *A&A*, 616, A68
- Gallenne, A., Pietrzyński, G., Graczyk, D., et al. 2019, *A&A*, 632, A31
- Ghez, A. M., McCarthy, D. W., Patience, J. L., & Beck, T. L. 1997, *The Astrophysical Journal*, 481, 378
- Giuppone, C. A. & Cuello, N. 2019, in *Journal of Physics Conference Series*, Vol. 1365, *Journal of Physics Conference Series*, 012023
- Gontcharov, G. A. 2006, *Astronomy Letters*, 32, 759
- Grandjean, A., Lagrange, A. M., Keppler, M., et al. 2020, *A&A*, 633, A44
- Gravity Collaboration, Eupen, F., Labadie, L., et al. 2021, *A&A*, 648, A37
- Gray, D. F. 1976, *The observation and analysis of stellar photospheres*
- Greene, T. 2001, *American Scientist*, 89, 316
- Griffin, R. F. 2010, *The Observatory*, 130, 125
- Guieu, S., Dougados, C., Monin, J.-L., Magnier, E., & Martín, E. L. 2006, *A&A*, 446, 485
- Haguenauer, P., Abuter, R., Alonso, J., et al. 2008, in *Optical and Infrared Interferometry*, ed. M. Schöller, W. C. Danchi, & F. Delplancke, Vol. 7013, *International Society for Optics and Photonics (SPIE)*, 141 – 149
- Halbwachs, J. L. 1986, *A&A*, 168, 161

## BIBLIOGRAPHY

- Hamers, A. S., Rantala, A., Neunteufel, P., Preece, H., & Vynatheya, P. 2021, *MNRAS*, 502, 4479
- Haubois, X., Abuter, R., Aller-Carpentier, E., et al. 2020, in *Optical and Infrared Interferometry and Imaging VII*, ed. P. G. Tuthill, A. Mérand, & S. Sallum, Vol. 11446, International Society for Optics and Photonics (SPIE), 26 – 35
- Hayashi, C. 1961, *PASJ*, 13, 450
- Henry, T. J. & McCarthy, Donald W., J. 1993, *AJ*, 106, 773
- Hilditch, R. W. 2001, *An Introduction to Close Binary Stars*
- Hinse, T. C., Christou, A. A., Alvarelos, J. L. A., & Goździewski, K. 2010, *MNRAS*, 404, 837
- Hirsch, L. A., Rosenthal, L., Fulton, B. J., et al. 2021, *The Astronomical Journal*, 161, 134
- Howell, S. B., Sobek, C., Haas, M., et al. 2014, *PASP*, 126, 398
- Huber, P. J. 1964, *Ann. Math. Statist.*, 35, 73
- Hummel, C. A., Le Bouquin, J.-B., & Merand, A. 2016, in *Society of Photo-Optical Instrumentation Engineers (SPIE) Conference Series*, Vol. 9907, *Optical and Infrared Interferometry and Imaging V*, ed. F. Malbet, M. J. Creech-Eakman, & P. G. Tuthill, 99073B
- Ivezić, Ž., Connelly, A. J., VanderPlas, J. T., & Gray, A. 2014, *Statistics, Data Mining, and Machine Learning in Astronomy*
- Jaehnig, K., Bird, J. C., Stassun, K. G., et al. 2017, *The Astrophysical Journal*, 851, 14
- Janson, M., Durkan, S., Hippler, S., et al. 2017, *A&A*, 599, A70
- Johnson-Groh, M., Marois, C., Rosa, R. J. D., et al. 2017, *The Astronomical Journal*, 153, 190
- Joncour, I., Duchêne, Gaspard, & Moraux, Estelle. 2017, *A&A*, 599, A14
- Kastner, J. H., Huenemoerder, D. P., Schulz, N. S., et al. 2004, *ApJ*, 605, L49
- Kastner, J. H., Zuckerman, B., Weintraub, D. A., & Forveille, T. 1997, *Science*, 277, 67

- Katz, D., Sartoretti, P., Cropper, M., et al. 2018, *A&A*, 622, A205
- Kaufer, A., Stahl, O., Tubbesing, S., et al. 1999, *The Messenger*, 95, 8
- Kennedy, G. M., Matrà, L., Facchini, S., et al. 2019, *Nature Astronomy*, 3, 230
- Keppler, M., Benisty, M., Müller, A., et al. 2018, *A&A*, 617, A44
- Kervella, P., Mérand, A., Gallenne, A., et al. 2017, in *European Physical Journal Web of Conferences*, Vol. 152, *European Physical Journal Web of Conferences*, 07002
- King, R. R., Goodwin, S. P., Parker, R. J., & Patience, J. 2012, *MNRAS*, 427, 2636
- Kiselev, A. A. & Kiyeva, O. V. 1980, *AZh*, 57, 1227
- Klüter, J., Bastian, U., & Wambsganss, J. 2020, *A&A*, 640, A83
- Köhler, R., Petr-Gotzens, M. G., McCaughrean, M. J., et al. 2006, *A&A*, 458, 461
- Köhler, R., Ratzka, T., Petr-Gotzens, M. G., & Correia, S. 2013, *A&A*, 558, A80
- Konopacky, Q. M., Ghez, A. M., Duchêne, G., McCabe, C., & Macintosh, B. A. 2007, *AJ*, 133, 2008
- Kounkel, M. & Covey, K. 2019, *AJ*, 158, 122
- Kouwenhoven, M. B. N. 2006, PhD thesis, -
- Kouwenhoven, M. B. N., Brown, A. G. A., Portegies Zwart, S. F., & Kaper, L. 2007, *A&A*, 474, 77
- Kozai, Y. 1962, *AJ*, 67, 591
- Kratter, K. & Lodato, G. 2016, *ARA&A*, 54, 271
- Kratter, K. M., Murray-Clay, R. A., & Youdin, A. N. 2010, *ApJ*, 710, 1375
- Kraus, A. L. & Ireland, M. J. 2012, *ApJ*, 745, 5
- Kraus, A. L., Ireland, M. J., Martinache, F., & Hillenbrand, L. A. 2011, *The Astrophysical Journal*, 731, 8
- Kraus, A. L., Shkolnik, E. L., Allers, K. N., & Liu, M. C. 2014, *The Astronomical Journal*, 147, 146

## *BIBLIOGRAPHY*

- Kraus, S., Kreplin, A., Young, A. K., et al. 2020, *Science*, 369, 1233
- Lagrange, A.-M., Meunier, N., Chauvin, G., et al. 2013, *A&A*, 559, A83
- Larson, R. B. 1969, *Monthly Notices of the Royal Astronomical Society*, 145, 271
- Larson, R. B. 1985, *MNRAS*, 214, 379
- Laskar, T., Soderblom, D. R., Valenti, J. A., & Stauffer, J. R. 2009, *ApJ*, 698, 660
- Lawson, P. R. 2000, *Principles of Long Baseline Stellar Interferometry*
- Le Bouquin, J. B. & Absil, O. 2012, *A&A*, 541, A89
- Le Bouquin, J. B., Berger, J. P., Lazareff, B., et al. 2011, *A&A*, 535, A67
- Lee, A. T., Offner, S. S. R., Kratter, K. M., Smullen, R. A., & Li, P. S. 2019, *ApJ*, 887, 232
- Lee, J. & Song, I. 2019, *MNRAS*, 489, 2189
- Lee, J.-E., Lee, S., Dunham, M. M., et al. 2017, *Nature Astronomy*, 1, 0172
- Lidov, M. 1962, *Planetary and Space Science*, 9, 719
- Lindgren, L. & Dravins, D. 2003, *A&A*, 401, 1185
- Lindgren, L., Hernández, J., Bombrun, A., et al. 2018, *A&A*, 616, A2
- Lopez-Santiago, J., Montes, D., Crespo-Chacon, I., & Fernandez-Figueroa, M. J. 2006, *The Astrophysical Journal*, 643, 1160
- Macintosh, B., Max, C., Zuckerman, B., et al. 2001, in *Astronomical Society of the Pacific Conference Series*, Vol. 244, *Young Stars Near Earth: Progress and Prospects*, ed. R. Jayawardhana & T. Greene, 309
- Maldonado, J., Martínez-Arnáiz, R. M., Eiroa, C., Montes, D., & Montesinos, B. 2010, *A&A*, 521, A12
- Malkov, O. Y. 2007, *MNRAS*, 382, 1073
- Malkov, O. Y., Tamazian, V. S., Docobo, J. A., & Chulkov, D. A. 2012, *A&A*, 546, A69
- Malo, L., Artigau, É., Doyon, R., et al. 2014, *The Astrophysical Journal*, 788, 81

- Mamajek, E. E. & Feigelson, E. D. 2001, in *Astronomical Society of the Pacific Conference Series*, Vol. 244, *Young Stars Near Earth: Progress and Prospects*, ed. R. Jayawardhana & T. Greene, 104–115
- Mann, A. W., Newton, E. R., Rizzuto, A. C., et al. 2016, *AJ*, 152, 61
- Marrese, P. M., Marinoni, S., Fabrizio, M., & Altavilla, G. 2021, *Gaia EDR3 documentation Chapter 9: Cross-match with external catalogues*, *Gaia EDR3 documentation*
- Martin, R. G. & Lubow, S. H. 2019, *MNRAS*, 490, 1332
- Mason, B. D., Wycoff, G. L., Hartkopf, W. I., Douglass, G. G., & Worley, C. E. 2001, *AJ*, 122, 3466
- Mathieu, R. D., Baraffe, I., Simon, M., Stassun, K. G., & White, R. 2007, in *Protostars and Planets V*, ed. B. Reipurth, D. Jewitt, & K. Keil, 411
- Maury, A. J., André, P., Hennebelle, P., et al. 2010, *A&A*, 512, A40
- Mayor, M., Pepe, F., Queloz, D., et al. 2003, *The Messenger*, 114, 20
- Melo, C. H. F. 2003, *A&A*, 410, 269
- Melo, C. H. F., Pasquini, L., & De Medeiros, J. R. 2001, *A&A*, 375, 851
- Merle, T., der Swaelmen, M. V., Eck, S. V., et al. 2020, *The Gaia-ESO Survey: detection and characterization of single line spectroscopic binaries*
- Mochnacki, S. W., Gladders, M. D., Thomson, J. R., et al. 2002, *The Astronomical Journal*, 124, 2868
- Moe, M. & Di Stefano, R. 2017, *ApJS*, 230, 15
- Molinari, S., Bally, J., Glover, S., et al. 2014, in *Protostars and Planets VI*, ed. H. Beuther, R. S. Klessen, C. P. Dullemond, & T. Henning, 125
- Monnier, J. D. 2003, *Reports on Progress in Physics*, 66, 789
- Montes, D., López-Santiago, J., Fernández-Figueroa, M. J., & Gálvez, M. C. 2001, *A&A*, 379, 976
- Moór, A., Szabó, G., Kiss, L., et al. 2013, *Monthly Notices of the Royal Astronomical Society*, 435, 1376

## BIBLIOGRAPHY

- Moraux, E. 2016, in EAS Publications Series, Vol. 80-81, EAS Publications Series, 73–114
- Moultaka, J., Ilovaisky, S., Prugniel, P., & Soubiran, C. 2004, Publications of the Astronomical Society of the Pacific, 116, 693
- Murphy, S. J., Lawson, W. A., & Bento, J. 2015, Monthly Notices of the Royal Astronomical Society, 453, 2220
- Murray, C. D. & Correia, A. C. M. 2010, Keplerian Orbits and Dynamics of Exoplanets, ed. S. Seager, 15–23
- Natta, A., Testi, L., & Randich, S. 2006, A&A, 452, 245
- Nguyen, D. C., Brandeker, A., van Kerkwijk, M. H., & Jayawardhana, R. 2012, The Astrophysical Journal, 745, 119
- Nielsen, E., Close, L., Guirado, J., et al. 2005, Astronomische Nachrichten, 326, 1033
- Nielsen, E. L., Rosa, R. J. D., Wang, J., et al. 2016, The Astronomical Journal, 152, 175
- Nordstrom, B., Olsen, E. H., Andersen, J., Mayor, M., & Pont, F. 1996, in Astronomical Society of the Pacific Conference Series, Vol. 112, The History of the Milky Way and Its Satellite System, ed. A. Burkert, D. H. Hartmann, & S. A. Majewski, 145
- Paczynski, B. 1991, ApJ, 371, L63
- Paczynski, B. 1996, ARA&A, 34, 419
- Pegues, J., Czekala, I., Andrews, S. M., et al. 2021, ApJ, 908, 42
- Pietrinferni, A., Cassisi, S., Salaris, M., & Castelli, F. 2004, ApJ, 612, 168
- Piskunov, A. E., Schilbach, E., Kharchenko, N. V., Röser, S., & Scholz, R. D. 2007, A&A, 468, 151
- Pourbaix, D. 1998, A&AS, 131, 377
- Povich, M. S., Giampapa, M. S., Valenti, J. A., et al. 2001, The Astronomical Journal, 121, 1136
- Prato, L., Ghez, A. M., Piña, R. K., et al. 2001, ApJ, 549, 590

- Queloz, D. 1995, Symposium - International Astronomical Union, 167, 221–229
- Queloz, D., Henry, G. W., Sivan, J. P., et al. 2001, *A&A*, 379, 279
- Queloz, D. and Allain, S., Mermilliod, J.-C., Bouvier, J., & Mayor, M. 1998, *A&A*, 335, 183
- R. Quast, G., A. O. Torres, C., Reza, R., da Silva, L., & Mayor, M. 2000, Proceedings of the International Astronomical Union, 200, 28P
- Raghavan, D., McAlister, H. A., Henry, T. J., et al. 2010, *The Astrophysical Journal Supplement Series*, 190, 1
- Rein, H. & Liu, S. F. 2012, *A&A*, 537, A128
- Rein, H. & Spiegel, D. S. 2015, *MNRAS*, 446, 1424
- Rein, H. & Tamayo, D. 2015, *MNRAS*, 452, 376
- Reiners, A. & Basri, G. 2009, *The Astrophysical Journal*, 705, 1416
- Reipurth, B., Clarke, C. J., Boss, A. P., et al. 2014, in *Protostars and Planets VI*, ed. H. Beuther, R. S. Klessen, C. P. Dullemond, & T. Henning, 267
- Reipurth, B. & Mikkola, S. 2012, *Nature*, 492, 1476
- Ribas, Á., Macías, E., Espaillat, C. C., & Duchêne, G. 2018, *ApJ*, 865, 77
- Ricker, G. R., Winn, J. N., Vanderspek, R., et al. 2015, *Journal of Astronomical Telescopes, Instruments, and Systems*, 1, 014003
- Riedel, A. R., Finch, C. T., Henry, T. J., et al. 2014, *AJ*, 147, 85
- Rizzuto, A. C., Dupuy, T. J., Ireland, M. J., & Kraus, A. L. 2020, *ApJ*, 889, 175
- Rizzuto, A. C., Ireland, M. J., Dupuy, T. J., & Kraus, A. L. 2016, *ApJ*, 817, 164
- Roddier, F. 1981, *Progress in Optics*, 19, 281
- Rodet, L., Bonnefoy, M., Durkan, S., et al. 2018, *A&A*, 618, A23
- Rodriguez, D. R., Zuckerman, B., Kastner, J. H., et al. 2013, *The Astrophysical Journal*, 774, 101

## *BIBLIOGRAPHY*

- Ronco, M. P., Guilera, O. M., Cuadra, J., et al. 2021, *The Astrophysical Journal*, 916, 113
- Ryu, T., Leigh, N. W. C., & Perna, R. 2017, *MNRAS*, 467, 4447
- Sahu, K. C., Anderson, J., Casertano, S., et al. 2017, *Science*, 356, 1046
- Salvatier, J., Wiecki, T. V., & Fonnesbeck, C. 2016, *PeerJ Computer Science*, 2, e55
- Sana, H., de Mink, S. E., de Koter, A., et al. 2012, *Science*, 337, 444
- Sartoretti, P., Katz, D., Cropper, M., et al. 2018, *A&A*, 616, A6
- Sato, B., Fischer, D. A., Ida, S., et al. 2009, *The Astrophysical Journal*, 703, 671
- Schlieder, J. E., Lépine, S., & Simon, M. 2012, *The Astronomical Journal*, 144, 109
- Schneider, A. C., Shkolnik, E. L., Allers, K. N., et al. 2019, *AJ*, 157, 234
- Scott, D. W. 1979, *Biometrika*, 66, 605
- Sebastian, D., Gillon, M., Ducrot, E., et al. 2021, *A&A*, 645, A100
- Shan, Y., Yee, J. C., Bowler, B. P., et al. 2017, *ApJ*, 846, 93
- Sheehan, P. D., Wu, Y.-L., Eisner, J. A., & Tobin, J. J. 2019, 874, 136
- Shkolnik, E. L., Anglada-Escudé, G., Liu, M. C., et al. 2012, *The Astrophysical Journal*, 758, 56
- Shkolnik, E. L., Hebb, L., Liu, M. C., Reid, I. N., & Cameron, A. C. 2010, *The Astrophysical Journal*, 716, 1522
- Shu, F. H., Adams, F. C., & Lizano, S. 1987, *ARA&A*, 25, 23
- Simon, M., Guilloteau, S., Beck, T. L., et al. 2019, *ApJ*, 884, 42
- Simon, M. & Prato, L. 2019, *Research Notes of the American Astronomical Society*, 3, 186
- Skinner, C. J., Barlow, M. J., & Justtanont, K. 1992, *MNRAS*, 255, 31P
- Sperauskas, J., Deveikis, V., & Tokovinin, A. 2019, *A&A*, 626, A31
- Stassun, K. G., Feiden, G. A., & Torres, G. 2014, *New Astronomy Reviews*, 60, 1

- Stassun, K. G., Oelkers, R. J., Paegert, M., et al. 2019, *The Astronomical Journal*, 158, 138
- Sterzik, M. F. & Tokovinin, A. A. 2002, *A&A*, 384, 1030
- Sturges, H. A. 1926, *Journal of the American Statistical Association*, 21, 65
- Susemihl, N. & Meyer, M. R. 2021, arXiv e-prints, arXiv:2109.05951
- Tobin, J., Sheehan, P., & Johnstone, D. 2018a, arXiv e-prints, arXiv:1810.06590
- Tobin, J. J., Looney, L. W., Li, Z.-Y., et al. 2016, *ApJ*, 818, 73
- Tobin, J. J., Looney, L. W., Li, Z.-Y., et al. 2018b, *ApJ*, 867, 43
- Tokovinin, A. 2008, *MNRAS*, 389, 925
- Tokovinin, A. 2014a, *The Astronomical Journal*, 147, 86
- Tokovinin, A. 2014b, *The Astronomical Journal*, 147, 87
- Tokovinin, A. 2016a, *AJ*, 152, 11
- Tokovinin, A. 2018a, *AJ*, 155, 160
- Tokovinin, A. 2018b, *PASP*, 130, 035002
- Tokovinin, A. 2018c, *ApJS*, 235, 6
- Tokovinin, A. 2019, arXiv e-prints, arXiv:1910.04143
- Tokovinin, A. 2020a, *AJ*, 159, 265
- Tokovinin, A. 2020b, *Astronomy Letters*, 46, 612
- Tokovinin, A. 2021, *Universe*, 7
- Tokovinin, A. & Briceno, C. 2019, arXiv e-prints, arXiv:1909.12700
- Tokovinin, A., Fischer, D. A., Bonati, M., et al. 2013, *PASP*, 125, 1336
- Tokovinin, A. & Horch, E. P. 2016, *The Astronomical Journal*, 152, 116
- Tokovinin, A., Mason, B. D., & Hartkopf, W. I. 2014, *AJ*, 147, 123
- Tokovinin, A. & Moe, M. 2020, *MNRAS*, 491, 5158

## BIBLIOGRAPHY

- Tokovinin, A., Petr-Gotzens, M. G., & Briceño, C. 2020, *AJ*, 160, 268
- Tokovinin, A., Thomas, S., Sterzik, M., & Udry, S. 2006, *A&A*, 450, 681
- Tokovinin, A. A. 1999, *Astronomy Letters*, 25, 669
- Torres, C. A. O., Quast, G. R., da Silva, L., et al. 2006, *A&A*, 460, 695
- Torres, C. A. O., R. Quast, G., Melo, C., & F. Sterzik, M. 2008, *Handbook of Star Forming Regions*, Vol. 2, 757
- Torres, G., Andersen, J., & Giménez, A. 2010, *A&A Rev.*, 18, 67
- Torres, G., Henry, T. J., Franz, O. G., & Wasserman, L. H. 1999, *The Astronomical Journal*, 117, 562
- Torres, G., Stefanik, R. P., Latham, D. W., & Mazeh, T. 1995, *ApJ*, 452, 870
- van Leeuwen, F. 2007, *A&A*, 474, 653
- VanderPlas, J. T. & Ivezić, Z. 2015, *The Astrophysical Journal*, 812, 18
- Vaytet, N., Audit, E., Chabrier, G., Commerçon, B., & Masson, J. 2012, *A&A*, 543, A60
- Vázquez-Semadeni, E., Palau, A., Ballesteros-Paredes, J., Gómez, G. C., & Zamora-Avilés, M. 2019, *MNRAS*, 490, 3061
- Verrier, P. E. & Evans, N. W. 2008, *MNRAS*, 390, 1377
- Viana Almeida, P., Melo, C., Santos, N. C., et al. 2012, *A&A*, 539, A62
- Wang, J. & Zhong, Z. 2018, *A&A*, 619, L1
- Ward-Duong, K., Patience, J., De Rosa, R. J., et al. 2015, *MNRAS*, 449, 2618
- Webb, R. A., Zuckerman, B., Platais, I., et al. 1999, *The Astrophysical Journal*, 512, L63
- Whitworth, A. P. 2001, *Symposium - International Astronomical Union*, 200, 33–39
- Winters, J. G., Henry, T. J., Jao, W.-C., et al. 2019, *AJ*, 157, 216
- Willez, J., Abad, J. A., Abuter, R., et al. 2019, *A&A*, 629, A41
- Zanazzi, J. J. & Lai, D. 2017, *Monthly Notices of the Royal Astronomical Society*, 473, 603

*BIBLIOGRAPHY*

- Zhu, Z., Hartmann, L., Nelson, R. P., & Gammie, C. F. 2012, *The Astrophysical Journal*, 746, 110
- Zúñiga-Fernández, S., Bayo, A., Elliott, P., et al. 2021a, *A&A*, 645, A30
- Zúñiga-Fernández, S., Olofsson, J., Bayo, A., et al. 2021b, *A&A*, 655, A15
- Zuckerman, B. & Becklin, E. E. 1993, *ApJ*, 406, L25
- Zuckerman, B., Rhee, J. H., Song, I., & Bessell, M. S. 2011, *The Astrophysical Journal*, 732, 61
- Zuckerman, B., Song, I., & Bessell, M. S. 2004, *The Astrophysical Journal*, 613, L65
- Zurlo, A., Gratton, R., Mesa, D., et al. 2018, *MNRAS*, 480, 236